SPA-LEED examinations of Gd and Tb silicide monolayers on Si(001)

Autorin: Kristina Sprenger

Erstprüfender: Prof. Dr. Joachim Wollschläger

Zweitprüfender: Prof. Dr. Simone Sanna

Contents

1 Introduction

Since the 1970s, Si is the most widespread material in the manufacturing of semiconductors. One of the main reasons for becoming so successful was the possible improvement in performance at the same time as a reduction of geometric dimensions to smaller scales. The production chains of Si have been perfected to such an extent that it is still the cheapest semiconductor material today, even if it is no longer the most suitable substrate.

Hereby, one-dimensional nanostructures on silicon are attracting considerable interest due to their special physical properties that do not occur on higher-dimensional objects. One method to gain quasi-one dimensional nanostructures as nanowires is to use self-organized epitaxial growth on flat surfaces which is especially promising due to its simplicity and large wire densities obtainable [1]. For this, Rare Earth silicides proved to be especially suitable for building metallic nanowire structures [2]. They can be studied to apply as miniaturized electric contacts or *plasmonic waveguides* [3, 4]. Additionally, these structures can be used to compare them to physical models for one-dimensional metals.

This thesis concentrates on the growth of Gd and Tb silicides on Si(001). Besides nanowires, different RE-induced superstructures in the submonolayer regime are examined. Furthermore, the substrate temperature during deposition of deposited RE material was varied. The examination of the surface morphology is performed by *Spot Profile Analysis Low-Energy Electron Diffraction* (SPA-LEED). By SPA-LEED, periodicities on the sample surface in areas of some nanometers can be detected, providing an advantage to the often used method of *Scanning Tunneling Microscope*, which concentrates on smaller areas. Additionally, an *X-ray Photoelectron Spectroscopy* (XPS) measurement was performed to analyze the chemical composition of the surface to ensure a clean preparation. In contrast to conventional LEED measurements, by spot profile analysis the profile shape can be studied allowing to draw conclusions about the surface morphology.

Chapter 2 provides the theoretical basics for the measurements and evaluation performed in the context of this thesis. Afterwards, chapter 3 introduces the used materials and presents their known superstructures on Si(001). In chapter 4, the experimental basics of the measurement methods of this thesis are presented. Additionally, the UHV chamber is described in which the samples were prepared and SPA-LEED measurements were performed. Chapter 5 deals with the measurement results of SPA-LEED and XPS measurements and their evaluation followed by a discussion including a comparison with other research. This thesis is concluded by a summary of the results in chapter 6.

2 Theoretical Background

In the following chapter, the basic theoretical background underlying this thesis will be introduced and explained. First, the basic properties of crystalline solids and surface structures are discussed in Chapter 2.1.1 and 2.1.2. After that, the background of epitaxial growth and its modes are explained in chapter 2.1.3. In chapter 2.2, diffraction on periodic structures is explained, followed by the basic theory of the analysis of intensity profiles of reflexes in 2.3. In chapter 2.4, the principles of X-ray photoelectron spectroscopy are explained.

2.1 Crystal Structures

In the following subchapters, theoretical basics for cristalline volumes and their surfaces will be described. In the end, there will be a short explanation of the different modes of epitaxial growth.

2.1.1 Volume Structures

In solid state physics, one needs to distinguish between the solid and its surface. The model of the solid itself is seen as a periodical pattern of repeating identical unit cells. Based on this assumption, many properties rest upon the periodicity. Primitive unit cells are the smallest repeating unit, which consist of a single-atomic or multi-atomic base (see figure 2.1). Using three basis vectors $\vec{a}_1$, $\vec{b}_1$ and $\vec{c}_1$ of the primitive unit cell, the crystal lattice $\vec{T}$ can be generated by translating the primitive unit cell

$$\vec{T} = u\vec{a}_1 + v\vec{b}_1 + w\vec{c}_1 \text{ with } u, v, w \in \mathbb{Z}. \tag{2.1}$$

The atoms in the unit cell are called base with the atom positions R in the solid defined by

$$\vec{R} = \vec{T} + \vec{r}_i = \text{ with } r_i \text{ as positions of atoms } i \text{ in the unit cell.} \tag{2.2}$$

If the unit cells are distinguished according to the translation symmetries, 7 different crystal lattices with primitive unit cells are obtained. By adding further lattice points in the middle of the unit cell (space-centered) or the outer surfaces (face-centered and base-centered), one can get 14 crystal lattices in total, whereby the unit cells of the additional cubic crystal lattices extend the classification system to 14 BRAVAIS lattices [5].
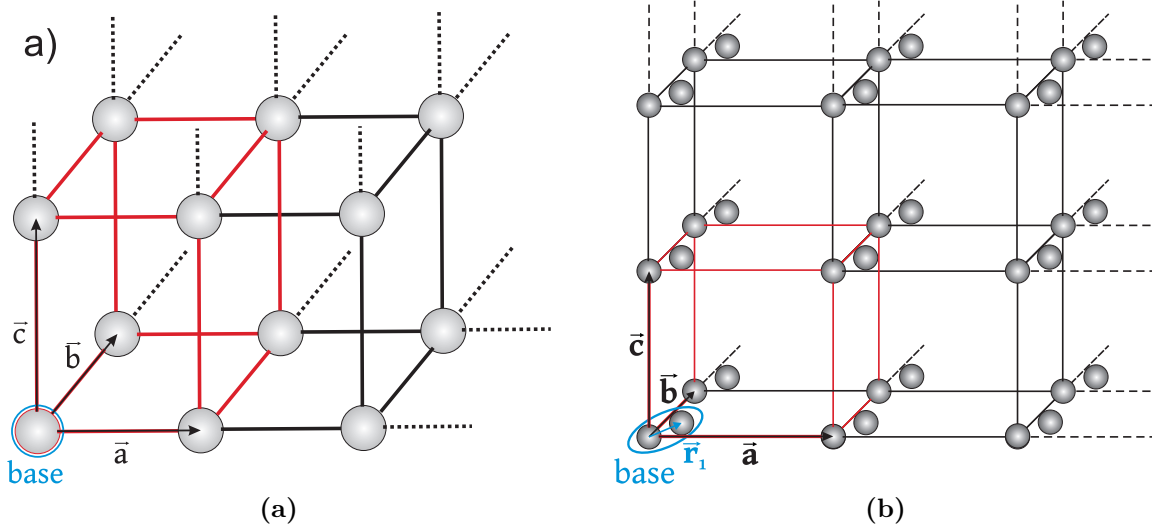
Figure 2.1: Model of a cubic-primitive lattice with a) one and b) two atomic base. $\vec{a}$, $\vec{b}$ and $\vec{c}$ are base vectors which span the unit cell (red).The relative position of the second unit cell atom is given by $\vec{r_1}$.

To define a plane in a grid, MILLER indices are introduced. For defining them, one determines the intersection points of the coordinate axes with the plane and forms the reciprocal value. If the pair of values obtained hereby is not consisting of integers, the indices are multiplied by the smallest common multiple. The notation of negative numbers is with an overscore instead of a minus sign. The components of that tuple, the MILLER indices, are named h,k and l. An index of value 0 describes an intersection in the infinite which means that the referring base vector is parallel to the plane.
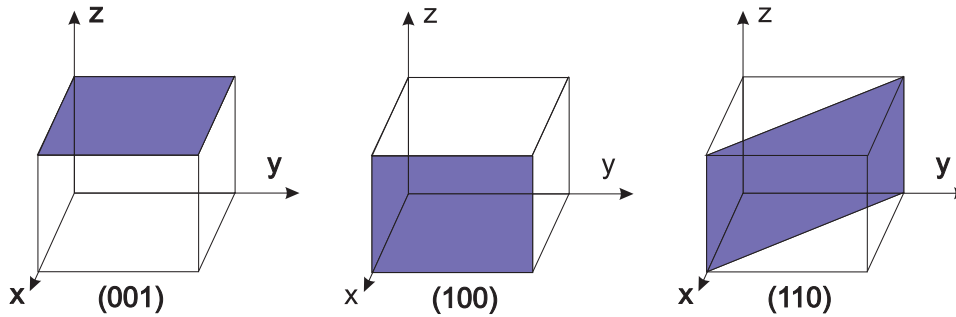
Figure 2.2: Crystal planes and corresponding MILLER indices in the coordinate system with coordinate axes x, y and z. The planes are marked in violet limited to a cuboid which can be referring to a not further defined cubic unit cell.

2.1.2 Surface Structures

In contrary to the structures described in 2.1.1, surface structures are not described under the condition that they are extended infinitely in all spatial directions. In reality, crystals

are limited by two-dimensional terminating surfaces with deviating physical and chemical properties. To describe them, one can use two surface grids, one for the substrate and one for the surface itself. The substrate grid understands the surface as idealized and has the periodicity of the volume. Due to reduced translation symmetry, one can simplify the translation vectors $\vec{T}$ to be written as

$$\vec{T}_{\text{solid}} = r\vec{a}_2 + s\vec{b}_2 \text{ with } r, s \in \mathbb{Z}. \tag{2.3}$$

On the surface, unsaturated bonds can lead to reconstruction of surface atoms. This happens to reduce the total energy of the system. A reconstructed surface differs from an equivalent plane in the solid. Therefore, one can write the translation vector for the surface as

$$\vec{T}_{\text{surface}} = p\vec{a_3} + q\vec{b_3} \text{ with } p, q \in \mathbb{Z}. \tag{2.4}$$

Instead of 14 BRAVAIS grids for classifying crystal structures, surfaces can be described by 5 BRAVAIS lattices (see figure 2.3).
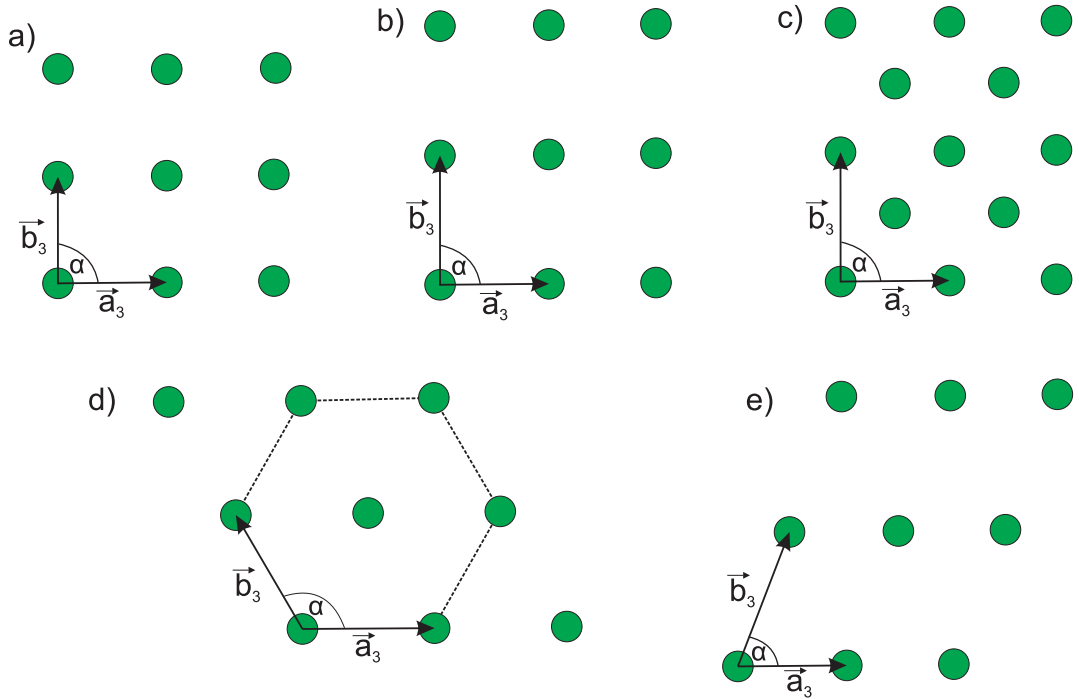
Figure 2.3: Two-dimensional BRAVAIS lattices. a) square $[a = b, \alpha = 90°]$, b) primitive rectangular $[a \neq b, \alpha = 90°]$, c) rectangular centered $[\alpha \neq b, \alpha = 90°]$ with centered base atom, d) hexagonal $[|a| = |b|, \alpha = 120°]$ and e) oblique-angled [else].

The relation between substrate lattice and surface lattice can mostly be described by WOOD notation [6]. For this, the lengths of their base vectors are related by $a' = ma$ and $b' = nb$.

$$\frac{|\vec{a}_3|}{|\vec{a}_2|} = m \qquad\qquad \frac{\left|\vec{b}_3\right|}{\left|\vec{b}_2\right|} = n \tag{2.5}$$

describes the ratio of the lengths of the translation vectors. The super structure can be described as

$$X(hkl)c\,(m \times n) - R\Phi° - Ad. \tag{2.6}$$

hkl are the MILLER indices, whereas X stands for the substrate and Φ for the rotation angle between base translation vectors of substrate and super structure. c includes a possible centering like in Si(001)c(4 × 2). If the super structure is induced by adsorbate atoms, Ad is replaced by the respective chemical symbol with the number of adsorbate atoms existing in one unit cell. (e.g. Si(001)$\sqrt{3} \times \sqrt{3} - R30° - 3Bi$).

If the super structure shows non commensurable behavior, WOOD notation can not be used. Not commensurable super structure means that the equation $\angle(a_2, b_2) = \angle(a_3, b_3)$ can not be fulfilled - the angle between the surface vectors differs from the angle between the substrate vectors. Instead, one has to use matrix notation by Park and Madden [7]. By matrix notation, the relation between translation vectors of substrate and super structure are transferred to a matrix with

$$\vec{a}_3 = G_{11}\vec{a}_2 + G_{12}\vec{b}_2 \qquad \text{and} \qquad \vec{b}_3 = G_{21}\vec{a}_2 + G_{22}\vec{b}_2. \tag{2.7}$$

The matrix G describes the super structure by

$$G = \begin{pmatrix} G_{11} & G_{12} \\ G_{21} & G_{22} \end{pmatrix}. \tag{2.8}$$

2.1.3 Epitaxial Growth

The samples used for this thesis were prepared by using epitaxial growth. Applying more than one monolayer of adsorbates, one speaks of a thin layer. If it happens to grow crystallographically oriented on a crystalline substrate, it is called epitaxy [8]. The growth of the layer depends on thermodynamic and kinetic boundary conditions. Due to thermodynamic consideration of boundary and surface energies of substrate and adsorbate, one can distinguish between different modes of growth:

- **Layer-by-layer growth (Frank-van-der-Merve)**
  Every atomic layer is completed, before a new layer begins to form. This happens when bindings of adsorbates are weaker than the ones to the substrate.

- **Island growth (Volmer-Weber)**
  Islands are formed, if the inter-adsorbate-bindings are stronger than the ones to the substrate.

- **Layer-Then-Island growth (Stranski-Krastanow)**
  After a two-dimensional adsorbate monolayer is formed, three-dimensional islands are taking shape.

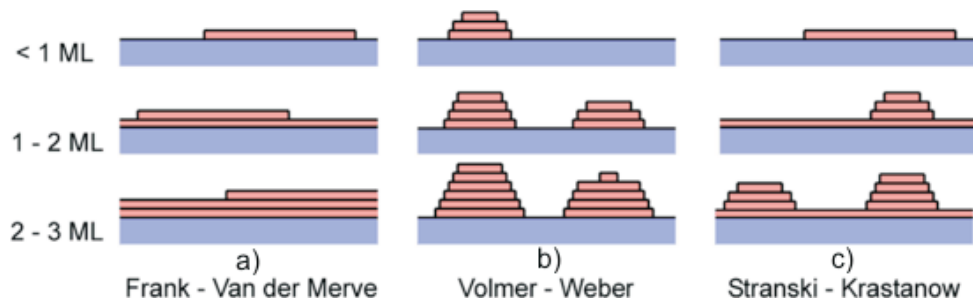These modes are displayed in figure 2.4.

Figure 2.4: Schematic presentation of individual growth modes: a) layer-by-layer/Frank-van-der-Merwe, b) Island/Volmer-Weber, c) Layer-Then-Island/Stranski-Krastanow. Taken and modified from [9].

Lattice mismatch

If adsorbate and substrate are not the same material (heteroepitaxy [10]), the lattice constants of the unit cells usually differ from each other. The degree of strain and dislocations depends upon epitaxial layer lattice mismatch and thickness - if the strain energy is less than required to create dislocation, the layer remains strained, or becomes relaxed with dislocations. Here, the lateral lattice constants are of importance, whereby the lattice mismatch can differ in both directions. The following definition of lattice mismatch used in this thesis is

$$\epsilon = \frac{a_{Ads} - a_{Sub}}{a_{Sub}} \qquad \text{with } a_{Ads} \text{ and } a_{Sub} \text{ as lateral lattice constants} \qquad (2.9)$$

after [11].
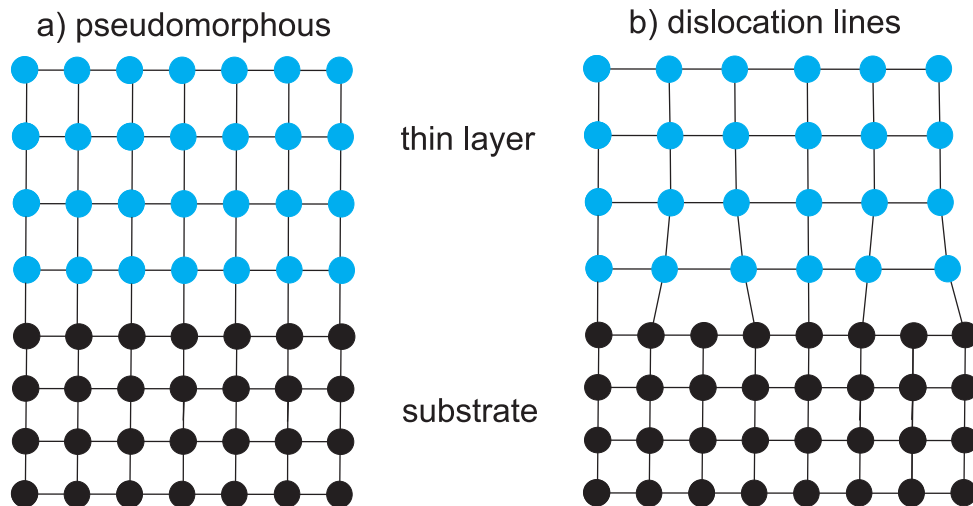
Figure 2.5: Schematic figure of lattice mismatch and possible relaxation state. In a), substrate and adsorbate have the same lateral lattice constant. Whereas in b), dislocation lines are built to minimize tension in the higher planes of the thin layer. Modified from [11].

Due to the lattice mismatch, stresses are built up in the adsorbate layer, which can be counteracted with pseudomorphous growth or the formation of dislocation lines (see fig.

2.5). Pseudomorphic growth is preferred in cases of low layer thickness and low lattice mismatch. From a certain layer thickness onwards, however, energetically more favorable dislocation lines are formed [12].

2.2 Diffraction on periodic structures - LEED

This chapter will deal with basic theory of electron diffraction and the use of reciprocal space.

2.2.1 The development of LEED

The first experiments with electron scattering were carried out by Davisson and Germer in 1927. The method of LEED (Low Energy Electron Diffraction) is a surface-sensitive standard method of surface physics and uses the diffraction of an electron beam with low energy electrons, here of about $50 - 300$eV ($\lambda = 1 - 2$Å). Hereby, the surface structure of crystalline solids can be characterized down to a penetration depth of a few monolayers.

To evaluate LEED images, one looks at the diffraction patterns that are reflected from the sample surface and then detected on a screen. The wavelength used here is the corresponding DE BROGLIE wavelength of the electrons with

$$\lambda = \frac{h}{\sqrt{2mE}}. \tag{2.10}$$

To evaluate the diffraction phenomena the concept of the reciprocal space is used.

2.2.2 Reciprocal Space for surface structures

Reciprocal Space is a model to interpret the diffraction on periodic structures. Its base vectors are represented by plane waves for what it is also called $\vec{k}$-space. The points in two-dimensional reciprocal space are described by the corresponding grid vectors G with the MILLER indices $h, k \in (0, \pm 1, \pm 2..)$ and the direction vectors $\vec{a}^*, \vec{b}^*$ analogous to equation 2.4 as follows:

$$\vec{G}_{hk} = h\vec{a}^* + k\vec{b}^*. \tag{2.11}$$

The relation between reciprocal vectors and the real space lattice for two dimensional structures is given by

$$\vec{a}^* = 2\pi \cdot \frac{\vec{b}_3 \times \vec{n}}{|\vec{a}_3 \times \vec{b}_3|} \qquad \text{and} \qquad \vec{b}^* = 2\pi \cdot \frac{\vec{n} \times \vec{a}_3}{|\vec{a}_3 \times \vec{b}_3|} \tag{2.12}$$

with n as unit vector orthogonal to the surface. Where the crystallographic vectors have the dimension [length], the reciprocal vectors $\vec{a}^*$ and $\vec{b}^*$ have the dimension of [1/length],

this is where the name of reciprocal space comes from. Reciprocal and real crystallographic vectors have the property for surfaces to always lay in the same plane and the two lattices being of the same type of BRAVAIS lattice. The vector $\vec{a}_3$ is perpendicular to $\vec{b}^*$ and $\vec{b}_3$ is perpendicular to $\vec{a}^*$.

Due to the reduced dimensionality of the diffraction grid compared to a three-dimensional grid, the interference condition perpendicular to the surface is eliminated. In the direction of the volume there are further scattering centers, but in the direction of the vacuum these are located at an approximate infinite distance, which is why the reflections come infinitely close together and so-called diffraction rods are created. Figure 2.6 shows the difference between diffraction results of crystalline volumes and surfaces.
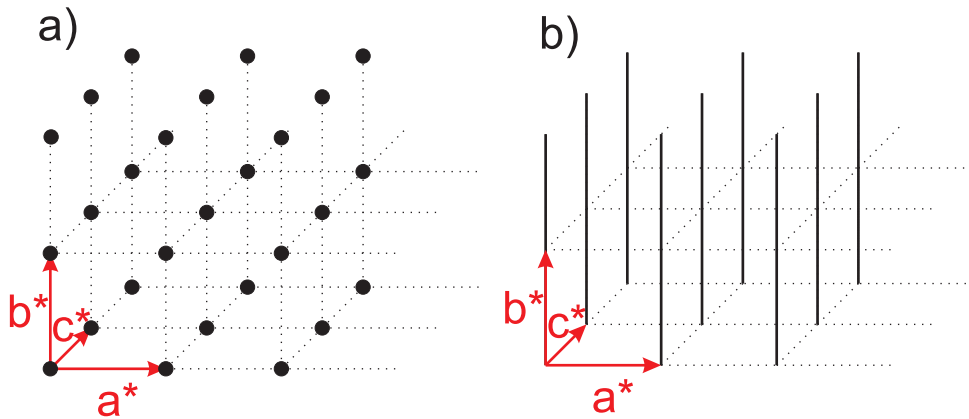

Figure 2.6: Schematic illustration of concept of reciprocal space for 3D crystalline structures in a) and 2D surface in b) with a square unit cell. In a) one can see BRAGG peaks, whereas in b) emerge lattice rods due to translation symmetry. The dotted lines are guides for the eye only. Further explanation see continuous text. Taken from [13].

### 2.2.3 Diffraction on periodic structures

For diffraction on periodic structures, one can set up conditions for constructive and destructive interference. Using wave-particle-dualism of quantum physics, one can assign a particular wave length to the electrons used for diffraction. Due to sufficient distance between electron source and sample surface, one can approximate the electrons as a plane wave. With help of figure 2.7, the conditions for constructive interference can be derived. This is valid for two neighbouring scattering centers whose position relative to each other can be described by vector $\vec{a}$.

Constructive interference is to be expected, when equation 2.13 is fulfilled.

$$\vec{a} \cdot (\vec{s} - \vec{s_0}) = h_1\lambda \qquad\qquad \text{with } h_1 \in \mathbb{Z} \qquad\qquad (2.13)$$

$\vec{s}$ stands for the unit vector with direction of the scattered ray, whereas $\vec{s_0}$ is the unit vector pointing in direction of the incoming ray. This means that the change of path lengths equals a multiple of the wave length λ.

Figure 2.7: This sketch illustrates the values and correlations used for deriving the diffraction conditions of two neighbouring scattering centers with relative position $\vec{a}$. Vectors $\vec{s}$ and $\vec{s_0}$ are unit vectors with direction of the incoming and scattered rays. By the red dotted lines, the change in path can be determined. Taken from [14].
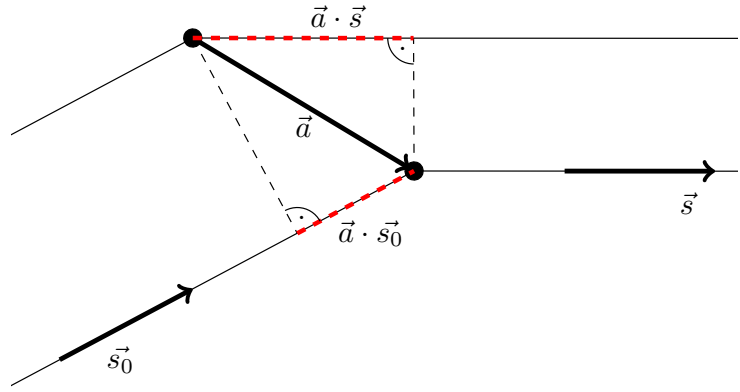
Analogous for two points with the relative position $\vec{b}$ or $\vec{c}$ follows

$$\vec{b} \cdot (\vec{s} - \vec{s_0}) = h_2 \lambda \qquad \text{with } h_2 \in \mathbb{Z} \text{ and} \qquad (2.14)$$

$$\vec{c} \cdot (\vec{s} - \vec{s_0}) = h_3 \lambda \qquad \text{with } h_3 \in \mathbb{Z}. \qquad (2.15)$$

In three dimensions, for any translation vector of reciprocal lattice $\vec{G} = h_1 \vec{a}^* + h_2 \vec{b}^* + h_3 \vec{c}^*$, equations 2.14 and 2.15 can be summarized to

$$\vec{s} - \vec{s_0} = \frac{\lambda}{2\pi} \vec{G} \qquad (2.16)$$

equal to the diffraction condition in 3D crystal structures. This can be proved mathematically by multiplying both sides of the equation 2.16 scalarly with $\vec{a}$, $\vec{b}$ or $\vec{c}$. The relation between real and reciprocal surface vectors for 3 dimensions is defined by

$$\vec{a}^* = 2\pi \frac{\vec{b} \times \vec{c}}{\vec{a} \cdot (\vec{b} \times \vec{c})}, \qquad \vec{b}^* = 2\pi \frac{\vec{c} \times \vec{a}}{\vec{a} \cdot (\vec{b} \times \vec{c})}, \qquad \vec{c}^* = 2\pi \frac{\vec{a} \times \vec{b}}{\vec{a} \cdot (\vec{b} \times \vec{c})}. \quad (2.17)$$

Since reciprocal space of a two-dimensional surface consists of bars, the component of $\vec{G}$ perpendicular to the surface can take on any value to obtain equation 2.16. Thus, only the components of $\vec{s}$ and $\vec{s_0}$, which are parallel to the surface, are important. If one also replaces $\vec{s}$ and $\vec{s_0}$ with the wave vectors $\vec{k}$ and $\vec{k_0}$ according to

$$\vec{s} = \frac{\lambda}{2\pi} \vec{k} \qquad \qquad \vec{s_0} = \frac{\lambda}{2\pi} \vec{k_0}, \qquad (2.18)$$

the result is the sufficient diffraction condition at two-dimensional surfaces with

$$\vec{k_{||}} - \vec{k_{0,||}} = \vec{G_{||}} \qquad \text{with } \vec{G_{||}} = h_1 \vec{a}^* + h_2 \vec{b}^*. \qquad (2.19)$$

Equation 2.19 is called LAUE condition and means, that the momentum perpendicular to the surface $(\vec{k_\perp} - \vec{k_{0,\perp}})$ can be arbitrarily large without having any impact on the Laue conditions. As consequence, constructive interference is observed on every point along the perpendicular direction.

Ewald Construction

To visually represent the relations between wavevector, diffraction angle and reciprocal lattice of the structure, the EWALD construction can be used. For three dimensional structures, it is a sphere which can be, for two dimensions, reduced to a circle and can be pictured as a cut through reciprocal space. So the Ewald sphere results in an Ewald circle which can be seen in figure 2.8.
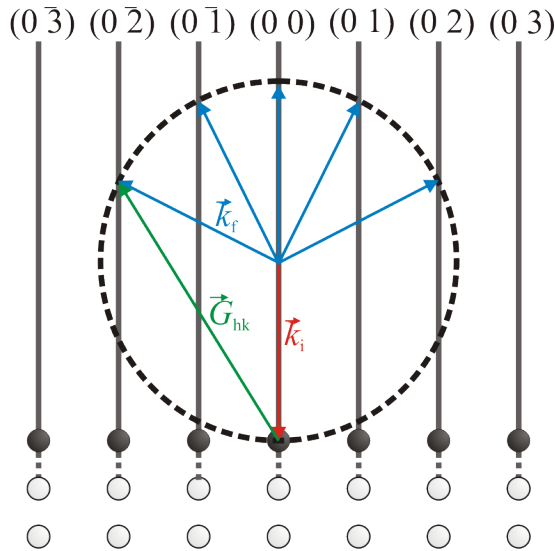

$(0\,\bar{3})\ (0\,\bar{2})\ (0\,\bar{1})\ (0\,0)\ (0\,1)\ (0\,2)\ (0\,3)$

Figure 2.8: Construction of EWALD circle as a cut though reciprocal space for LEED optics. $\vec{k}_i$ is an incident wave vector and the wave vector of the reflected wave is $\vec{k}_f$. The edge of the EWALD sphere results from all possible directions of the wave vector of the scattered reflection, its radius from the amount of the vector $|\vec{k}_i| = |\vec{k}_f|$. Where the wave vector $\vec{k}_f$ intersects diffraction rods with $\vec{k}_{i,||} - \vec{k}_{f,||} = \vec{G}_{hk,||}$ there are diffraction reflexes in LEED. Taken from [15].

This visualization is built by plotting the incident wave vector $\vec{k}$ in such a way that the arrowhead is at the origin of the reciprocal space. Afterwards a sphere with radius $|\vec{k}_i|$ and its origin at the tip of $\vec{k}_i$ is drawn. The points of intersection of the sphere with the diffraction rods indicate where the reflexes are to be expected. In the construction of the EWALD sphere it is assumed that the magnitude of the incident and reflected wave vector are equal. This corresponds to the conservation of energy, thus only the elastically scattered electrons are considered.

Figure 2.7 visualizes the correlations between incoming and scattered vectors for deducing the diffraction conditions.

2.2.4 Kinematic approximation

Due to the strong interaction of the electrons with the crystal, a possible multiple scattering of the electrons at the crystal is not negligible. The complete information about the surface condition is therefore only accessible within the framework of dynamic diffraction theory. But since this theory becomes very complex when describing a defective surface, the following uses the kinematic approximation and multiple scattering can be disregarded in order to investigate the crystallography and morphology.

The kinematic diffraction theory is limited to the description of the reflex profiles and its positions. The direction dependency of diffraction is not taken into account.

Another assumption which is made is the FRAUNHOFER approximation. Due to this,
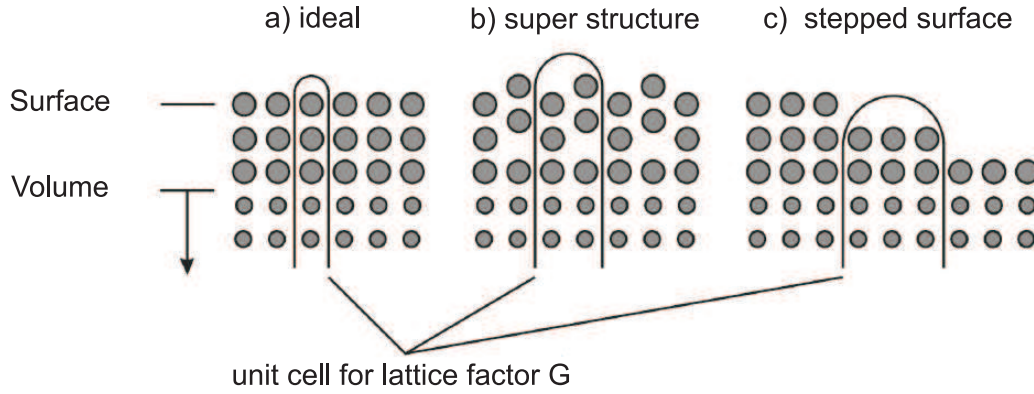
Figure 2.9: These are three different column-shaped unit cells, like they are used in kinematic diffraction theory. a) shows an ideal arrangement of volume and surface atoms, b) gives the picture of a periodic super structure on the surface, whereas c) displays a stepped surface with terraces. Taken and modified from [16].

waves in great distance to their source can be seen as plane waves. The distance between detector and sample has to be much larger than the dimension of the sample surface.

Sources for the following thoughts are [17] and [18]. As seen in figure 2.9, after dividing the surface in columnar unit cells, the wave function of a surface scattered electron can be described by

$$\psi(\vec{K}, \vec{k}_i) = \frac{1}{N} \sum_n \psi_n e^{i\vec{K}\vec{r}(n)}. \tag{2.20}$$

Hereafter, the wave function results as sum over the scattering amplitudes ψ_n of all n unit cells of the surface, located at position $r(n)$, also considering the phase shift $\vec{K}\vec{r}(n)$. N means an appropriate normalization and the scattering vector is $\vec{K} = \vec{k}_i - \vec{k}_f$, with hereby $\vec{k}_i$ being the incident vector and $\vec{k}_f$ the scattering vector. The scattering amplitude of a unit cell $E(n)$ is defined by

$$\psi_n = \sum_{\nu \in E(n)} f_\nu e^{i\vec{K}\vec{r}(\nu)} \tag{2.21}$$

with f_ν as form factor of all atoms at positions $\vec{r}(\nu)$, considering phase shifting. By this, one can look at multiple scattering inside one unit cell, but not between different unit cells. The wave function $\psi(\vec{K}, \vec{k}_i)$ is not an experimentally accessible measurable variable, which is why intensity is now more considered by

$$I(\vec{K}, \vec{k}_i) = |\psi(\vec{K}, \vec{k}_i)|^2 = \frac{1}{N^2} \sum_n \sum_m \psi_n \psi_m^* e^{i\vec{K}[\vec{r}(n) - \vec{r}(m)]}. \tag{2.22}$$

In kinematic diffraction theory, the atomic form factor of all columns is considered equal. If one assumes that the base can be composed of just one atom, equation 2.22 can be simplified to

$$I(\vec{K}, \vec{k}_i) = F(\vec{K}, \vec{k}_i)G(\vec{K}) \tag{2.23}$$

with $F(\vec{K}, \vec{k}_i) = |f(\vec{K})|^2$ as form factor and $G(\vec{K})$ as lattice factor.

The form factor gives the intensity along the lattice rods. Generally, the lattice factor is given by

$$G(\vec{K}) = \sum_n \sum_m e^{i\vec{K}[\vec{r}(n) - \vec{r}(m)]} \tag{2.24}$$

and considers the position and form of diffraction reflexes. Perfect surface lattices are described by $\vec{T} = u\vec{a} + v\vec{b}$. When considered additionally a variation in height, K-dependency is reduced to parallel components of the scattering vector and the lattice factor is simplified to

$$G(\vec{K}_{\parallel}) = \sum_n \delta(\vec{K}_{\parallel} - (m_1\vec{a}^* + m_2\vec{b}^*)) \text{ with } m_1, m_2 \in \mathbb{N}. \tag{2.25}$$

The grid factor in the $\vec{K}_{\parallel}$-plane consists of delta function at the grid points of the reciprocal grid and is independent of the $\vec{K}_{\perp}$-direction. This leads to the diffraction rods. In reality, the assumptions made here are often not correct, resulting in a deviation of the reflex profile. Within the scope of a reflex profile analysis, conclusions can be drawn about the morphology of the surface. Further information can be found in references [12, 19, 20].

2.3 Intensity profiles of reflexes

For examining super structures and how they are arranged, in the context of this thesis, the intensity profiles of reflexes are analyzed. Therefore, one can use the analogy to diffraction of light on periodically arranged scattering vectors as explained in the following. The individual scattering centers are sources for elementary waves. By FRAUNHOFER approximation, light beams reach the screen nearly in parallel. Figure 2.10 shows, that the difference in path length of two neighbouring beams corresponds to $\Delta x = g \cdot \sin\Theta$ with g as distance between two neighbouring scattering centers. By this follows the phase difference $\Delta\varphi$ with

$$\Delta\varphi = 2\pi\frac{\Delta x}{\lambda} = 2\pi\frac{g\sin\Theta}{\lambda}. \tag{2.26}$$

At this point, phasors are introduced as description of the single waves which denote the complex amplitude of waves. Figure 2.11 shows a vector diagram for four phasors, equal to a diffraction on $N = 4$ scattering centers.

Figure 2.10: Diffraction process, schematic presentation. Wave fronts reach a surface with equal atom distance g and the path difference Δx of the diffracted rays. This shows exemplary $N = 4$ diffraction centers causing elementary waves. Taken from [14].
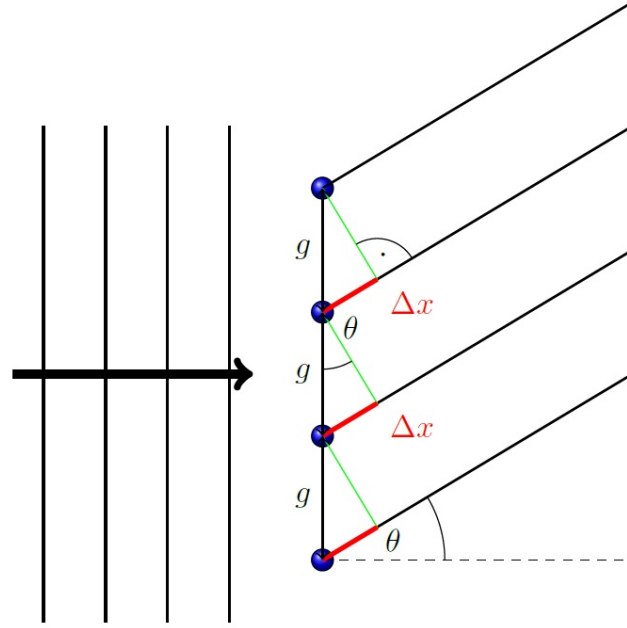
For N scattering centers, the triangle $P_1 P_2 Q$ in figure 2.11 gives

$$\sin(\frac{\Delta\varphi}{2}) = \frac{A_1}{2 \cdot r}, \tag{2.27}$$

whereas the triangle $P_1 S Q$ results in

$$\sin(N \cdot \frac{\Delta\varphi}{2}) = \frac{A_{Ges}}{2 \cdot r}. \tag{2.28}$$

One can eliminate r by reshaping and inserting, which means that

$$I_{Ges} = I_0 \cdot \left(\frac{\sin(N \cdot \frac{\Delta\varphi}{2})}{\sin(\frac{\Delta\varphi}{2})} \right)^2. \tag{2.29}$$

Hereby, the proportionality of the intensity to the square of the amplitude is taken into account. Figure 2.12 shows intensity profiles for three different values of N.

For the main maxima, phase difference is a multiple of 2π which allows to use small angle approximation. It can be simplified to

$$I_{Ges} = I_0 \cdot \left(\frac{N \cdot \frac{\Delta\varphi}{2}}{\frac{\Delta\varphi}{2}} \right)^2 = I_0 \cdot N^2, \tag{2.30}$$

which means that the intensity of the main maxima is proportional to the square of the numer of scattering centers N. Single scattering centers correspond in experiment to unit cells of surface structures. Transferred to the diffraction of electrons at surface structures, it is thus to be expected that the intensity of the reflexes depends on the domain size. In the experiment, however, thermal effects and the limited resolution of the apparatus also
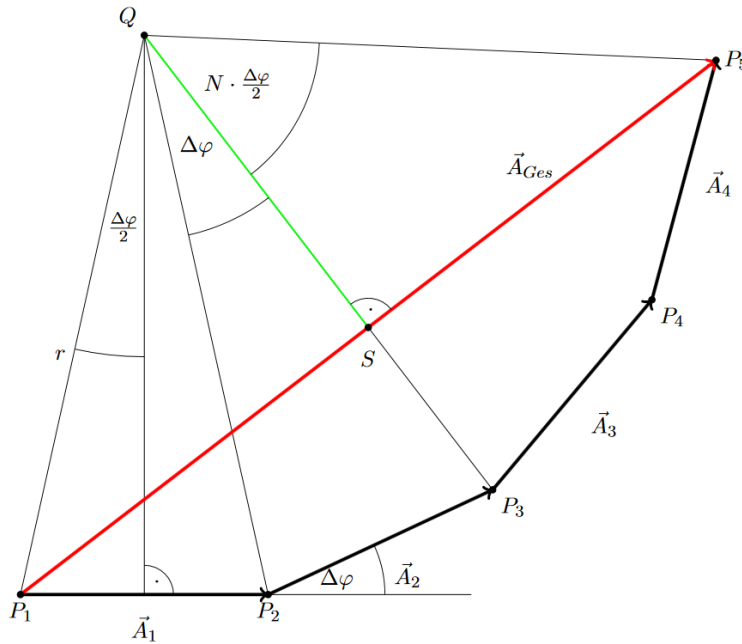
Figure 2.11: Vector diagram for diffraction on 4 scattering centers. The angle $\Delta\varphi$ stands for the rotation between the phasors $\vec{A}_n$. A circle can be drawn with center Q passing every P_n. $\vec{A}_{Ges}$ is the vector sum of all phasors, its absolute value being equal to the amplitude on the screen. Taken from [14].

influence the measured intensities. Nevertheless, the larger the domains, the more intense the reflexes should be. The further analysis of equation 2.29 also shows a dependence of the reflex widths on the number of scattering centers N. The numerator of the fraction of equation 2.29 has further roots between 0 and 2π which leads to an erasure of total intensity at the positions $\Delta\varphi = \frac{2\pi \cdot k}{N}$ mit $k \in \{1, ..., N-1\}$. This means that at regular intervals there are exactly $N-1$ intensity minima between the main reflexes. The greater N is, the narrower the main reflexes must become, as the neighboring minima move closer and closer together. For the diffraction of electrons at surface structures this means that the peak width at half-height of reflexes must decrease with increasing domain size. This chapter is based on [14].

Surface Roughness

The roughness of the surface has influence on the diffraction pattern too. The diffraction rods described above appear for a perfect flat surface and produce sharp spots in the LEED picture. They are only broadened by instrumental influence, not due to physical properties of the surface. The apparatus sets the minimum experimental width of the spots. When deviation from that perfect surface in form of surface point defects takes place, some intensity redistributes to diffuse intensity in the BRILLOUIN-zone.

Real surfaces are never perfectly flat due to steps. To understand the influences of steps on the diffraction pattern, one can use a model of a two-level surface. Thereby, it is expected that all atoms are at lattice sites. The two-dimensional islands grow as a second layer on the surface and are separated by single atomic steps. The diffraction pattern is hereby dependent on the interference between the different layers. The LEED spots now consist of a sharp central peak based on the long-range order on the surface and a diffuse part. The central peak is given by constructive interference of both the upper and the lower layer. Hence, for an „in-phase" there is only one sharp central peak, whereas for
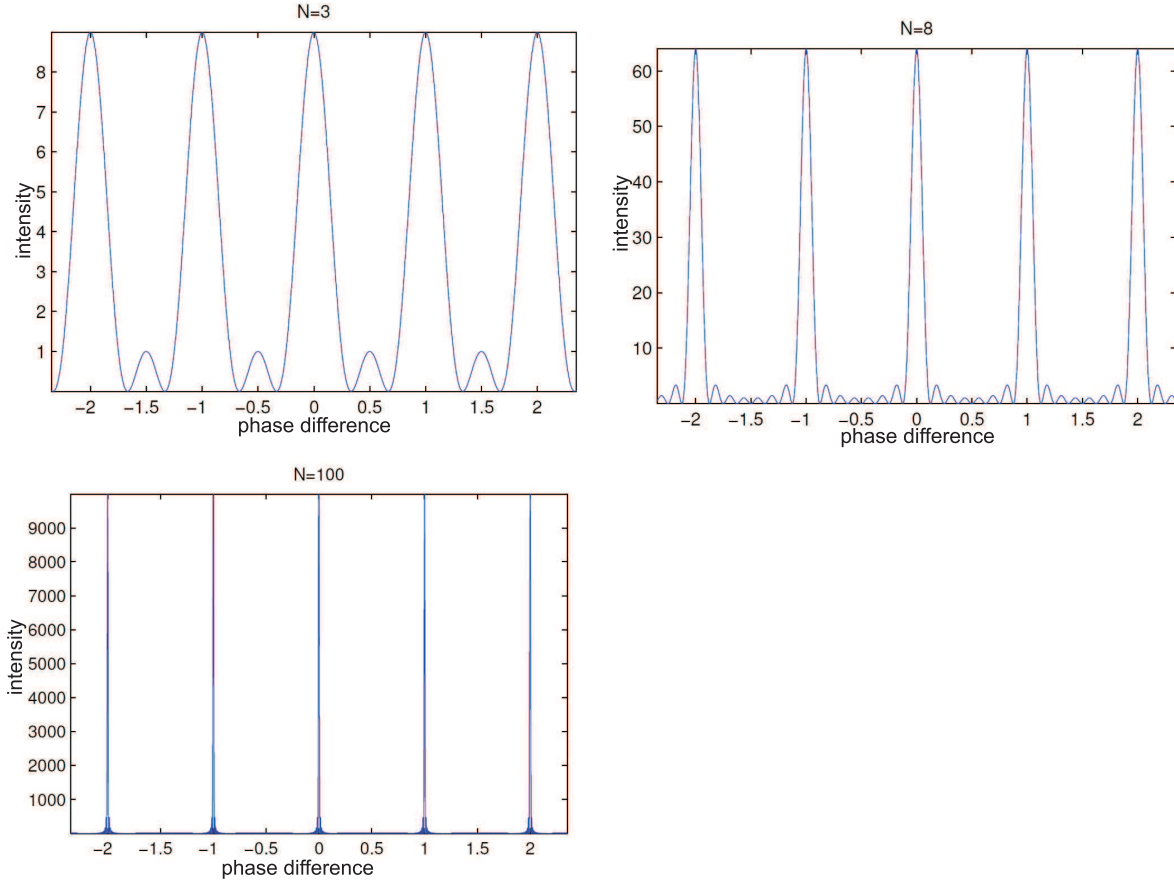
Figure 2.12: Intensity profiles for different numbers of scattering centers N. Exemplary, intensity courses for $N = 3, 8$ and 100 are presented for constant incoming intensity I_0. On the abscissa, phase difference divided by 2π is applied. Dependance for intensity und FWHM of main maxima on numer of scattering centers N is shown. Modified from [14].

an „out-phase" destructive interference leads to the existence of only a broad diffuse part being visible in the diffraction pattern.

Its intensity depends on the coverage constitution in the first layer and oscillates with a cosine function of the scattering phase and scattering vector $k_\perp$.

The scattering phase S can replace the vertical scattering vector $K_\perp$ as dimensionless value, independent on the material system, with

$$S = K_\perp \frac{d}{2\pi} \tag{2.31}$$

whereas d denotes the height difference of the two surface layers. S describes the phase difference in numbers of electron wavelength when electrons are scattered from adjacent terraces.

For an „in-phase" condition, results are the same as for a perfect surface and all intensity is focused on the central peak. „In-phase" means that the scattering phase is equal to a multiple of an integer value n. This indicates that the scattered electrons are insensitive

to the surface roughness. For all other scattering conditions, there is at least a fraction of destructive interference taking place and the intensity is not (wholly) distributed to the central peak. The contrary situation is called „out-phase" and describes that the scattering phase has a value of $n + 0.5$ and multiples. The interference of the base level and the islands is here completely destructive and the central peak fully vanishes. In this thesis, only an electron energy of 130eV is used. For Si(001), this energy equals an „out-phase" with $n = 2.52$. With no other disturbances, this would mean that no central peak is visible in the measurement results, only the broadening reflex. Due to instrumental influences and the sample having an imperfectly stepped surface with defects and domain boundaries, this is not the case with all measurements performed within this thesis. The principal behavior of the spot profile as a function of vertical scattering vector $K_\perp$ is displayed in figure 2.13.
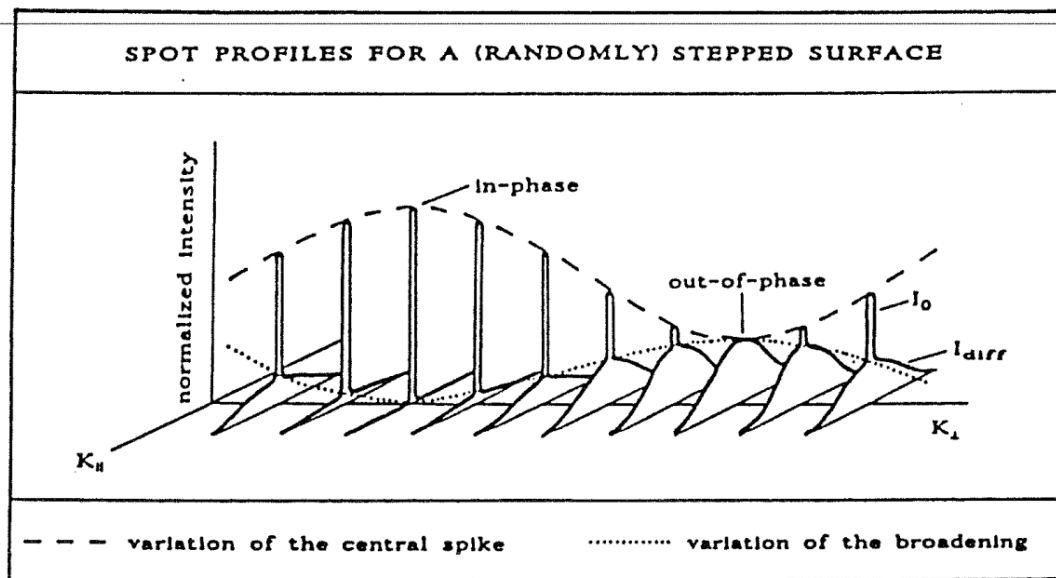

Figure 2.13: General dependence of the spot profile from the scattering vector $K_\perp$ for a randomly stepped surface. The spot profile consists of two parts: the sharp central peak and a broadening. At an „in-phase", only the central peak can be seen, whereas at an „out-phase", only the broadening peak contributes to the intensity profile. Taken from [17].

For anti-phase domains of superstructures, the fundamental reflexes are not broadened. Fundamental reflexes are those present even when no superstructure exists, that means the reflexes which exist only due to periodicity of the base lattice.

The influence of the superstructure on the reflex profile can be derived theoretically. For a two-level system like described here, the profile of the broadening reflex is independent of the vertical scattering vector or scattering phase. Its shape is determined by a geometric terrace width distribution with an average terrace width $\overline{\Gamma}$ of non-interacting steps [22].

If this surface is disrupted by a lateral shift of domains that equals a multiple of the substrate lattice constant, it is shown that the FWHM of a reflex (here e.g. the 0%BZ

broadening reflex) is indirectly proportional to the respective domain sizes in this direction [17].

The average terrace width $\overline{\Gamma}$ can be derived from the FWHM of the broadening reflex with

$$\overline{\Gamma} = a \cdot \frac{1}{\text{FWHM}}. \tag{2.32}$$

The proportional constant a is hereby dependent on the considered reflex.

2.4 X-ray photoelectron spectroscopy (XPS)

X-ray photo electron spectroscopy is based on the photoelectric effect and the fact that the binding energy E_b is specific for each orbital and each element as the binding energy of the electrons is dependent on the COULOMB interaction with the atomic nucleus and the shielding of other electrons [8]. Hence, XPS can be used to directly identify elements and their electronic structure both in samples and on sample surfaces.

In XPS measurements, a sample is illuminated with X-rays, which leads to the emission of so-called photoelectrons.

The kinetic energy

$$E_{kin} = h\nu - E_b - \Phi_A \tag{2.33}$$

of the photoelectrons can be measured and thus provides information about the binding energy E_b if the excitation energy of the used X-rays $h\nu$ and the material dependent work function Φ_A of the analyzer are known. Φ_A can be empirically determined by calibration to a well-known peak in the spectrum. Furthermore, by comparing the relative intensities of peaks of different elements, quantitative information can be obtained such as the stoichiometry of the investigated material.

Figure 2.14 (a) displays a schematic experimental setup for an XPS measurement. The X-rays are directed onto the sample and lead to the emission of photoelectrons. These electrons are then projected through an electron lens system where they are focused into the hemispherical analyzer and reach the detector which counts the electrons according to their kinetic energy. An energy scheme of the occurring energy levels is displayed in figure 2.14 (b), where Φ_S denotes the work function of the sample, E_{kin} the kinetic energy of the photoelectrons and E_F the FERMI energy of sample and analyzer.
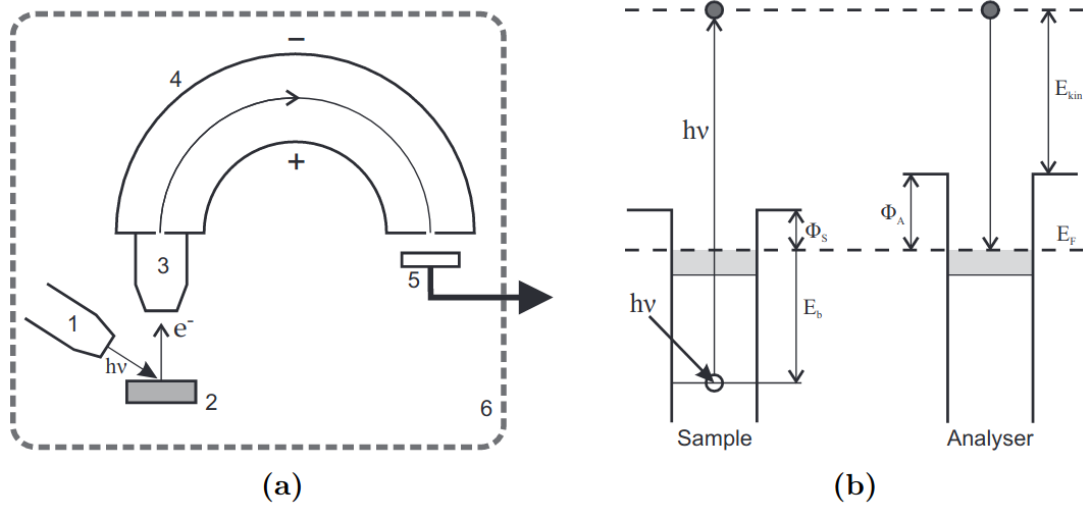
Figure 2.14: Principle of XPS. a) Schematic instrumental construction of a XPS apparatus with 1) X-ray source, 2) sample, 3) electron lens, 4)hemispherical analyzer, 5) detector and 6) vacuum enclosure. b) shows an energy diagram of the process underlying the XPS process. Taken from [23].

3 Material Systems

In the following, the materials used in the frame of this thesis are described. The samples produced for this work are applied on substrate consisting of silicon (001), explained in chapter 3.1. The adsorbate materials used are gadolinium or terbium, which are presented in chapters 3.2 and 3.3. A description of the properties of trivalent earths is given in chapter 3.4.

3.1 Silicon - Si(001)

Silicon is the chemical element with the atomic number 14 and is located in the fourth main group and the third period of the periodic system of the elements. In the earth cover, it is after oxygen the most common element concerning mass fraction. Si is an elementary semiconductor with cubic face-centered unit cells consisting of 8 atoms in diamond structure. Their base consists of two identical atoms at positions $(0,0,0)$ and $(\frac{1}{4}, \frac{1}{4}, \frac{1}{4})$ (see figure 3.1) which can only be distinguished by the orientation of their bindings. The crystal structure forms therefore from two fcc-lattices, which are shifted against each other by $\frac{1}{4}$ of the space diagonal, each consisting of four atoms.
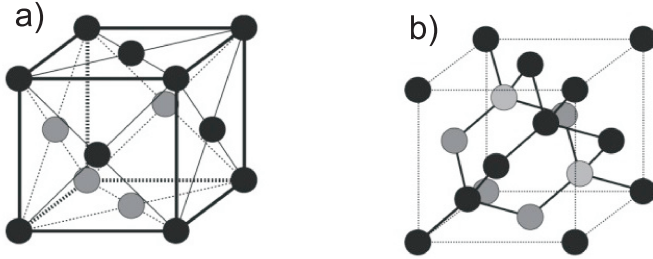

Figure 3.1: Lattice structure of silicon - schematic illustration. a) shows the fcc-lattice of silicon, b) the crystal structure of silicon, equivalent to a diamond lattice. Taken from [24].

Silicon has a lattice constant of $g \approx 5,43$Å [25] and a melting temperature of 1420°C [26]. As a semiconductor, silicon is a hot conductor, so the electrical resistance decreases with rising temperature. (Semi-)conduction is essential for SPA-LEED to avoid charging effects by electrons on the surface. In crystalline silicon, one $2s$-orbital and three $2p$-orbitals merge into four sp^3 hybrid orbitals. They are arranged in a tetrahedral orientation and each of the orbitals hosts a valence electron. The MILLER indices (001) mean that for this thesis, Si is used in an orientation where it was cut along the side of the cubic unit cell. That leads to a unit cell, which is quadratic (see figure 3.1). Due to the fcc arrangement of the cubic unit cell, the side length of the quadratic unit cell is $\frac{\sqrt{2}}{2} \cdot 5.43$ Å$= 3.84$ Å [14].

Figure 3.2 shows how atoms of the first surface level rearrange for energetic reasons. Two neighboring Si-atoms bind to a Si dimer, leading to a (2x1) reconstruction. This reduces the unsaturated bindings on the surface by half. This relocation can impact up to five and
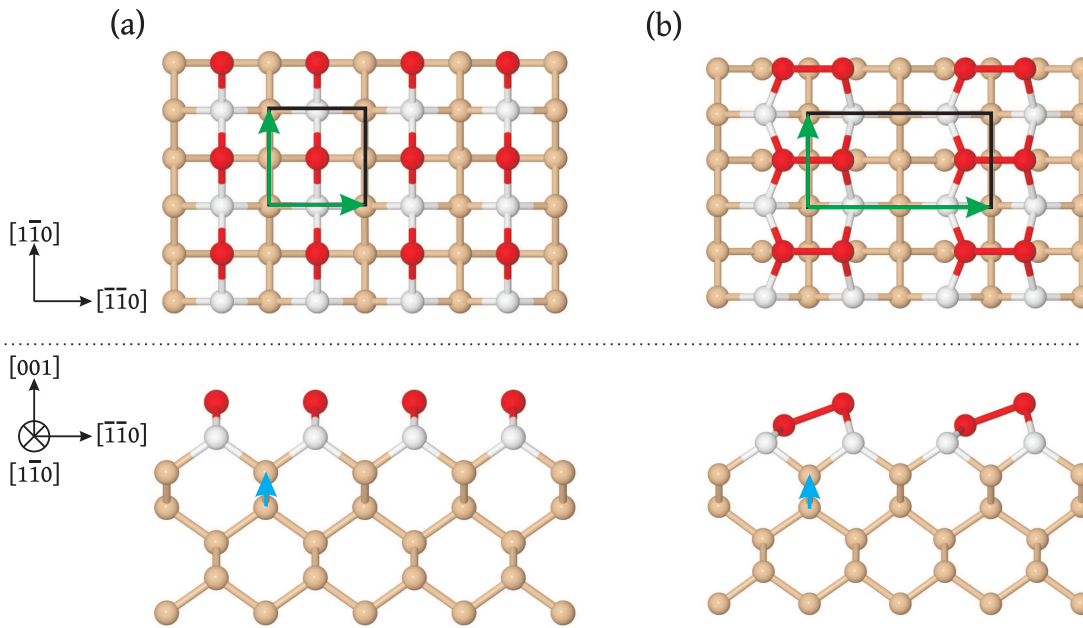
Figure 3.2: Reconstruction of Si (001). a) shows a surface which is not (yet) reconstructed with a (1x1) unit cell, whereas in b) the surface reconstructed into a (2x1) unit cell. The quadratic unit cell from a) changed into a rectangular arrangement (black box). Green arrows stand for the crystallographic vectors, blue ones for layer-spacing. The topmost atom layer is shown in red, second layer in white and lower layers in brown. Taken from [13].

more levels below the surface [27]. Dimer bindings have two different possible orientations, only one of them is shown in figure 3.2. The dimers flip their orientation in high rates for which they can not be distinguished at room temperature.

3.2 Gadolinium

Gadolinium is a chemical element with the atomic number 64, is located in the group of lathanoides and is thereby part of metals of rare earths. The appearance is silver-white and it's malleable. For temperatures lower than 1260°C, gadolinium crystallizes in a hexagonal-thickest crystal structure with lattice parameters a = 363 pm and c = 578 pm [28]. The electron configuration of gadolinium is $[Xe]4f^{14}5d^{10}6s^1$ and it occurs in nature as 7 isotopes [29].

With a CURIE-temperature of 19, 3°C, Gd has the highest CURIE temperature of all lathanoides except iron, cobalt and nickel [30]. Above this limit, it shows paramagnetic behavior.

3.3 Terbium

Terbium (Tb) is also part of the group of lathanoides, has the atomic number 65 and normally consists of a shell with 65 electrons. In 1864, its existence was initially proven spectroscopically by Delafontaine [31]. The electron configuration of terbium is $[Xe]4f^9 5d^{10} 6s^1$ and it is counted in the group of Ytter earths, and on higher level, to the group of rare earths. Terbium can not be found naturally as a free element, but is contained in many minerals. It is used in different fields as solid state devices, fuel cells and sensors, but most common in green phosphors. Additionally, it has ferromagnetic ordering at temperatures below 219K, above it turns into a helical anti-ferromagnetic state and transforms into a disordered para-magnetic state at 230K [32].

3.4 Trivalent Rare Earths on silicon

Trivalent Rare Earths (RE) as gadolinium and terbium show a comparable behavior when applied to silicon (001) due to a strong chemical similarity. They differ only in the amount of 4f electrons that are not directly taking part in the chemical bindings of RE and silicon. Under certain conditions, some RE are shown to build nanowire structures when applied to a Si(001) surface [1, 33, 34]. Further STS spectra research has shown, that a finite density of states at Fermi level points to all RE silicide nanowires having metallic properties [33]. Appelfeller states that silicides with high Si content form directly when pure RE are deposited on the Si(001) surface, and no initial formation of silicides with low Si content is observed [2]. It is claimed that the reaction of RE metals with Si(001) surfaces occurs in a small temperature range [35]. That leads to assume that the needed temperature for formation of RE silicides on Si(001) is in a range where diffusion of Si as the main diffusing species is very high [36].

Nanowires of RE on Si were detected over 20 years ago by NOGAMI and LIU [33, 37]. The nanowires examined by PREINESBERGER shortly afterwards for Dy had lengths of up to 2000Å and widths of about 30Å [1]. When RE material is brought onto clean Si(001) surface, the growth of (2x4)-structures can be detected (in the coverage range of 0.17 to 1.6 monolayers for Dy). A fully (2x4) reconstructed surface could not be observed by LIU and NOGAMI [37]. It always coexisted with clean Si areas which did not disappear even with higher coverages up to 3 monolayers. For low Dy coverages, it was shown that on the Si(001) surface, the Si dimers vanish and the (2x4) superstructure formed by Dy atoms appears. Hereby, 3 Dy atoms were counted per unit cell [37].

With higher coverages of RE, a (2x7) structure appears on the surface, consisting of (2x3) and (2x4) sub-unit-cells. (2x4) and (2x7) reconstructions often coexist on the surface and show similar structure, whereas no pure (2x3) surface reconstruction was detected yet. LIU and NOGAMI report an appearance of a (2x4) superstructure up to 0.2 monolayers of Dy [38]. The (2x7) superstructure subsequently appears afterwards at the cost of decreasing the (2x4) coverage up to 0.33 monolayers, at which the surface is almost entirely (2x7) reconstructed. Figure 3.3 shows a schematic presentation of the two possible alignments of (2x3) and (2x4) structures to build a (2x7)-superstructure which are statistically distributed over the sample surface [34]. This leads to a reduced sharpness of the (x2)

periodicity in the diffraction pattern and the appearance of streaks. (2x7) reconstruction shows a periodicity containing 6 atoms in total (about 0.429 monolayers) which function as a wetting layer for nanowire growth [38, 39]. For lower temperatures of about 500°C, (2x7) reconstruction cannot be prepared exclusively, for about 600°C it is possible with a coverage of about 0.42 monolayers of Dy [13].
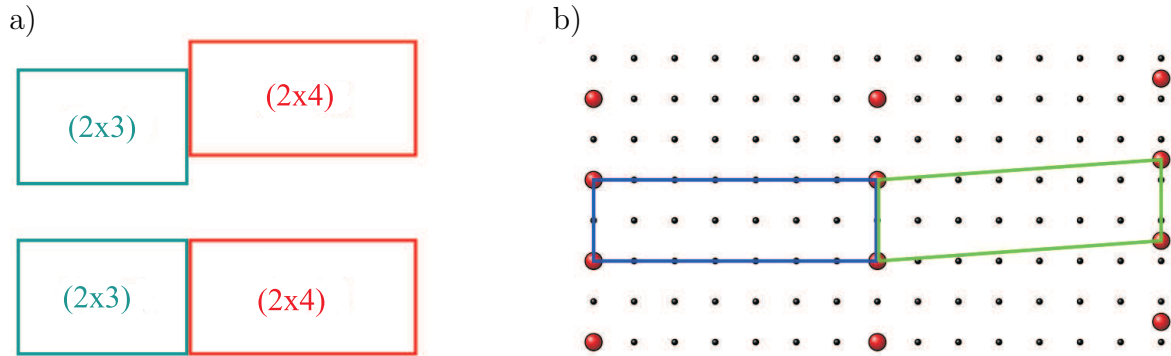

Figure 3.3: Schematic illustration of a (2x7)-reconstruction of RE on Si(001). a) gives the two spatial arrangement possibilities of the (2x3) and (2x4) unit cells forming a (2x7) structure. b) The periodicity of the not reconstructed substrate surface is marked in black, whereas the possible relative positions of the unit cells are shown in blue (not shifted) and green (shifted). Taken from [14].

With further increasing coverage (0.63 - 1.05 monolayers for Dy, [13]), the growth of nanowires can be examined [40]. Nanowire structures appear from 0.5 monolayer to several multilayers and are characterized as structural motifs with a very high aspect ratio.

When LIU and NOGAMI first examined nanowires on Si(001), they assumed lattice mismatches of different magnitude being the cause for their formation in one direction. The structure consequently was assumed to grow alongside the small lattice misfit. This was continued by PREINESBERGER et al for later research. Due to differing experimental results, e.g. variation in maxima positions, the concept of RE vacancies was taken into account [41], even though no evidence for Si vacancies in the nanowires was reported so far. These considerations led to the assumption of different lattice parameters than before and thereby the lattice constant previously strongly differing now moves closer to the lattice constant of Si(001). This led to doubts about this growth model.

Later, HOLTGREWE et al. did theoretical research about the energetic states of nanowires on silicon surfaces [42]. Hereby, erbium silicide nanowires are theoretically examined based on density functional theory, considering different possible nanowire structures. Nanowires are thereby applied to a surface and investigated for increasing width. Results show that the broader the nanowire gets, the lower the energy level of the structure is. A mismatch as assumed before would have strong impact on the energy. It is not yet conclusively clear why the nanowires grow in the way they do. A guess is that it is caused by dynamic effects, perhaps the growth of RE-silicide islands needs more

energy in one spatial direction than in the other, leading to the formation of wires. In 2020, APPELFELLER et al. publicized a joint experimental and theoretical study about a continuous crossover from two-dimensional to one-dimensional electron properties for metallic silicide nanowires based on the growth of $TbSi_2$ on a Si(111) substrate [43]. The results indicate a continuous 2D to 1D transition of the electronic structure for decreasing nanowire width on a vicinal Si(111) surface.

Nanowires can appear individually or in bundles [34]. With even higher coverage (more than 1.05 monolayers for Dy), nanowire bundles start to form on the surface, leading to a whole surface being covered by them (at about 2.1 monolayers) for Dy and temperatures of about 500°C. These bundles form strictly separated [39] in between a mixture of a (2x7) reconstructed surface, sub-structures described earlier in this chapter and Si dimer rows [44–46]. This wetting layer shows non-metallic properties leading to the nanowires not being electrically connected [3]. The surface of nanowires is assumed to arrange in a (2x1) reconstruction, resulting probably from nanowires growing in two domains on the planar surface [2, 34]. Due to their large height and compact appearance, one can assume that they are not just a surface reconstruction, but built of silicides with high Si content [35, 47]. The periodic appearance of nanowire bundles on a surface with high coverage leads to further reflexes in the diffraction pattern, depending on their average groove-to-groove distance. A schematic sketch of groove-to-groove distances of nanowire bundles on the surface is shown in figure 3.4.
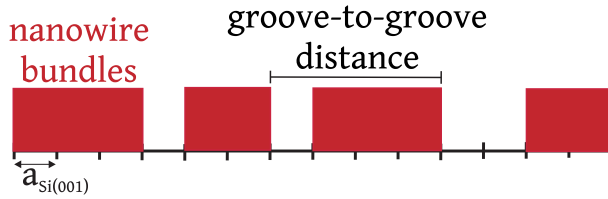

Figure 3.4: Schematic sketch of groove-to-groove distances of nanowire bundles. Nanowire bundles are displayed in red with width of multiples of $a_{Si(001)}$. One exemplary groove-to-groove distance is marked.

Inside monolayer bundles, adjacent nanowires of different width were separated by a distance of one Si(001) unit. For RE coverages exceeding 2.1 monolayers, 3D island growth is observed for Dy [13]. There have been different explanations for the atomic structure of the mentioned wetting layer [39, 40]. The composition of anisotropic islands can be explained by assuming hexagonal instead of a tetragonal $TbSi_2$ atomic structure - a similar bonding configuration of the Si atoms eventually lead to epitaxial growth of these structures. For details on epitaxial growth see chapter 2.1.3.

4 Experimental Basics

In this chapter, all important experimental basics used during this thesis are presented. All samples were fabricated in the same Ultra High Vacuum Chamber in which they were examined based on Spot Profile Analysis - Low Energy Electron Diffraction (SPA-LEED). In chapter 4.1, the creation and operation of the ultra high vacuum in the chamber is explained. It is followed by the experimental basics concerning the fabrication of layers of gadolinium and terbium by evaporation in chapter 4.2. Afterwards in chapter 4.3, the structure of the SPA-LEED apparatus is explained. The theoretical basics are already explained in chapter 2, whereas here the practical use is presented. The preparation of samples and all measurements were performed at Osnabrueck University.

4.1 Ultra High Vacuum (UHV) chamber

The arrangement of the components of the UHV-chamber are displayed in figure 4.1.

The experimental setup consists of two chambers, which are separated by a valve. The substrates are implanted in the prechamber. The prechamber is used for not ventilating the whole UHV chamber when a new substrate is needed. To achieve a pressure in the scale of 10^{-10} mbar, a system of three different pumps is used. The prechamber, as well as the main UHV chamber, are connected to a vane rotary pump and a turbomolecular pump. The first is to ensure a basic pressure of the size of down to 10^{-3} mbar, the molecular pump serves to cover the pressure area down to 10^{-8} mbar. For sample preparation, a base pressure of $(2 \pm 5) \cdot 10^{-10}$ mbar was reached by an ion getter pump. Low pressure is necessary for not having contamination during the process of deposition of rare earth material. With higher pressure, too many impurity atoms could adsorb at the substrate surface and contaminate the whole deposited layer. Further information about the pumps can be found in [8].

Behind the valve between prechamber and main chamber, a sample garage was installed to keep different substrates and samples in UHV. The substrates can be moved from the prechamber to the main chamber by a transfer rod which moves along one axis. In the main chamber, the sample is installed at a manipulator that is rotatable along one axis at 360°, to place the sample in front of evaporator, SPA-LEED or pyrometer. The pyrometer can be directed through one of the windows on the sample surface. By this, the approximate temperature of the sample can be determined. Furthermore, the sample can be heated by pins which are connected to a power supply unit. By that, a direct current is applied and flows through pins and the sample, heating up these components. Also, the manipulator with the sample can be tilted to four directions and moved up and down.
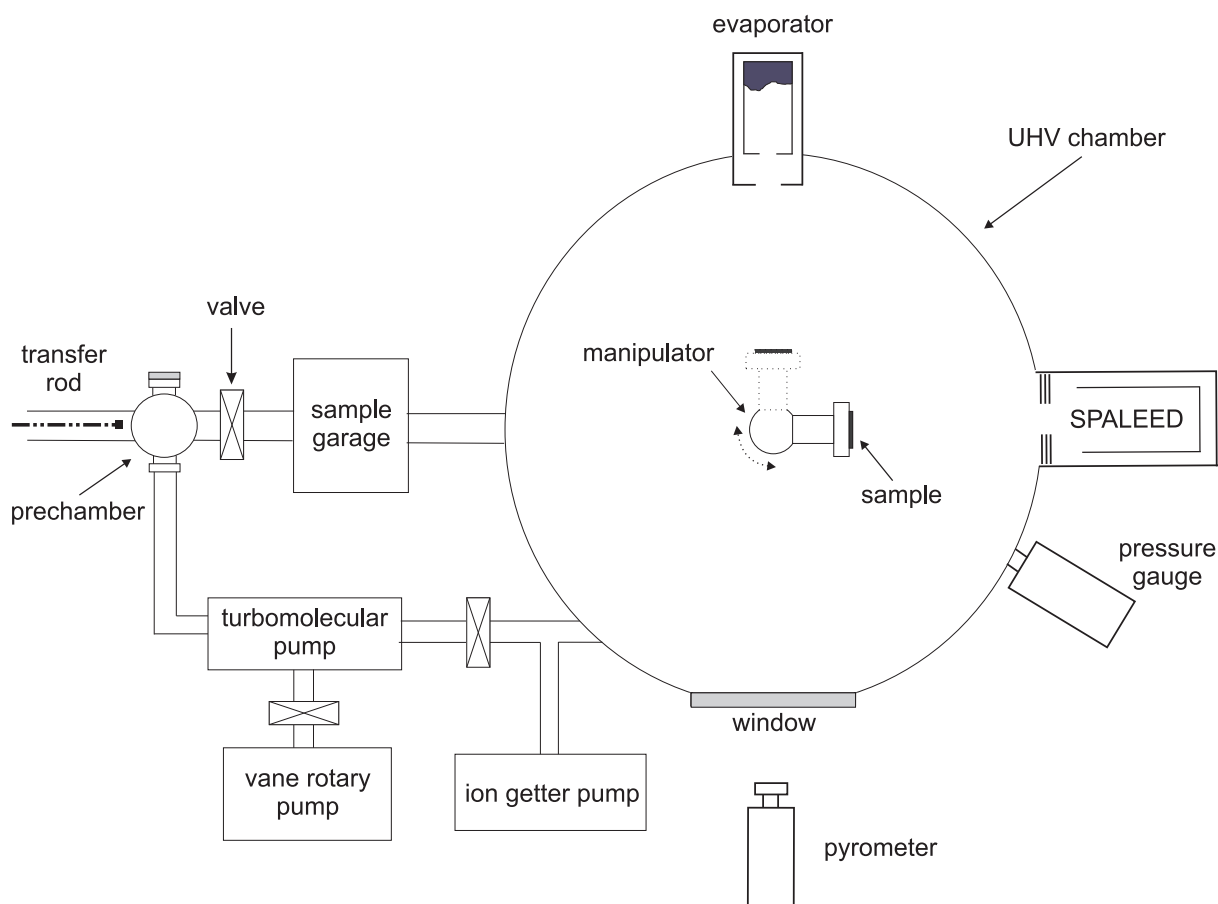
Figure 4.1: Experimental setup of the used ultra high vacuum chamber. The prechamper is used to implant the sample in the chamber system. Via the transfer rod, it can be moved through a valve to a sample garage or the main UHV chamber and is positioned at the manipulator. The manipulator can move the sample in every direction by tilting and turned up to 360°C. The sample can be heated through the manipulator and moved in front of the evaporator for material deposition, of the SPA-LEED for surface analysis and in front of the pyrometer for temperature settings. The ultra high vacuum is reached by a pump system of three pumps.

The evaporator contains a crucible with the rare earth material. For further information about the structure of the evaporator, see chapter 4.2.

4.2 Sample preparation and evaporation

At the sample, a voltage is applied which can be used to heat the Si(001) sample to about 1200°C. For cleaning the substrate surface for deposition, it is heated up to about 1150°C for a few seconds, called flashing. The pyrometer determines the temperature at the sample surface at an estimated accuracy of about ±20°C. The flashing is repeated several times to ensure a better cleaning effect. In between heating sequences, the voltage at the sample is lowered for cooling down the sample. While flashing the first time, the silicon

oxide layer on the surface is blown off and takes interfering atoms with it. Afterwards, the sample is placed in front of the evaporator.

The vaporization material, in this case the rare earths gadolinium or terbium, is filled into a crucible located in the middle of the evaporator case. Besides the crucible and about the level of the rare earth, a spiral filament is located which can be heated by a power source, here named filament control. The spiral filament consists of a tungsten-rhenium wire with a diameter of 0.125mm. When heated, it emits electrons which are accelerated on to the crucible by an applied voltage between itself and the filament of about 1000V. Therefore, the crucible with the vaporization material heats too and rare earth atoms evaporate. They move towards the shutter. When the shutter is opened during a deposition process, rare earth atoms reach the sample surface and the quartz located at the opening of the evaporator. The quartz is part of a quartz crystal microbalance (QCM) which determines the thickness of deposited rare earth material. It is dependent on the deposition time and rate used in the experiment. Gadolinium and terbium atoms adsorb on the oscillating quartz which leads to a change in its mass by Δm and therefore to a change in frequency Δf. If the ratio $\frac{\Delta f}{f_0}$ is small, equation 4.1 can be used [48].

$$\Delta f = -\frac{2 \cdot f_0^2}{A \cdot \sqrt{\rho_q \cdot \mu_q}} \cdot \Delta m \tag{4.1}$$

explains the dependencies with f_0 as natural frequency of the quartz, μ_q its shear modulus and ρ_q its density. A is the surface area of the the quartz where evaporated material can adsorb. Based on this, the coverages in this thesis are all given in the unit Hz, referring to the change in frequency of the QCM during deposition.
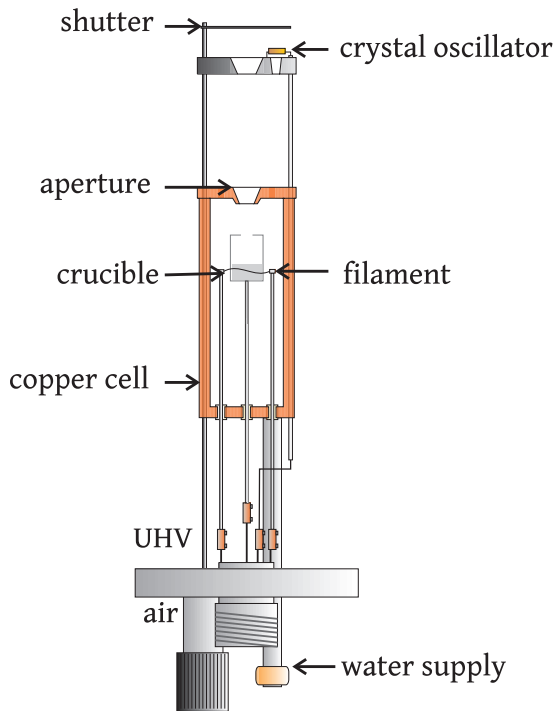

Figure 4.2: Schematic drawing of evaporator, taken and changed from [13]. The vaporization material is located at a crucible which is open in the direction of the sample. Next to the crucible, a spiral filament is placed on which a voltage is applied for heating. By this heating process, electrons are emitted to the crucible from the filament and are accelerated by another voltage to the crucible. Thereby, it and the vaporization material in it get heated and desorb too. They are moved towards the shutter and the QCM. By opening the shutter, one can vaporize towards the sample.

4.3 SPA-LEED

In the following chapter, the experimental setup of SPA-LEED is presented. SPA-LEED is a specified application of LEED. In contrast to LEED, in SPA-LEED a variation of the incident angle is possible. Therefore, the (00)-reflex can be detected too, because no electron gun is to be placed between detector and sample. The $\vec{k}$-space can be scanned laterally in the area of the (00) reflex.

The electrons used in SPA-LEED normally have an energy of about 20 to 500eV. This equals to a DE BROGLIE wavelength in the area of typical atomic distances in crystal solids, 0.5Å to 2.7Å. For the used energy of 130eV, equation 2.10 gives an electron wavelength of $\lambda = 1.076$Å.

An electron source emits particles - the so called electron cannon, which consists of a filament, an anode and a Wehnelt cylinder, using the photoelectric effect. The particles are accelerated by an electric field and their direction can be defined by anode and electron beam energy. The focusing is controlled by the Wehnelt cylinder. After that, the electrons reach an area between octopol plates which are able to deflect the beam in a way that they reach the sample surface by an angle ε. Before that, a lens system can be used to focus the incoming beam again. The reflected beam is detected by a channeltron under the deflection angle α.

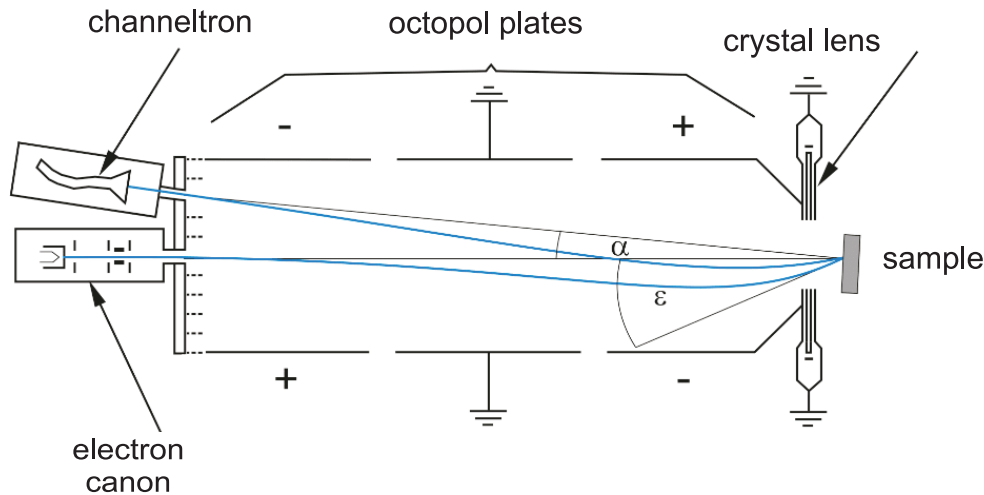Figure 4.3 shows a schematic sketch of the experimental setting of SPA-LEED optics.

Figure 4.3: Experimental setup of SPA-LEED apparatus. The electron cannon emits electrons, which reach the sample surface at the angle ε after passing through the field between the octopol plates and the crystal lenses. The diffracted beam from the sample travels back trough the fields in an angle α and reaches the channeltron detector. Taken and modified from [49].

The channeltron is installed at a fixed angle to the electron canon α. This leads to the experimental feature that the angle between incident wave $\vec{k}_0$ and reflected wave $\vec{k}$ is

constant and independent of the incoming angle ε. Reciprocal space can be scanned by varying the voltage applied to the octopol plates, thereby varying ε.

By varying the angle of incidence, the SPA-LEED can scan a larger area of $\vec{k}$-space. The Ewald circle can be constructed like shown in figure 4.4.
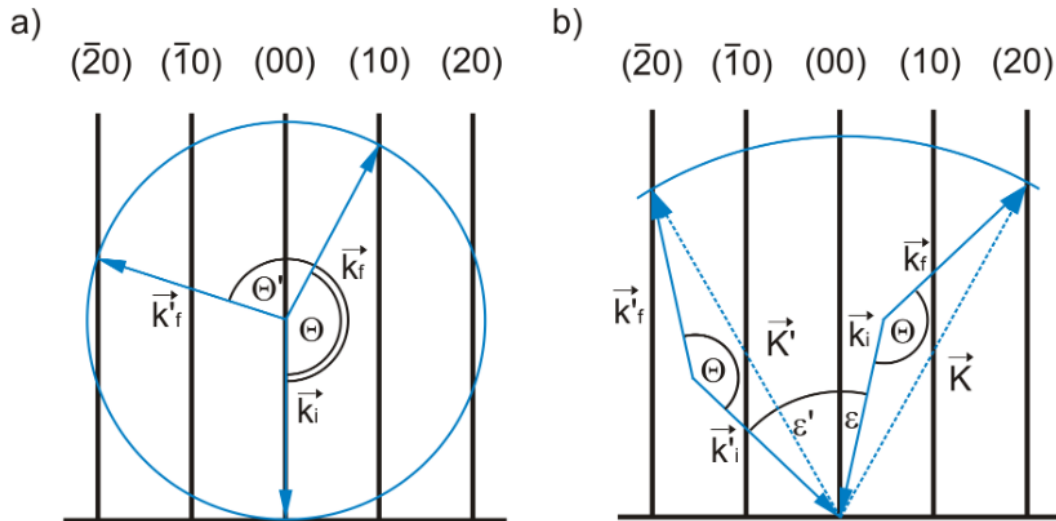

Figure 4.4: Construction of Ewald circle as a cut though reciprocal space shown for a) LEED optics (again for comparison, see chapter 2.2) and b) SPA-LEED optics. $\vec{k_i}$ and $\vec{k_i'}$ are incident wave vectors for different angles of incident, and the wave vectors of the reflected waves are $\vec{k_f}$ and $\vec{k_f'}$. b) shows diffraction with the same angle Θ between incident and reflected vector. K and K' stand for the resulting scattering vector. Taken from [49].

The measurement is carried out by a computer program named *SPALEED_Qt* developed by Henrik Wilkens at the working group of Professor Wollschläger at Osnabrueck University. It is able to take 2D- and 1D-scans, the second ones also called linescans.

With *SPALEED_Qt*, one is able to readjust the (00)-reflex into the center of the measurement scale, after centering by carefully changing the sample position. This is necessary for exactly scanning along the axis of the crystal structure.

The evaluation of these measurements is described in chapter 5.

5 Results and discussion

In this chapter, the measurement results are presented and interpreted. Firstly, the general analysis of the gained measurement data is explained in chapter 5.1, followed by a presentation of the results of the pure silicon (001) surface in chapter 5.2. Afterwards, chapter 5.3 examines the influence of several preparation conditions like substrate temperature during or after the deposition process, as well as the electron energy of SPA-LEED canon as measurement parameter. In chapter 5.4, the main coverage series for gadolinium in this thesis are presented and evaluated. Afterwards, two more coverage series and a XPS measurement are carried out for terbium in chapter 5.5. Chapter 5.6 adds additional measurements with a variation in flux manipulated by different evaporation power values.

A comparison and discussion of all results from chapter 5.4 to 5.6 follows in chapter 5.7.

5.1 Analysis of measurement data

The data were collected with commercial Omicron SPA-LEED Optics and the measurement program *Spaleed_Qt* developed by Henrik Wilkens at the working group of Professor Wollschläger at Osnabrück University. By this program, the *2D measurements* and the *linescan* can be conducted. After adjusting the sample in front of the optics, the linescan is recorded at a resolution of 1001 pixels (estimated about 8 pixels per %BZ) and an integration time of 100 milliseconds per pixel. The linescans have the lateral scattering vector $k_\parallel$ in percent *Brillouin* zone on the abscissa and are carried out along a main axis of the diffraction pattern. After that, the 2D scan is taken with a resolution of 401x401 pixels and an integration time of 1 millisecond per pixel. The linescans are evaluated by a program called *Peakorino* by Jascha Bahlmann at the working group of Prof. Wollschläger at Osnabrück University. Individual linescans can be distorted and fitted with an infinite amount of functions. In this case, a distortion correction is necessary because the field between the octopol plates is not homogeneous which leads to a distortion in the diffraction pattern. Image distortions generally occur owing to the characteristics of the experimental setup and/or the recording of the diffraction patterns. For more information about determination and correction of distortions and systematic errors in LEED see [50]. Firstly for all linescans, the intensity offset and slope can be set by *Peakorino*. Afterwards, peaks in the signal are identified and assigned Lorentz functions. The main (00) reflex is fitted with two functions, the central peak and the broadening, as well as the reflex at 100%BZ. The rest of intensity maxima in the signal are only assigned to one function. Sharp reflexes indicate areas with long range order (see chapter 2.3). Due to symmetrical reasons, only the side with the clearer diffraction pattern is analyzed, either the range of positive or negative lateral scattering vector. Theoretically, both sides of the diffraction pattern are identical, but experimentally most times one side shows a clearer pattern than the other. This varies for every coverage series and is given at each chapter.

The graphical user interface (GUI) of *Peakorino* is shown in figure 5.1. In this example, a coverage series with 17 different coverages from 0Hz to 350Hz was loaded into *Peakorino* for fitting. The example coverage of 240Hz displayed in the figure shows the positive part of the lateral scattering vector axis from 0%BZ to 100%BZ. The intensity profile was fitted with the use of 13 functions (list on the left bottom corner) at parameters visible on the right bottom corner of the GUI. The reflex at 0%BZ and 100%BZ were fitted with two functions, the rest of the reflexes each with one function. Only reflexes which appear significantly during the coverage series are taken into account. On the right top corner, different parameters can be displayed in dependency of the coverage. These parameters are *intensity*, full-width-half-maximum (*FWHM*), position (*lateral scattering vector*), *offset* and *slope* among others. As parameter *exponent*, for all evaluations in this thesis a value of 1.5 is chosen which stands for a line profile of a two-dimensional LORENTZ function.
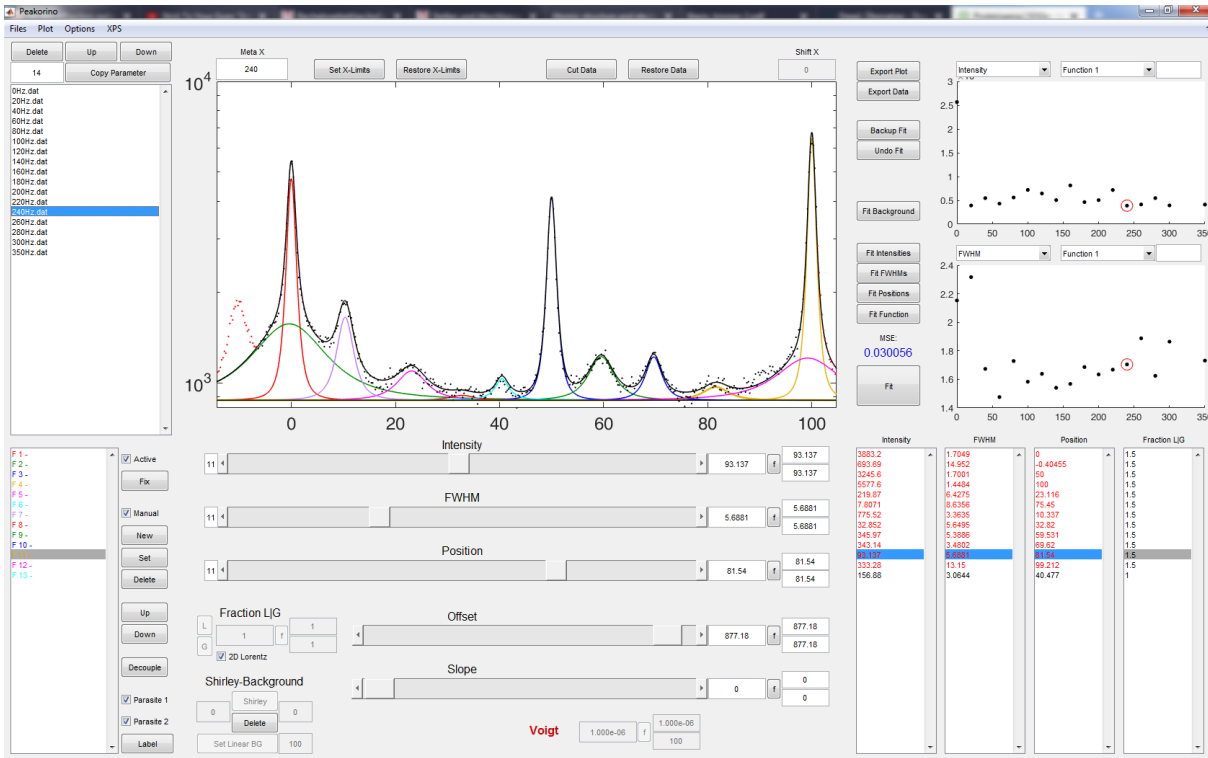

Figure 5.1: Fitting Graphic User Interface (GUI) of Matlab Program *Peakorino*. An example coverage series with 17 coverages from 0Hz to 350Hz is loaded and the linescan of 240Hz is shown as an example with 13 fitting functions and their parameters. Measurement points are displayed as dots and all parameters can be optimized manually or automatically by RMSE. The black line stands for the sum of all fractions of the intensity at that lateral scattering vector and is meant to fit the course of measurement points. Red measurement dots are not considered for fitting.

For every coverage series, the presentation of the results was done in the following way. Firstly, a 3D plot shows the distorted intensity courses in dependence of the lateral scattering vector in %BZ (see chapter 5.4, figure 5.12). The intensity values were normalized to the absolute intensity of the maximum value of the reflex at 0%BZ. The linescans are

shifted against each other for better visibility. Secondly, selected 2D diffraction patterns of different coverages are presented to show the approximate development of reflexes and to estimate the background noise as well as detecting streaks caused by nanowires on the sample surface. Afterwards, intensities and FWHM of individual reflexes are displayed in dependence of the coverage. Hereby, associated reflexes and symmetries determine which reflexes are shown in one diagram. FWHM courses for reflexes at 25%, 50% and 75%BZ are separately displayed in the following. Finally, for some coverage series, the development of the average groove-to-groove distance of nanowire bundles connected to some individual reflexes in $a_{Si(001)}$ were displayed in dependence of the coverage in Hz.

5.2 Substrate Si(001)

For every new substrate, a SPA-LEED measurement of the Si(001) surface was done. Figure 5.2 shows a 2D LEED pattern of the surface after flashing in UHV and before starting an evaporation process. The measurement was carried out at room temperature.

Figure 5.2: 2D SPA-LEED scan of substrate Si(001). The scan shows the (2x1)-reconstruction of the Si surface as consequence of dimer-structure due to unsaturated bindings (see chapter 3.1). This figure shows two rotational domains related by a 90° angle which lie one above the other. They exist because of a 90° rotation between atomic steps occurring on surface. The red arrow shows the scan axis used for the linescan in figure 5.3. An electron energy of 130eV was used.
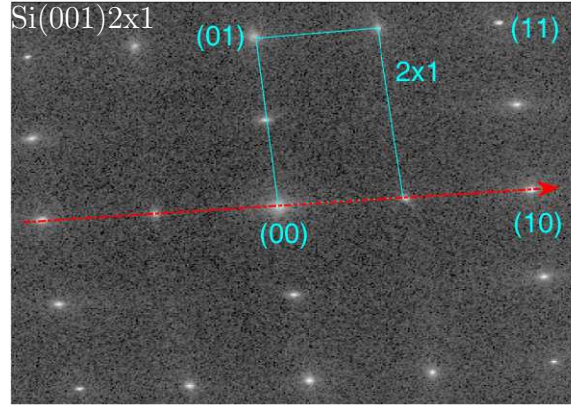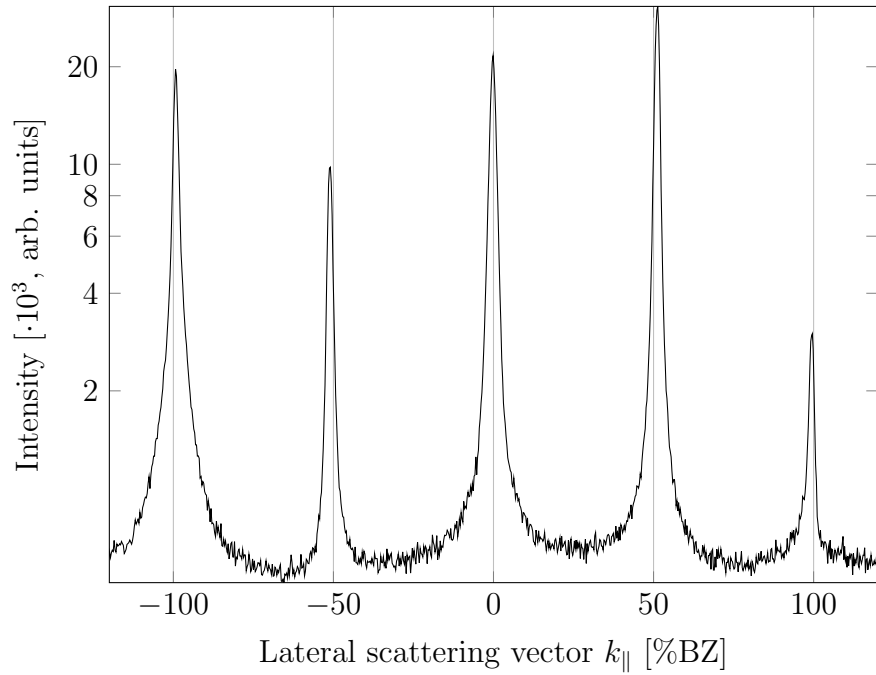
Figure 5.3: 1D scan of substrate Si(001). The scan axis is shown by the red line in figure 5.2. Reflexes at ±50% and ±100%BZ indicate a (2x1) reconstructed surface structure. This is the expected result for a Si(001) surface.

As explained in chapter 2.3, an electron energy of 130eV belongs to an out-phase of the spot profiles. Therefore exist both sharp peaks and a distinctive shoulder in this intensity profile shown in figure 5.3. The low FWHM of the 0%BZ central peak indicates a high domain size. FWHM here lie in a range of 1.5% to 2%BZ, which would refer to a domain size of about 19 to 25nm.

5.3 Pre-examination of Gadolinium-induced superstructures

The first of two rare earth elements used in this research is gadolinium. Due to resemblance in chemical and physical properties, the pre-examination to determine exact measurement conditions was only performed on gadolinium. For the comparability of gadolinium and terbium see chapter 3.4. After pre-examination, three coverage series with Gd follow, taking the results gained so far into consideration (chapter 5.4), firstly explaining the way of analysis and interpretation of these coverage series.

This chapter explains the preliminary examination measurements on Gd in a mostly chronological order. The dependence on preparation conditions like sample temperature and post annealing are examined, as well as detection properties like SPA-LEED electron energy. All coverages are given in the unit of $[\frac{1}{s}]$, which is based on the way to define the amount of deposited material by a change in mass on a quartz crystal microbalance (see chapter 4.2).

5.3.1 Electron energy of SPA-LEED

The next varied parameter is the energy of the electrons that are emitted by the electron gun in the SPA-LEED apparatus. The measurements were carried out with a sample of 60Hz and an electron energy range of 50eV to 170eV in steps of 20eV. The results are shown in figure 5.4. At 50eV, an indistinct diffraction pattern of a (2x1) surface structure can be guessed. It is slightly sharper for 70eV and additionally, reflexes of a (2x4) reconstruction are visible. With further increasing energy, the visibility of these reflexes increases until 130eV. For further increasing electron energy, the image starts to blur again and clear structures start to vanish, probably caused by unsuitable settings at SPA-LEED. Probably, the reflexes of a (2x4) structure exist more or less distinct in all diffraction patterns, only for some energies, the quality of the pattern is too low. The area around the reflex at (00) is darkened most intensely at 110eV, indicating that at this energy, some reflexes in this area are suppressed. The lens settings only seem to fit properly for an electron energy of 130eV. This measurement is important, because intensities of reflexes are dependent on the electron energy. The most fitting value is found when no reflexes are suppressed due to multiple scattering or the influence of different terraces on the surface. This measurement makes sure, that no reflexes are overlooked.

Additionally, 130eV is an out-of-phase electron energy here (see chapter 2.3). For an in-phase energy, the measurement would not be sensitive to surface steps, whereas it is step-sensitive for an out-phase confirming that 130eV is suitable for further measurements.
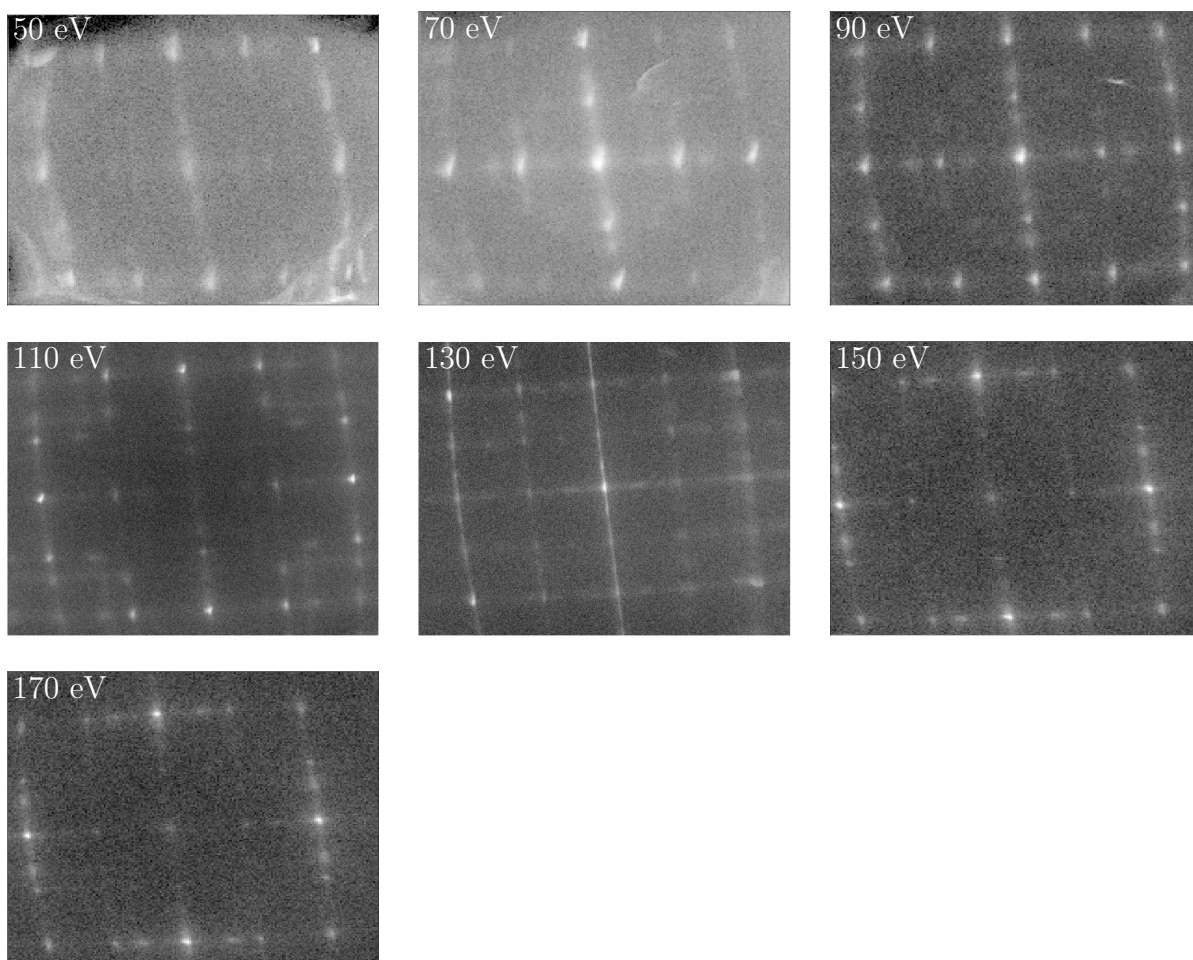
Figure 5.4: 2D scans with different SPA-LEED electron energies from 50eV to 170eV in steps of 20eV. The visibility of diffraction pattern reflexes increases up to 130eV with its clearest presentation. Afterwards, the sharpness of the diffraction pattern decreases up to 170eV.

5.3.2 Sample temperature during evaporation

Additionally the sample temperature during evaporation was varied. Like described in chapter 4.2, the sample can be heated with a direct current via two pins connected to the sample holder. In contrast to experimental methods of other research groups in this field [34, 37–39], the sample was heated *during* evaporation and deposition process, and direct current was turned off directly afterwards. The selection of heating temperatures was made based on former research on this subject [14, 34, 38], performed mostly at about 500°C to 600°C. For this reason, a temperature range of 400°C to 700°C with a step size of 100°C was chosen. The other parameters are a coverage of 80Hz and an evaporation power of 42W. The axis of the linescan is marked in red at the 2D picture. It is the same axis for all four measurements.
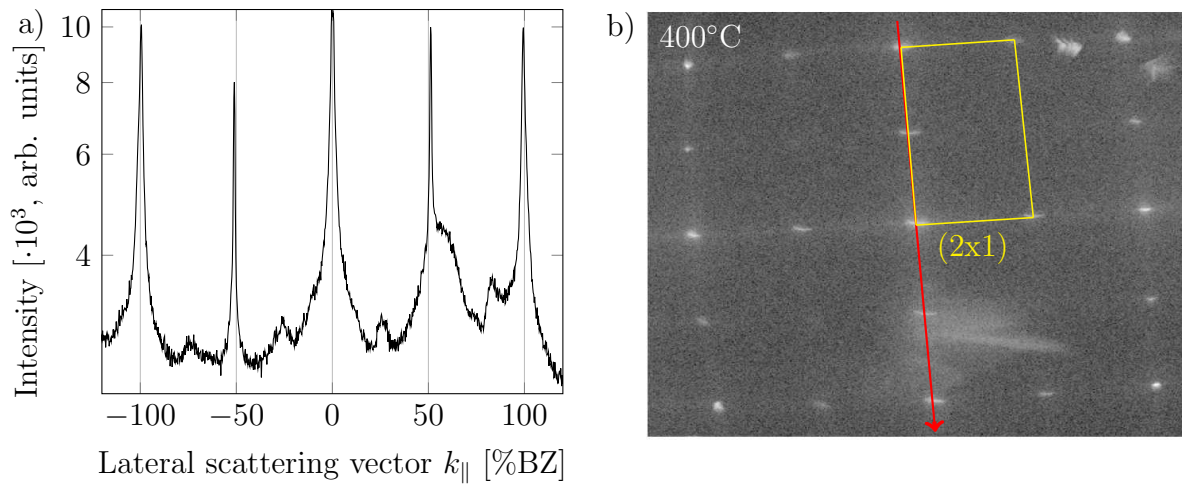

Figure 5.5: a) Linescan and b) 2D scan of coverage of 80Hz, an electron energy of 130eV and a sample temperature of 400°C during deposition and the corresponding scan axis is marked with a red arrow and the (2x1) structure in yellow. The 2D scan shows a (2x1) structure as known for a reconstructed Si(001) surface. The linescan reveals, additionally to the reflexes of the (2x1) superstructure, peaks at $\pm 25\%$BZ and $\pm 75\%$BZ which could originate from the well known (2x4) superstructure [37].

The results of the SPA-LEED measurement at a sample temperature of 400°C during deposition are shown in figure 5.5. The 2D scan indicates reflexes only at 50%BZ, whereas the more detailed linescan shows additional reflexes of lower intensity at 25%BZ and 75%BZ resulting from the (2x4) superstructure. In the lower part of the 2D picture, one can see some noise intensity of unknown origin. It can as well be seen on the positive side of the abscissa in the linescan. These intensities have no further meaning for the diffraction pattern and the surface structure. As a result, one can possibly conclude that at 400°C, the surface partly consists of amorphous islands and partly of the (2x1) reconstruction (yellow). It could be an explanation that the sample temperature during deposition is too low for further structuring, which at this point seems more probable than too little RE material being on the surface. The (2x4) structure described in chapter 3.4 has not been able to build widely on the Si(001) surface.
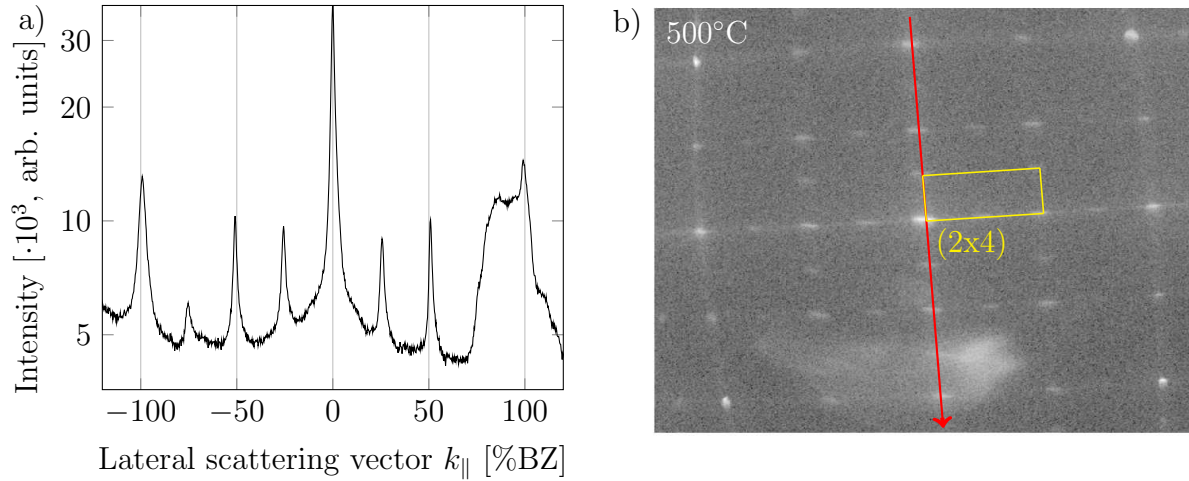
Figure 5.6: a) Linescan and b) 2D scan of coverage of 80Hz and a sample temperature of 500°C during deposition and an electron energy of 130eV. The used scan axis is again marked with a red arrow. The 2D scan shows a (2x4) structure marked in yellow. Sharp reflexes are visible at $(0,\frac{1}{4})$, $(0,\frac{1}{2})$, $(0,\frac{3}{4})$ and symmetrical equivalents in the 2D scan.

The SPA-LEED measurement with a sample temperature of 500°C during evaporation is shown in figure 5.6. In the 2D scan in b), reflexes of the (2x4) superstructure can be seen at positions of $(0,\frac{1}{4})$, $(0,\frac{1}{2})$, $(0,\frac{3}{4})$ and equivalents of symmetry. The corresponding linescan in a) confirms this observation. Reflexes at $\pm25\%$, $\pm50\%$ and $\pm75\%$BZ are recognizable, with lower intensities as the reflexes at $\pm50\%$BZ, probably resulting of a superposition of the diffraction patterns of (2x1) and (2x4) structures on the surface. The cause of the noise at the positive end of the linescan axis can again not be identified.

In figure 5.7, the experimental results of the measurement at a sample temperature of 600°C during deposition are displayed. b) shows the diffraction pattern with a (2x1) superstructure, reflexes additional to that can hardly be identified. A (2x4) structure can only be guessed. On the other hand, the linescan shows reflexes at $\pm25\%$ and $\pm50\%$BZ. To $\pm25\%$BZ corresponding reflexes at $\pm75\%$BZ are not clearly visible. Again, reflexes at $\pm50\%$BZ show higher intensities than those at $\pm25\%$BZ. This can be explained again by a superposition of the diffraction pattern of (2x1) and (2x4) areas on the sample surface. On the positive end of the linescan axis, again areas of increased intensity appear caused by unknown factors.

Figure 5.8 displays the measurement results for a sample temperature of 700°C during the evaporation process. The 2D scan in b) shows reflexes of a (2x1) superstructure which is supported by the linescan with sharp and intense reflexes at $\pm50\%$BZ. The missing superstructures expected for Gd can be explained by two factors. Firstly, it is possible that the temperature is too high for Gd atoms to adsorb at the surface. Secondly, island growth could take place on the surface due to intensified diffusion (see chapter 2.1.3).

At both measurements with 600°C and 700°C there is some additional intensity around 100%BZ. This noise in intensity probably has its cause in the SPA-LEED optics. Perhaps, lenses were not adjusted properly and it could be that electrons are reflected somewhere
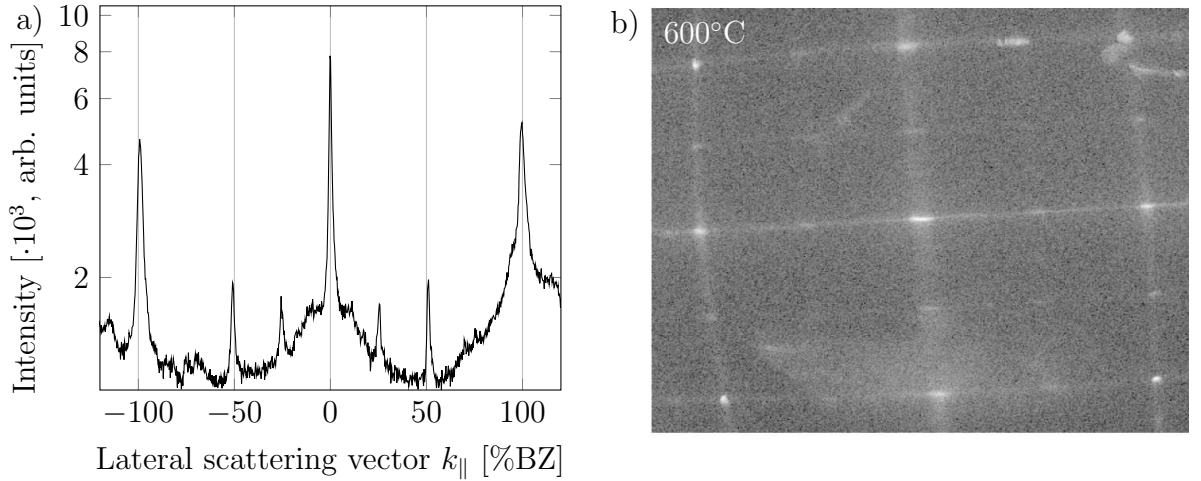
Figure 5.7: a) Linescan and b) 2D scan of coverage of 80Hz and a sample temperature of 600°C during deposition. The linescan axis is analogous to the one marked in 5.5 and with a red arrow, the used electron energy is 130eV. The diffraction pattern shows mainly a (2x1) with high noise. Sharp reflexes in the diffraction pattern are visible only at $(0,\frac{1}{2})$ and $(0,-\frac{1}{2})$, whereas a (2x4) structure can only be guessed. The linescan however shows clear reflexes additionally at 25%. Corresponding reflexes at 75%BZ can not be identified. In the area of the positive lateral scattering vector, again some increased background noise is observable.

besides the sample surface, e.g. the sample holder. But origins of this intensity are unclear.

These four measurements show that there is a strong temperature dependence for the growth of Gd structures on Si(001). If the temperature during Gd deposition is too low or too high, no (2x4) superstructures can here be observed with SPA-LEED at these coverages. Probably, lowest temperatures do not allow ordered structures to grow on the surface. That means either there is no Gd adsorbed on the surface or that the growth happens in a way that no diffraction pattern e.g. of (2x4) structures can be achieved (e.g. due to island growth). At low temperatures, diffusion on the sample surface could be too slow to spread Gd atoms throughout the whole surface. This could lead to areas where there is not enough Gd to build (2x4) or (2x7) superstructures. More probably at low temperatures energy is too low to break former existing chemical bonds and create new ones, it does not reach the level of activation energy. At the measurement with a substrate temperature of 500°C during deposition, the (2x4) superstructure is far more distinctive than for 600°C. For the first coverage series in chapter 5.4 a temperature of 600°C was chosen based on other research [37, 40], as these measurements about temperature dependency of structure growth were chronologically performed after the first coverage series.

Other researchers dealing with rare earth material on Si(001) use temperatures of 500°C [39] and 600°C [37, 39, 40]. Experimental results of pre-examination and other papers indicate that further experiments should be done at about 500°C as performed in the coverage series in chapters 5.4 and 5.5.
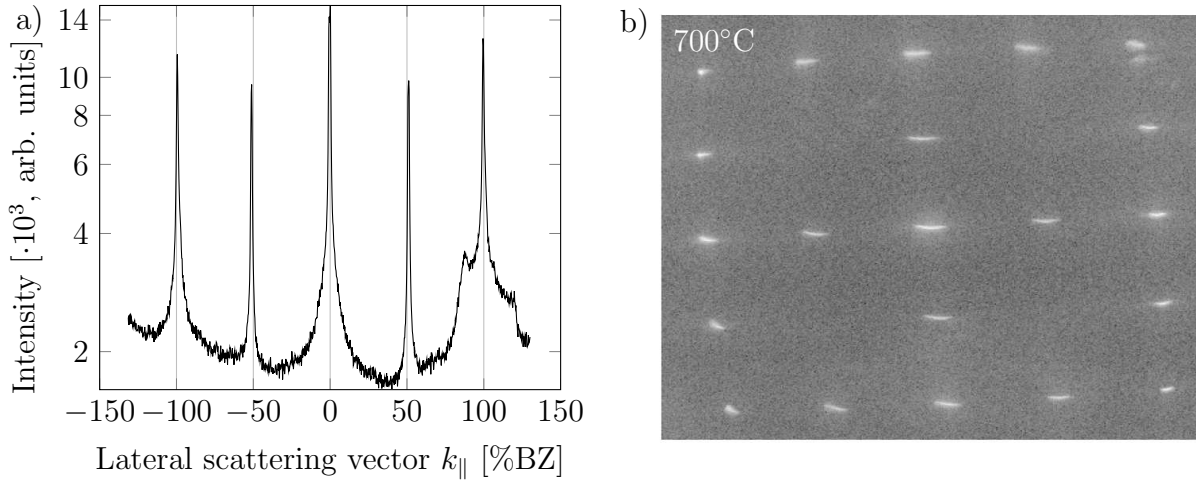
Figure 5.8: a) Linescan and b) 2D scan of a sample with a coverage of 80Hz, a sample temperature of 700°C during deposition and an electron energy of 130eV. The linescan axis is analogous to figure 5.5. The diffraction pattern shows a (2x1) structure, the linescan clear and very intense reflexes at 50%BZ. At the positive end of the abscissa, again some background noise intensity appears (at about 100%BZ).

5.3.3 Post-annealing

Similar research is performed with the sample being heated during deposition and subsequently. (at 500°C [38, 39], 600°C [37, 38, 40], 650°C and 700°C [38]). Heating the sample after deposition is called *post-annealing*. LIU and NOGAMI for example deposit dysprosium at a sample temperature of 600°C and post-anneal for several minutes afterwards [40]. To identify the influence on the measurements in this thesis, post-annealing was performed at two different coverages, two different temperatures and two different post-annealing durations. 2D scans are used to evaluate the influence on the surface structure.

Samples with coverages of 80Hz and 200Hz were examined. Both coverages were prepared firstly at a temperature of 500°C only during deposition, and secondly with the same temperature during and for about two minutes after deposition. The result is presented in figure 5.9. At 80Hz, the 2D scan shows a (2x4) structure with a high background noise rate. In comparison to a measurement without post-annealing in figure 5.6, the quality of the diffraction pattern is decreased with longer heating duration.

The measurement with a Gd coverage of 200Hz in figure 5.9 shows reflexes at (0,0), (0,1) and equivalents due to symmetry as well as streaky intensity along the main axes.

This could indicate that an elongation of heating time a few minutes after deposition does not necessarily lead to sharper reflexes and a more ordered surface, but here to higher background signal.
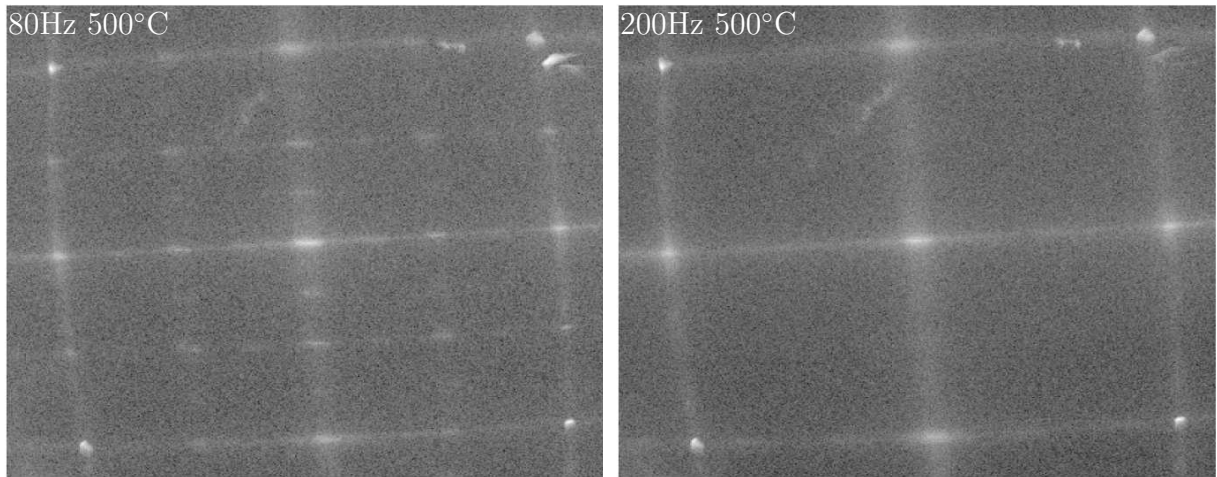
Figure 5.9: 2D scans of post-annealing at 500°C and coverages of 80Hz & 200Hz. The 2D scan of 80Hz shows reflexes of a (2x4) superstructure with a high background noise. The scan with a Gd coverage of 200Hz shows streaks on the main axes without any reflexes besides (00), (01) and symmetry equivalents. An electron energy of 130eV was used.

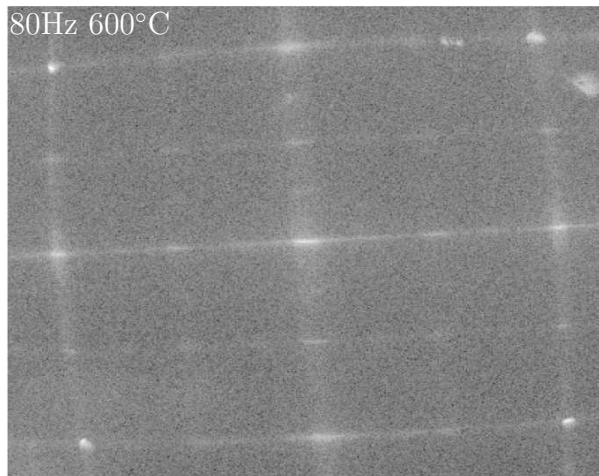In figure 5.10, the 2D result of a measurement with a coverage of 80Hz and a temperature of 600°C is shown. The heating process took place during and 2 minutes after deposition.

Figure 5.10: 2D scan of a sample with a coverage of 80Hz and a SPA-LEED electron energy of 130eV. It was heated during and two minutes after the deposition process at a temperature of 600°C.

For examining the influence of temperature, one can compare it to the coverage of 80Hz in figure 5.9. Figure 5.10 shows a (2x4) superstructure too, but with more noise signal and a lesser contrast for the reflexes. One can conclude that under these conditions, an increase of temperature from 500°C to 600°C does not have a positive impact on the formation of long range and well ordered (2x4) or (2x7) structures on the surface. Even though, the diffraction pattern of this measurement at 600°C shows better structures than the one without post-annealing displayed in figure 5.7, but both with low quality diffraction patterns. Additional time with elevated temperature could have led to a better reorganization of the surface.

The last varied parameter in post-annealing measurements is the length of post-annealing time. For this comparison, durations of 5 minutes and 10 minutes were chosen. Results

are displayed in figure 5.11. This measurement was done after a repair of the SPA-LEED lenses that lead to sharper reflexes in general. They are not related to a variation in experimental parameters examined in this chapter. The left side shows the 2D scan of a 5 minutes post-annealing with reflexes at $(0,0)$, $(0,\frac{1}{2})$, (01) and symmetric equivalents on the main axes. Besides the main axes, no structures can be identified. With an increased post-annealing duration to 10 minutes, the intensity of the whole diffraction pattern decreases, indicating a far less ordered surface which was created during the additional 5 minutes of heating in the second experiment. During these additional minutes of post-annealing, different effects could cause the decrease in structure quality. Firstly, the structure could be unstable and could be (more) destroyed again after additional time. A second possible explanation could be a diffusion of the adsorbates away from the surface and into the solid silicon or a desorption from the surface into the vacuum. This would imply that the structure has not been in an energy minimum before. Another possible reason could be that other trace gas atoms adsorb on the sample surface and thereby destroy the Gd silicide surface structure.
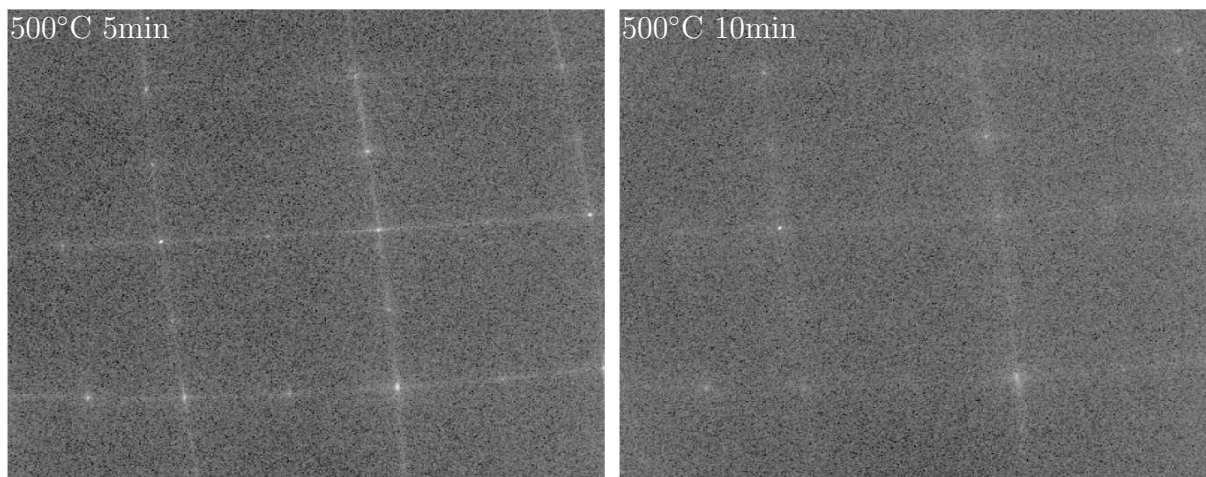

Figure 5.11: 2D scans of measurements at 500°C with a coverage of 80Hz and a post-annealing duration of 5 minutes and 10 minutes. The electron energy was 130eV. For five minutes, the reflexes of a (2x1) structure are clearly visible on the main axes, with higher intensity than after 10 minutes.

5.4 Series of coverage with Gd

The first three coverage series were done with gadolinium as Rare Earth material, the last two in chapter 5.5 with terbium. Chronically, the results for an ideal temperature range of 500°C were achieved after the first two coverage series. This is the reason why in the following coverage series, a sample temperature of 600°C during deposition was chosen based on the results of other research groups [33, 37].

5.4.1 Coverage Series I

The evaporation power for this coverage series is 35W. Evaporation times lie in a range of 52 seconds for 20Hz to 54 minutes for 1000Hz.
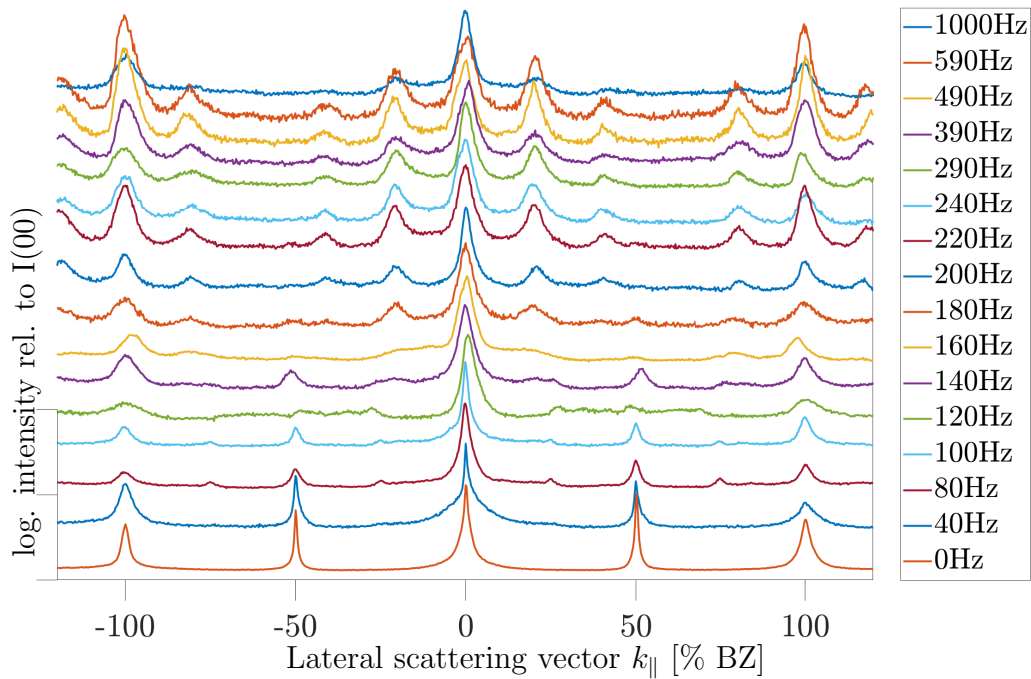

Figure 5.12: 3D presentation of linescans of coverage series 1. The abscissa gives the lateral scattering vector in %BZ, the ordinate the intensities normalized to I(00). The linescans are shifted against each other to ensure a clear arrangement. Equidistant step sizes of 20Hz up to 240Hz (without 20Hz and 60Hz) and of 50Hz up to 390Hz with additional measurements at 490Hz, 590Hz and 1000Hz. The closer to the abscissa, the lower the coverage.

3D presentation of all linescans of coverage series 1 are shown in figure 5.12. The abscissa gives the lateral scattering vector in %BZ, the ordinate the intensity relatively to the maximum intensity of the 0%BZ reflex in the same linescan. Linescans are shifted against each other for better visibility, the lowest coverages are presented closest to the abscissa. Coverages were chosen equidistantly up to 240Hz in steps of 20Hz without 20Hz and 60Hz,

afterwards with a step size of 50Hz to 390Hz, steps of 100Hz to 590Hz and an additional measurement at 1000Hz.

For low coverages up to 40Hz, besides 0%BZ and $\pm$100%BZ reflexes, at $\pm$50%BZ is the only intensity peak, indicating the presence of a (2x1) reconstruction on the sample surface. With increasing coverage up to 120Hz, reflexes probably corresponding to a (2x4) surface structure appear with additional small reflexes at $\pm$25% and $\pm$75%BZ. When having coverages of 120Hz and higher, former reflexes vanish and new ones at about $\pm$20%, $\pm$40% and $\pm$80%BZ appear. They indicate the presence of a (x5) structure on the surface. Hereby, only the reflex at about $\pm$60%BZ is missing which could be suppressed at the used electron energy, because intensities of all possible (x5) reflexes are low in general. Up to 1000Hz, intensities of the reflexes decrease again but they are still visible.

The reflexes at 0Hz and 40Hz, the two measurements with lowest coverage, have low FWHM at 0%BZ and $\pm$50%BZ. The central peak of 0%BZ has a smaller FWHM and higher intensity than the rest of the coverage series. This indicates a clean structure and reflexes broaden when the substrate is covered with gadolinium. Therefore, the domain size of (2x1) domains for pure substrate and a nearly pure substrate at 40Hz is very high. Irregularities on the substrate surface can be assumed to be rare.

2D diffraction patterns

Figure 5.13 shows exemplary 2D diffraction patterns of the coverages 80Hz, 140Hz and 220Hz. They point out the development of structures throughout the whole coverage series. At 80Hz, the (2x4) structure expected from figure 5.12 can be seen, which gets blurred at 140Hz but is still visible. At 220Hz, on the main axes, a (x5) structure can be seen on both axes - horizontally and vertically. With increasing coverage, an increase in background signal and therefore a reduction in contrast can be noticed. This results from a lower degree of order on the surface and can be caused by longer deposition times. The difference of deposition times are about 10 minutes and potentially make it possible for trace gas atoms to adsorb on the surface.

Streaky intensities on the major and minor axes are visible in all three diffraction patterns in figure 5.13, indicating the existence of nanowire bundles on the surface.

Analysis of linescans

In this subchapter, the courses of normalized intensities and FWHM in %BZ of individual or related reflexes are displayed. Hereby, only the positive lateral scattering vector axis is considered since the negative part should contain the same information. Figure 5.14a) presents the values for the central peak (in the following: 0%BZ cp) of the reflex at 0%BZ, as well as for the reflex at 50%BZ. For normalization, intensities are divided by the maximum intensity of the 0%BZ reflex of the corresponding linescan and are applied to the left axis (red), FWHM to the right (blue). Values for the 0%BZ cp are displayed with triangle data points, whereas the 50%BZ reflex is shown with circle points. The abscissa gives the coverage from 20Hz to 700Hz. The normalized intensity and FWHM of 0%BZ cp stay at about the same level of about 0.6 and 5%BZ during the coverage series, with a slightly increasing tendency in the FWHM and decrease in the intensity. Fluctuations exist in the area up to 240Hz. The values for the reflex at 50%BZ show these
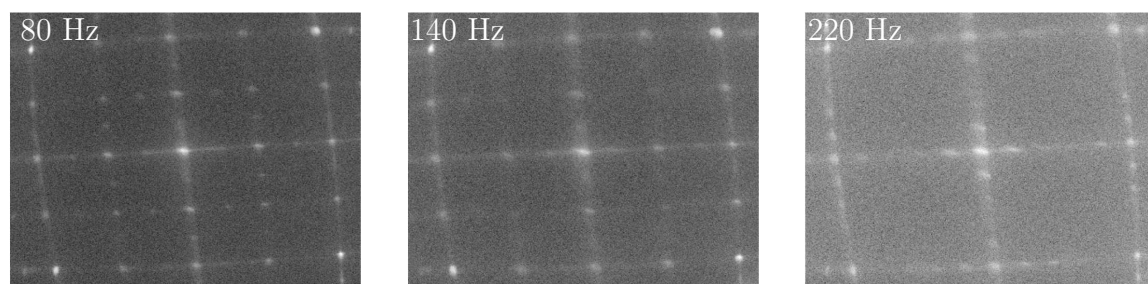
Figure 5.13: 2D representation of coverage series 1 for 80Hz, 140Hz and 220Hz. These coverages were chosen to represent important steps in the development of surface structures. At 80Hz, reflexes correlation with both rotational domains of a (2x4) structure can be seen on the surface, decreasing contrast and blurring up to 140Hz. At 220Hz, the (2x4) structure is completely gone and a (x5) structure on the main axes appears. With higher coverages, the background signal increases strongly, lowering the contrast of the diffraction pattern of remaining structures.

tendencies too, a linear decrease can be estimated in the intensity from 0.6 to 0.01 and a constant increase in the FWHM from about 5% to 15%BZ. This means, that for low coverages, a well ordered (2x1) structure exists on the surface. The adsorption of Gd leads to smaller domains on the surface, indicated by the decrease in FWHM. The decrease in intensities and an increase in background noise intensity visible in figure 5.13 let assume the appearance of more defects with increasing coverage. Due to the superposition of the diffraction patterns of (2x1) and (2x4) structures, no statements concerning these can be made based on the analysis of 0% and 50%BZ reflexes. In general, sharp reflexes indicate a high level of order and a long-range superstructure.

Figure 5.14b) shows a diagram with the intensities and FWHM of the central peak and the broadening fitting function (in the following: 0%BZ b) of the 0%BZ reflex. The central peak is therefore represented again for better comparison. The courses of intensities and FWHM of both fitting functions are similar. The values of normalized intensity of the central peak are higher than the one from the broadening, contrary to behavior for a strongly stepped surface. Also a logic consequence is that FWHM of the broadening function is higher than of the cp, at about 22% to 30%BZ. Intensities and FWHM of central peak and broadening are roughly constant. Intensities lie at about 0.6 for 0% cp and 0.06 for 0% b, FWHM of cp at about 5%BZ and of broadening at about 28%BZ. Based on a similar course of 0%BZ cp and broadening, one can assume a constant roughness of the surface (see chapter 2.3). It could indicate that no additional island growth took place during the coverage series.

Figure 5.15 shows the intensity and FWHM courses for the reflexes at 25%, 75%, 20%, 40% and 80%BZ. The grouping for display was chosen due to affiliation to certain surface structures: the reflexes at 25% and 75%BZ to a (2x4) reconstruction, 20%, 40% and 80%BZ to a (x5) reconstruction. The courses of intensity for 25% and 75%BZ show a very similar behavior with a minimum at about 240Hz and a maximum at about 100Hz. The minimum could indicate, that at this coverage, the corresponding surface structures are replaced by the (x5) structure. Correspondingly, the FWHM is low for small coverages
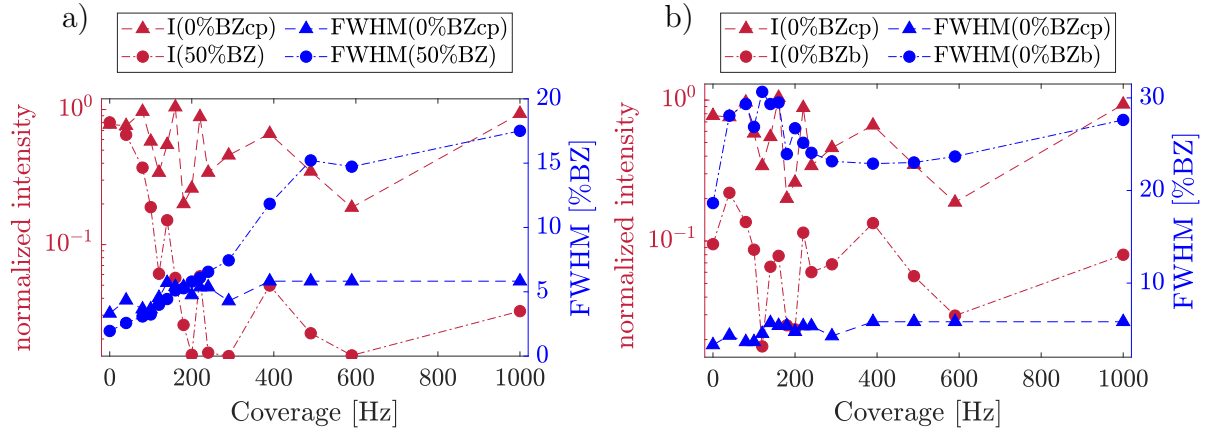
Figure 5.14: Coverage Series 1 - a) Intensity and FWHM courses for 0%BZ central peak and 50%BZ. It shows a similar course in the intensities for 200Hz and higher, only with a higher offset for the 0%BZ reflex. For 50%BZ, there is an increase in FWHM and a decrease in intensity. b) 0%BZ central peak and broadening show a constant behavior in FWHM and intensities, last ones with higher fluctuations for coverages from 0Hz to 240Hz.

from 80Hz to about 180Hz and increases linearly for higher coverages. Mainly lower intensities and higher FWHM until a coverage of about 200Hz indicate that the (2x4) structure exists on the surface for a wide coverage range with sinking quality for coverages above 180Hz and is replaced by other structures for highest coverages. This is supported by figure 5.13. The similar behavior for reflexes at 25% and 75%BZ is expected due to symmetric reasons.

Figure 5.15b) includes all three reflexes of which the positions indicate a (x5) surface structure. Only an expected reflex at 60%BZ is missing in the measurement results. Normalized intensity courses show similar behavior for the whole coverage series. The superstructure occurs in a coverage range from 180Hz to about 590Hz. The normalized intensity is low in the beginning, increases to 290Hz and afterwards shows constant behavior with a low decrease at 590Hz. The FWHM starts low except for the reflex at 40%BZ which can be caused by lower intensity values and thereby a bigger error range. Afterwards, FWHM stays at low levels for coverages of 220Hz and higher with a slow increase for higher coverages with a local maximum for 20%BZ and 80%BZ at 400Hz. The outlier in all three reflexes at 220Hz can be caused by an improper calibration of the scan axis, lying just beside the (0,0) reflex. This leads to a normalization to a value that is too low and therefor the resulting intensities are higher than they would be with a proper adjustment of the scan axis. The reflexes at 20% and 80%BZ could also belong to nanobundle structures on the surface [2], but due to existence of the reflex at 40%BZ one could assume that perhaps nanowire bundles coexist with the (x5) structure on the surface.

Figure 5.16 shows the FWHM courses of reflexes at 25%, 50% and 75%BZ in comparison. By analyzing these, one can draw conclusions concerning domain boundaries (see chapter 2.3). Because FWHM of all three reflexes are nearly identical, one can assume that
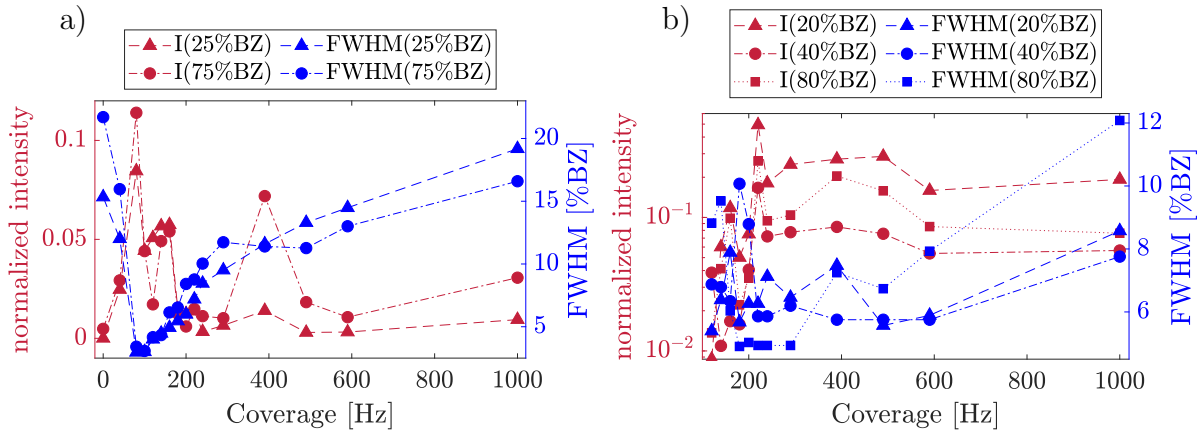
Figure 5.15: Coverage Series 1 - Normalized intensity and FWHM courses for a) 25% and 75%BZ and b) 20%, 40% and 80%BZ. Reflexes in a) are part of a (2x4) reconstruction and have high normalized intensities and low FWHM in the range of 80Hz to 180Hz, where the (2x4) is most present. b) shows the courses for reflexes assumed to be part of a (x5) structure. They mainly show a constant behavior from 240Hz to highest coverages. For low coverages, high FWHM and low intensities indicate a non existence of this structure.
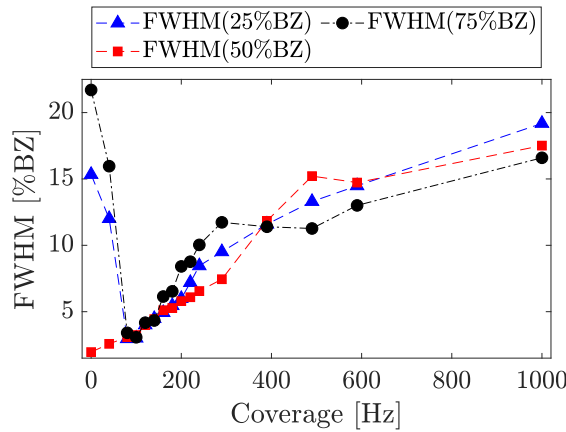
Figure 5.16: Coverage Series 1 - coverage dependency of FWHM for 25%, 50% and 75%BZ reflexes for comparison within (2x4) structure. FWHM of 25% and 75%BZ are minimal at about 100Hz and show a similar positive linear slope in average afterwards. For 50%BZ, the values start low for low coverages. Afterwards, the course of FWHM of all three reflexes is very similar.

different domain boundaries appear statistically. The reflex at 50%BZ for coverages of 0Hz to 100Hz has very low FWHM of about 1%BZ in contrast to the reflexes at 25% and 75%BZ with values of about 15%BZ. This indicates the existence of a (2x1) reconstruction for coverages from 0Hz to 100Hz which is replaced by a (2x4) structure indicated by similar courses of 25% and 75%BZ compared to 50%BZ above 100Hz. The (2x4) structure is very slowly decreasing for coverages above 100Hz.

In this coverage series, the evaporation and deposition duration was very high, up to an hour for 1000Hz. Therefore, the next coverage series, again with Gd as RE material, was performed with a evaporation power of 42W instead of 35W to shorten the deposition duration to hereby reduce possible disruptive impact of trace gases.

5.4.2 Coverage Series II

This coverage series was performed again at a sample temperature of 600°C, with an increased evaporation power of 42W for depositing Gd. By this, the evaporation duration was reduced to a range of 20 seconds for 20Hz to 210 seconds for 450Hz.
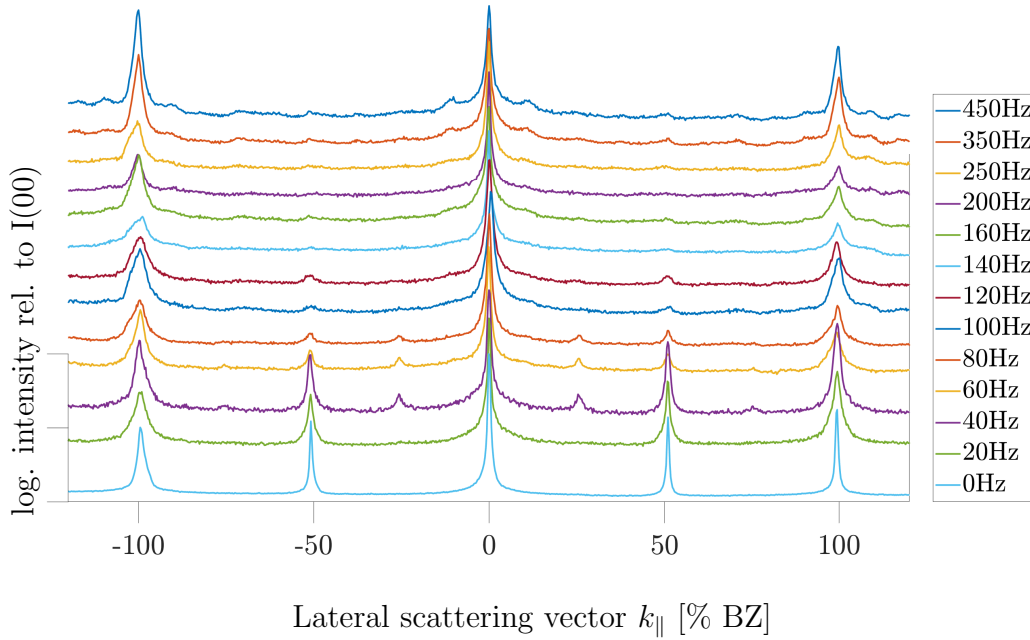

Figure 5.17: 3D presentation of linescans of coverage series 2. The abscissa gives the lateral scattering vector in %BZ, the ordinate the intensity normalized to I(00). Step sizes are 20Hz for coverages up to 160Hz, then additional measurements at 200Hz, 250Hz, 350Hz and 450Hz were performed. Linescans are shifted against each other for better visibility.

Figure 5.17 is the 3D presentation of linescans of coverage series 2. The abscissa again gives the lateral scattering vector in %BZ, the ordinate shows the normalized intensity, relatively to the maximum intensity of the 0%BZ reflex of the same linescan. Coverages from 0Hz to 160Hz and additionally at 200Hz, 250Hz, 350Hz and 450Hz are displayed. For evaluation, only the values of the negative lateral scattering vector axis were used and the measurement of 80Hz was left out due to deviating behavior of unknown cause.

For low coverages up to 40Hz, a (2x1) surface reconstruction is indicated by reflexes at ±50%BZ. With increasing coverage, a (2x4) pattern appears with broad reflexes at ±25% and ±75%BZ until about 80Hz. Afterwards, for coverages higher than 250Hz, low additional reflexes appear with lateral scattering vectors possibly correlating with a (x9) or (x10) structure of which origins are unclear. Due to bad quality of the correlating structure, it is not evaluated in the following.

2D diffraction patterns

2D diffraction patterns of two coverages were picked to show the development in the surface structures throughout the second coverage series in figure 5.18. At a coverage of 120Hz, reflexes with low intensities are visible at $(0, \frac{1}{2})$ and equivalents of symmetry at the same time as streaky intensity on the main axes. At 350Hz, reflexes correlating with a (2x1) reconstruction are gone and until there are only streaks on both axes at 350Hz, with visible reflexes only at (0,0) and (0,1) and equivalents of symmetry.
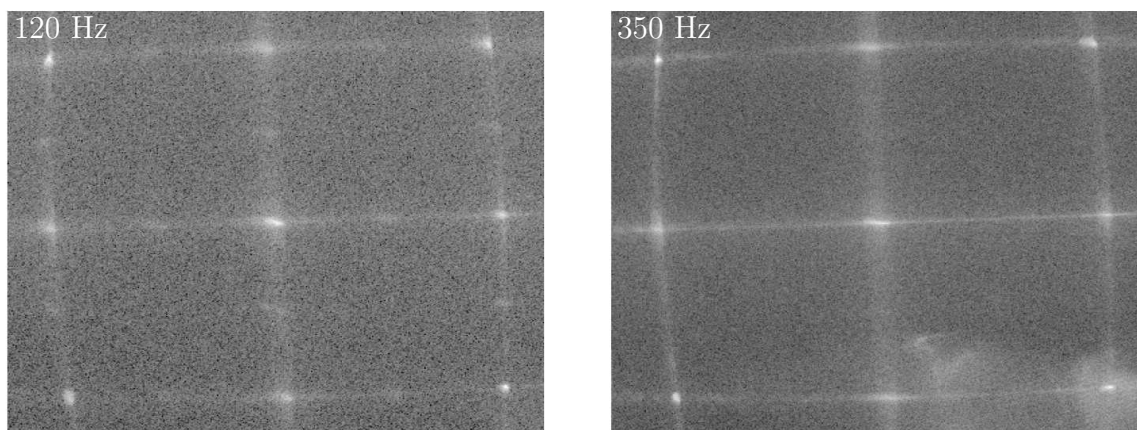
Figure 5.18: 2D representation of coverage series 2 for 120Hz and 350Hz. These coverages were chosen to represent important steps in the development of surface structures. At 120Hz, reflexes with low intensities are visible at $(0, \pm\frac{1}{2})$ and symmetry equivalents, which vanish with increasing coverage. Additionally to these reflexes, streaky intensity can be noticed on the main axes at both coverages.

Analysis of linescans

Intensity and FWHM courses of reflexes at 0%, 50%, 25% and 75%BZ were analyzed depending on the coverage. The reflexes at 0% and 50%BZ correlating with a (2x1) structure are displayed in figure 5.19 a). The intensities and FWHM of 0%BZ cp and the reflex at 50%BZ are displayed together. Intensity and FWHM of 0%BZ cp are constant, whereas the intensity of 50%BZ decreases for a coverage of up to 200Hz and increases a little afterwards. This is in accordance to the FWHM which starts with low values and increases to a maximum at 200Hz. Afterwards, the FWHM of 50%BZ decreases again gently. The coverage of 200Hz with the minimal intensity and maximal FWHM marks the limit to which the quality of the (2x4) structure decreases. The (2x1) structure probably does not exist anymore for these coverages, in accordance to coverage series 1. For higher coverages, the intensities of the reflex at 50%BZ increase again, probably caused by a (2x1) reconstruction on nanowires (see chapter 3.4).

In figure 5.19 b), the intensity and FWHM of the 0%BZ b reflex are displayed alone due to different value ranges. Its normalized intensity values lie in a range of 0.1 to 0.16 with no clear tendency. The FWHM of this reflex increases similar with increasing coverage and decreasing slope from 22% to 25%BZ. Increasing streaky intensity for increasing coverage

could have led to a wrong choice of offset at too high values and therefore to a higher error in FWHM for the reflexes resulting at lower FWHM. Possibly without this source of error, a linearly increasing course would occur. As described in chapter 2.3, the terrace width is reciprocally proportional to the FWHM of the 0%BZ b reflex. Over the coverage series, this FWHM only increases for about 10%, indicating that the surface roughness behaves constantly or only smoothly increases. For more reliable statements, one would have to do energy dependent measurements.
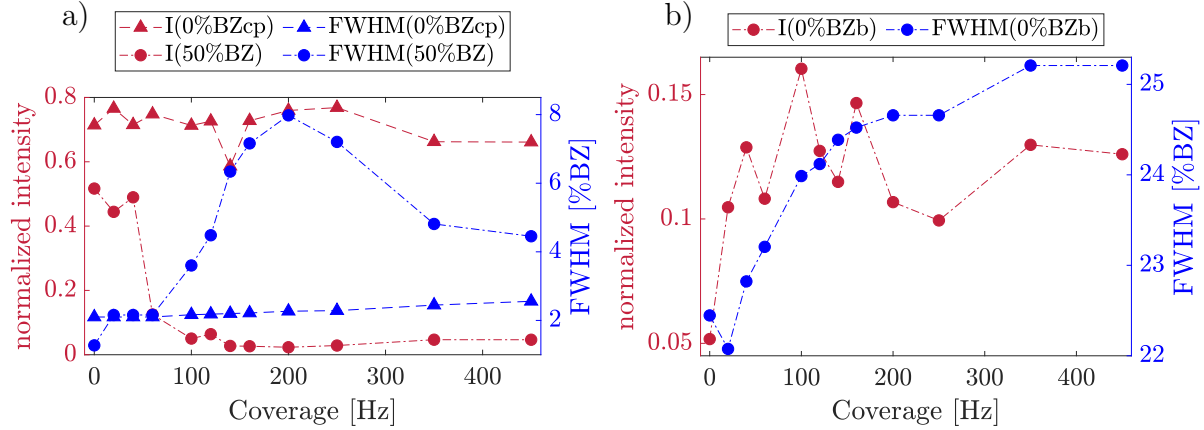
Figure 5.19: Coverage Series 2 - a) Normalized intensities and FWHM for 0%BZ cp and for 50%BZ. It shows a slight decrease in intensity and increase for FWHM of the 0%BZ cp and a significant coverage dependency in FWHM and intensity of the 50%BZ reflex. b) gives normalized intensities and FWHM for only the 0%BZ broadening reflex due to different value ranges. The FWHM of 0%BZ b increases with decreasing slope for increasing coverages, whereas intensity is constant with low fluctuations.

Figure 5.20 displays the measurement results for reflexes belonging to the (2x4) reconstructed surface. For coverages from 20Hz to 100Hz, the reflexes at 25% and 75%BZ show relatively high intensities (especially 25%BZ) and sink to a minimum between about 140Hz and 240Hz. Afterwards, intensities increase again smoothly. Increasing FWHM with increasing coverage can be identified to a maximum at about 240Hz and a smooth decrease afterwards. Consequently, a slowly decreasing (2x4) structure appears on the surface for coverages up to 140Hz to a minimum at about 200Hz. Normalized intensities smoothly increase again for highest coverages and FWHM decrease. That goes especially for 25%BZ, whereas for 75%BZ the FWHM nearly stays at the same level at about 8%BZ. The intensity values for 25%BZ are higher in the beginning, which could indicate a different occurrence of domain boundaries on the surface. Based on kinetic theory, reflexes at 25% and 75%BZ are expected to be similar, but intensities can vary due to dynamic effects [22]. For low coverages the low normalized intensities of the reflex at 75%BZ lead to a bigger error range in FWHM. The linescans in figure 5.12 show very small reflexes of a (2x4) surface structure.

This coverage series does not leave much to evaluate regarding superstructures on the sample surface. Only reflexes correlating with a (2x1) and afterwards a weak (2x4) reconstruction are visible for some coverages, but no further reflexes of additional structures could be detected within these SPA-LEED measurements.
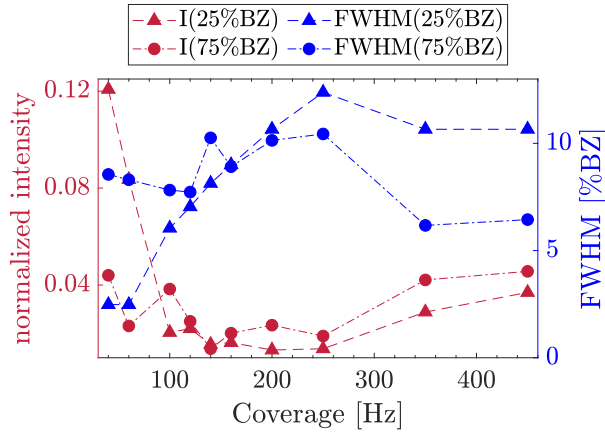
Figure 5.20: Coverage Series 2 - Normalized intensities and FWHM for 25% and 75%BZ reflexes. They indicate the growing presence of a (2x4) structure for up to 140Hz, nearly vanishing afterwards. Both reflexes show similar behavior in both evaluated values.
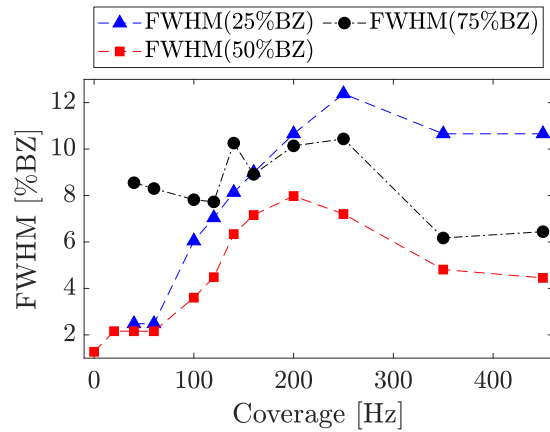
Figure 5.21: Coverage Series 2- FWHM of 25%, 50% and 75%BZ reflexes are displayed in one diagram for better comparison. For 0Hz, the reflex at 75%BZ starts at high values, whereas 50%BZ starts with low FWHM due to the (2x1) structure of pure Si(001). FWHM of 25% and 50%BZ increase from low values at 20Hz to 240Hz and stays about the same level with a slight drop at 350Hz. For 140Hz and higher, values ot the reflex at 75%BZ lie between 25% and 50%BZ.

The FWHM of all three reflexes belonging to (2x4) reconstruction (except 0%BZ) are displayed in one diagram in figure 5.21 for better comparability. All three courses show a maximum at about 200Hz to 250Hz. 50%BZ has the lowest FWHM for low coverages, because it belongs to the (2x1) reconstructed surface of pure Si(001) too. For higher coverages, its values still are lower than of 25% and 75%BZ reflexes. The reflex at 25%BZ shows higher FWHM of about 10% to 12%BZ for high coverages, whereas 75%BZ already starts with FWHM at about 8%BZ and only sinks to about 6%BZ for high coverages. Similar behavior and value range indicate, that these three reflexes belong to a (2x4) reconstruction which builds up to 200Hz of coverage and decreases in quality afterwards. Low intensities of reflexes lead to a bigger error range in FWHM, like the elevated FWHM level of the reflex at 75%BZ for coverages up to 120Hz. For a statistical distribution of domain boundaries, all peaks are expected to have the same FWHM. At lowest coverages from 20Hz to 80Hz, the (2x4) reconstructed surface possibly has the largest average domain size, but very low intensities make it difficult to make a valid statement.

After this coverage series, the pre-measurements for identifying an ideal substrate temperature during the deposition process were carried out. In doing so, a more suitable temperature of 500°C could be determined and was applied in coverage series 3.

5.4.3 Coverage Series III

Coverage series 3 was conducted with a sample temperature of 500°C during deposition. Like coverage series 2, an elevated evaporation power was chosen to reduce the duration of the process. This measurement is the third and last which was carried out with gadolinium as RE material for coverage. Deposition duration for this series is in a range from 30 seconds to 28 minutes with step sizes of 20Hz up to 300Hz and additional measurements at 350Hz and 500Hz.
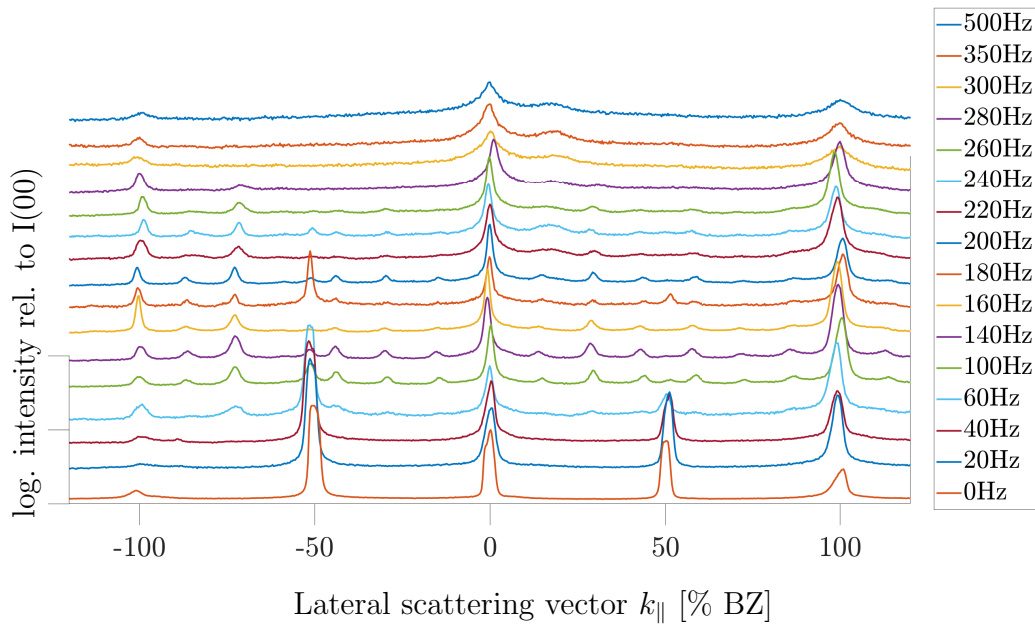

Figure 5.22: 3D presentation of linescans of coverage series 3. The ordinate gives the normalized intensity in dependence of the lateral scattering vector in %BZ on the abscissa. Coverage steps are 20Hz from 0Hz to 300Hz, with additional measurements at 350Hz and 500Hz. 80Hz and 120Hz were left out. The linescans are shifted against each other for better visibility.

Figure 5.22 displays the resulting normalized intensities in relation to the maximum intensity of the reflex at 0%BZ on the ordinate in dependence of the lateral scattering vector in %BZ on the abscissa. The linescans are shifted against each other for better visibility.

For 0Hz to 40Hz, intensity peaks at $\pm 50\%$BZ indicate a (2x1) reconstructed surface. With increasing coverage, additional intensity maxima appear at positions indicating a (2x7) reconstructed surface lasting until about 280Hz. Reflexes at $\pm 50\%$BZ superimpose with these. Afterwards, no maxima can be detected except at 0%BZ and 100%BZ. In the following, only the positive side of the lateral scattering vector is evaluated.

After coverage series 2, a readjustment of the SPA-LEED lens system was performed which leads to better focusing and sharper reflexes in the following measurements.

2D diffraction patterns

Exemplarily, 2D diffraction patterns of coverages 140Hz, 220Hz and 350Hz of coverage series 3 are displayed in figure 5.23. At 140Hz, reflexes correlating with a (2x7) reconstruction appear on the main axes. The (x2) periodicity is clearly visible by streaky intensity on the minor axes and most pronounced for 140Hz but still visible at 220Hz. For the appearance of (x2) periodicity see chapter 3.4. Here additional streaks on the main axes appear. At 350Hz, streaks become more continuous.
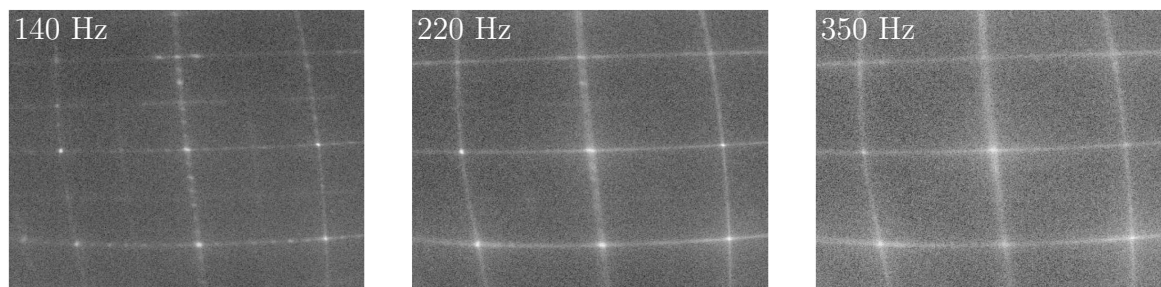
Figure 5.23: 2D presentation of coverage series 3 - Exemplary display of coverages 140Hz, 220Hz and 350Hz to represent the development in structures on the surface. At 140Hz, a (2x7) structure is visible with reflexes on the main axes. With increasing coverage, the reflexes decrease and streaks appear with rather constant intensity on the main axes at a coverage of 350Hz.

Analysis of linescans

In the following, intensity and FWHM for all appearing reflexes are analyzed. In figure 5.24 a), the 0% cp and 50%BZ peak are shown. The central peak shows steady behavior in intensity and FWHM with a slight decrease in intensity and growth in FWHM for coverages greater than 260Hz. For the peak at 50%BZ, the FWHM increases continuously from 3%BZ at 20Hz to about 10%BZ at 300Hz, indicating a soon decaying (2x1) structure on the surface. It is replaced by reflexes of the (2x7) structure respectively the streaky intensity at this lateral scattering vector for coverages of 100Hz and above. The (2x7) reconstruction probably decays smoothly with slowly decreasing intensity and increasing FWHM of the reflex at 50%BZ for coverages of 240Hz and higher. The intensity of the reflex at 50%BZ decreases for coverages from 0Hz to 140Hz and remains constant afterwards.

In general, normalized intensity for this peak shows a decreasing course from nearly 1 at low coverages to 0.02 for about 300Hz. (2x1) reconstruction has its largest average domain size for lowest coverages and decays up to 100Hz. It is replaced afterwards by a (2x7) reconstruction contributing to the intensity at about 50%BZ as well. But because reflexes of the (2x7) reconstruction have lower intensities, the FWHM values increase with increasing coverage. For other coverage series too, reflexes probably caused by a (2x1) reconstructed surface exist up to about 100Hz.

Figure 5.24 b) compares intensities and FWHM of both functions used for fitting the reflex at 0%BZ, central peak and broadening. The broadening peak shows constant behavior

in FWHM at about 15%BZ and intensity at about 0.1 for 0Hz to 260Hz and an increase in both parameters afterwards to 33%BZ and 0.4. The increase in FWHM of the 50%BZ reflex and decrease of intensity of the 50%BZ reflex with increasing coverage could hint at slightly higher roughness at high coverages. Due to comparability of both cp and broadening courses, one can probably assume that in this coverage series too, no significant change in surface roughness takes place during this series.
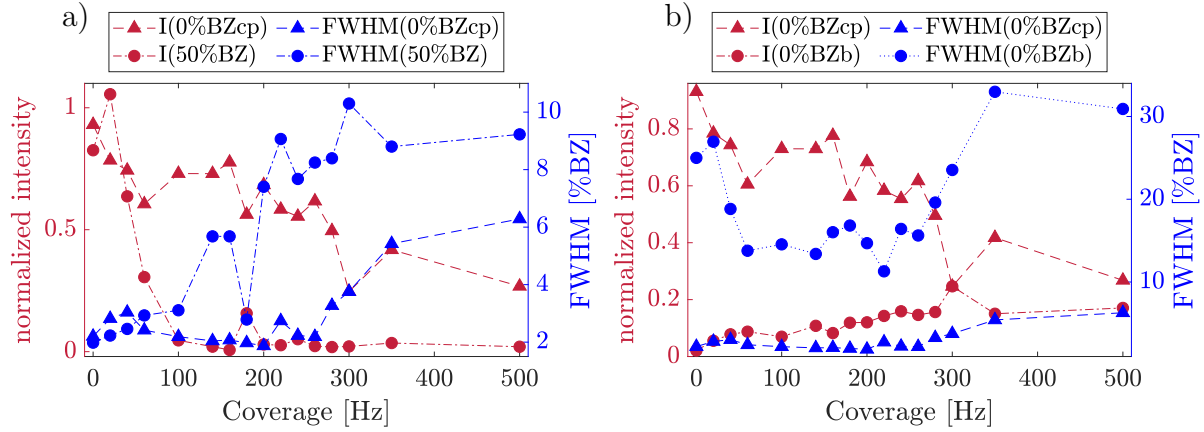

Figure 5.24: Coverage Series 3 - a) Normalized intensities and FWHM for the reflexes at 0%BZ cp and 50%BZ. In a) FWHM of 0%BZ cp shows constant behavior in FWHM and intensity up to 260Hz. Afterwards, the intensity slowly decreases and FWHM increases. The reflex at 50%BZ starts at high intensities and decreases up to 160Hz, afterwards staying about constant. FWHM are constant up to 100Hz and increase continuously afterwards. b) gives intensities and FWHM of 0%BZ cp and broadening. Intensities and FWHM of the 0%BZ broadening reflex are constant until a coverage of about 260Hz and slightly increase afterwards, especially in FWHM.

Figure 5.25 a) shows normalized intensities and FWHM for reflexes at 14% and 85%BZ. The normalized intensities start low for about 60Hz and show a very similar course with a maximum between 120 to 180Hz and decrease until 300Hz. FWHM of 14%BZ stays at about 5%BZ for the whole coverage series. The FWHM of 85%BZ starts at about 7%BZ and increases linearly with a slight slope up to nearly 12%BZ. Both reflexes are possibly resulting from a (2x7) reconstructed surface that exists for coverages from 40Hz to about 260Hz, mainly based on the parabolic course of the intensity with maximum values of about 0.07. But because FWHM are rather constant or increase linearly and intensities have low values, one could assume that there are some areas of (2x7) superstructures on the surface with a fixed size. Their number is highest for about 140Hz with normalized intensity of 0.08 and 0.1 and FWHM of 3%BZ and 6%BZ. It is to mention that intensities for (2x7) corresponding reflexes are very low in comparison to the intensities of the 0%BZ reflex.

Figure 5.25 b) gives the normalized intensities and FWHM of reflexes at 29% and 71%BZ, both showing a very similar course with a different offset. Normalized intensities start at about 0.01 and increase up to 0.1 for 120Hz to about 180Hz, decreasing afterwards with a slight slope. FWHM start at values of 7%BZ and sink to about 4%BZ for coverages from
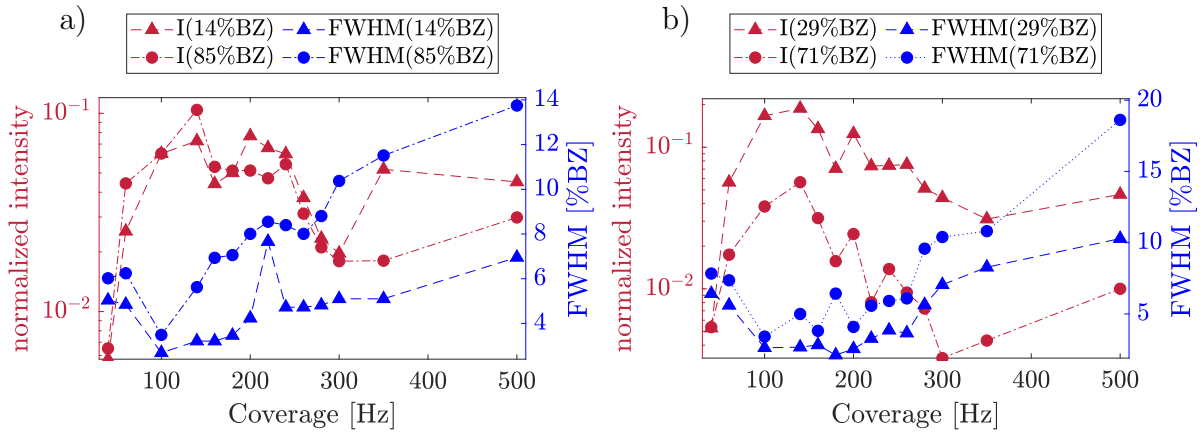
Figure 5.25: Coverage Series 3 - a) Normalized intensities and FWHM for 14% and 85%BZ. Normalized intensities show parabolic behavior with a maximum between 120Hz and 180Hz, whereas FWHM show parabolic behavior with a minimal value between 100Hz and 200Hz. b) gives normalized intensities and FWHM of reflexes at 29% and 71%BZ. Normalized intensities and FWHM show similar behavior like in a). FHWM have a minimum value of about 3%BZ between 100Hz and 180Hz. All four reflexes are attributed to a (2x7) surface structure. Correlating reflexes due to symmetry are displayed together.

100Hz to 200Hz. Values in this diagram indicate the best and most widespread structures for a coverage between about 100Hz and 200Hz too.

Normalized intensities and FWHM for 42% and 58%BZ are displayed in figure 5.26 a). They are presented together due to symmetrical reasons and both are considered to originate from a (2x7) structure. Normalized intensities as well as FWHM of the two reflexes show very similar behavior and values. Normalized intensities start low and develop parabolic with a maximum range between 100Hz and 240Hz at about 0.06. For higher values intensities decrease to nearly 0.01. FWHM show analogous behavior with minimal values of about 4% resp. 7%BZ in the same coverage range and increasing afterwards. In a range of 120Hz to 180Hz, probably most domains with a (2x7) superstructure and a fixed width exist on the sample surface with a normalized intensity of about 0.1 which decreases to about 0.01 for higher coverages. The same applies analogously to the FWHM. The similar course of FWHM of both the reflexes compared to figure 5.26 indicates that the appearance and distribution of domain boundaries are independent of the coverage. Due to identical courses for reflexes at 14%, 29%, 42%, 58%, 71% and 85%BZ, one can assume the existence of statistically distributed domain boundaries for the (2x7) superstructure.

Figure 5.26 b) shows normalized intensity and FWHM of a reflex appearing at 18%BZ and again the values of the reflex at 85%BZ. This diagram was created to compare and define whether the 85%BZ reflex belongs to a (2x7) structure or rather to the average groove-to-groove distance of nanowire bundles. Therefore, courses need to be compared with reflexes of both structures. The reflex at about 18%BZ can be associated with nanowire bundles [2].

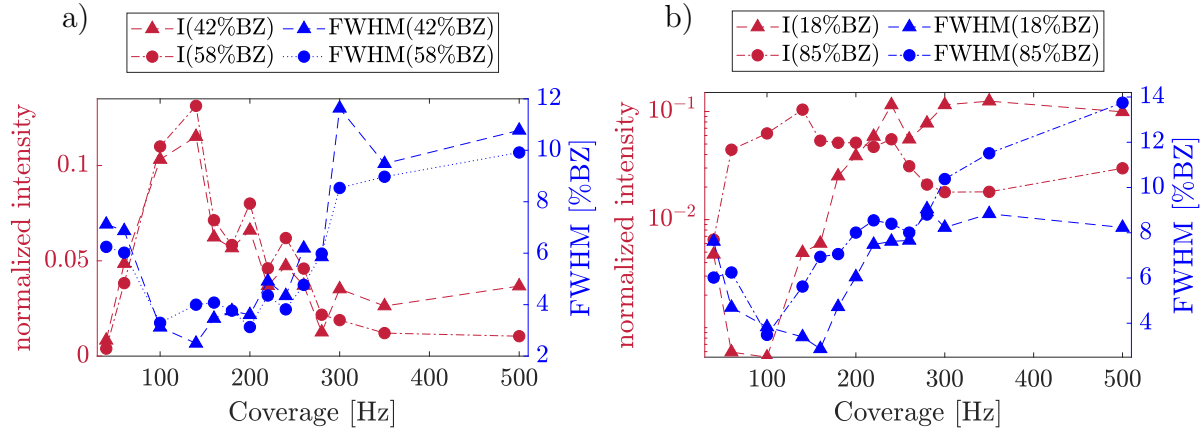The reflex at 18%BZ begins at low intensities increasing steadily. In general, values are

Figure 5.26: Coverage Series 3 - a) Normalized intensities and FWHM of reflexes at 42% and 58%BZ which are considered being part of the (2x7) structure. Both parameters show very similar behavior for both reflexes. b) displays normalized intensities and FWHM of reflexes at 18% and 85%BZ which are compared to determine whether they possibly indicate the average groove-to-groove distance of nanowire bundles on the surface.

very low at about 0.01 to 0.1. The FWHM shows a decrease up to 160Hz and a steady increase afterwards from 3%BZ to about 9%BZ.

Similar FWHM courses could indicate that both reflexes could belong to the same structure. At 100Hz, both FWHM have low values and increase for coverages higher than 140Hz, but they show a offset afterwards. The courses of normalized intensities differ which would indicate the contrary.

For low coverages, the normalized intensity of the reflex at 18%BZ is much lower than of the reflex at 85%BZ. It increases with the appearance of nanowires on the sample surface. For the area at about 85%BZ, only one fitting function was used to represent the measured values. Therefore the values show a superposition of both reflexes which has impact on higher FWHM of the 85%BZ reflex in comparison to the 18%BZ reflex.

Evaluation of nanowire bundles

Reflexes counted to nanowire bundle structures are expected to shift positions with increasing coverage when the average groove-to-groove distance changes. Therefore the varying positions of the reflexes at approximately 18% and 85%BZ are displayed in figure 5.27 (see chapter 3.4).

The reflex at 18%BZ (green) starts with an average groove-to-groove distance of nearly $5.6a_{Si(001)}$ at position 18%BZ and decreases to values of about $5a_{Si(001)}$ for 300Hz. For higher coverages, d increases again.

The other examined reflex at about 85%BZ starts at an average groove-to-groove distance d of about $6.5a_{Si(001)}$ which increases with fluctuations up to 220Hz and values of $8a_{Si(001)}$. For even higher coverages, $d(85\%BZ)$ decreases again to about $7a_{Si(001)}$. In average, $d(18\%BZ)$ shows a decreasing and $d(85\%BZ)$ an increasing linear slope throughout the coverage series. Due to the assumed superposition of the reflexes of the mean groove-to-
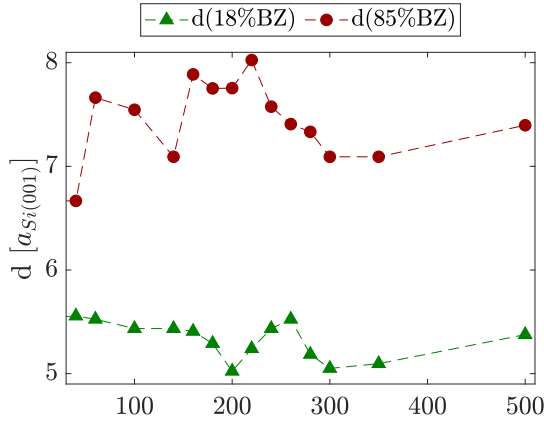
Figure 5.27: Coverage Series 3 - Average groove-to-groove distances resulting of the positions of reflexes at about 18% and 85%BZ. The resulting values are displayed in units of lattice constants of the substrate. For 18%BZ reflex, the groove-to-groove distances decrease with increasing coverage. In contrast, for 85%BZ they increase.

groove distance of nanowire bundles and the reflex corresponding to the (2x7) structure at about 85.7%BZ, this reflex can not be properly evaluated. Normalized intensity and FWHM courses do not fit either of them and the intensities are too low to distinguish between them. The decrease of the mean groove-to-groove distance resulting from the reflex at 18%BZ indicates that more nanowire bundles form in between the existing ones with increasing coverage.

Due to symmetric reasons, one would estimate that not only are there two very close reflexes at 14%BZ and 18%BZ, but also at 82%BZ and 86%BZ instead of one reflex at 85%BZ. Unfortunately the measured values do not give enough information for this. The assumed superposition of the two reflexes at 14%BZ and 18%BZ is a possible explanation why intensities and FWHM of both these reflexes do not match clearly with associated reflexes. The average groove-to-groove distance of about $8a_{Si(001)}$ equals a lateral scattering vector of about 87.5%BZ. The superposition of this reflex with the reflex at associated with the (2x7) structure at about 85.7%BZ ($\frac{6}{7}$BZ) could lead to incorrectly high values for the average groove-to-groove distance and therefore explain the increasing tendency.

Screenshots of the measured values and their fits are given in figure 5.28. In a) the two close reflexes at 14% and 18%BZ are shown with blue and yellow fitting functions. b) gives measurement values and fits for the range around 85%BZ. In contrast to the data points between 10%BZ and 25%BZ, the intensity course at about 85%BZ does not support the identification of two singular reflexes, even though this would be expected by symmetry.

Coverage series 3 is the only one not showing reflexes of a (2x4) reconstructed surface. Directly after the (2x1) structure decaying up to 100Hz, reflexes possibly referring to a (2x7) reconstruction appear.
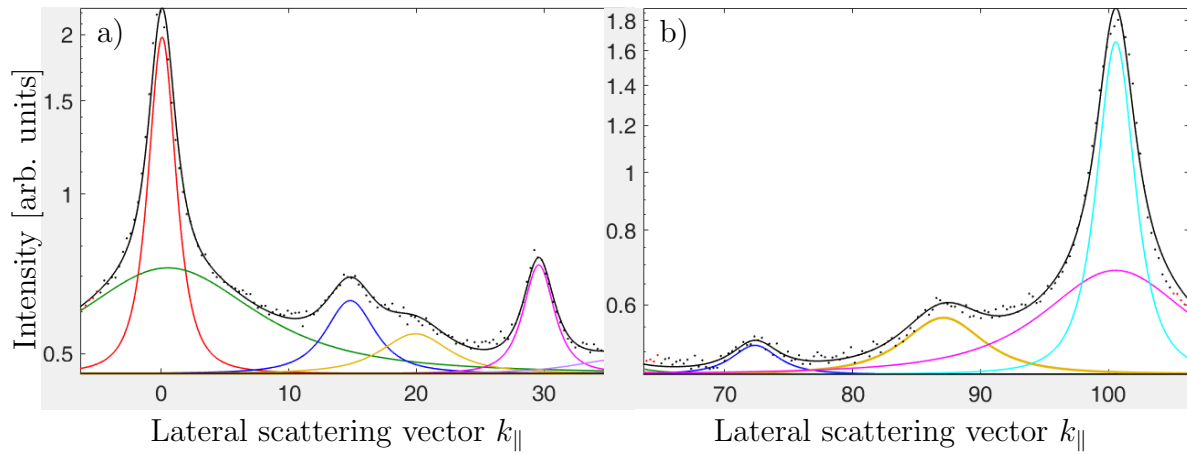
Figure 5.28: Coverage Series 3 - Fitting a) 14% and 18%BZ and b) 85%BZ, both measurements exemplary for a coverage of 200Hz to show that for reflex at 85%BZ, the measurement values do not indicate a division in two reflexes contrary to the reflexes at 14%BZ and 18%BZ exposing a distinct shoulder. A similar interpretation for both position ranges was expected due to symmetric reasons.

5.5 Studies on Terbium

To further evaluate the influence of Rare Earths, with terbium another RE element was examined. For both Gd and Tb, literature indicates the appearance of similar surface structures. Therefore for the next two coverage series, it was examined whether Tb grows more orderly. Based on former papers [34], the outcome was expected to show more intense and clearer structures on the surface and a consistent construction and deconstruction course of these. It was suspected that this could be RE dependent, and for the next two coverage series, another material was chosen. Due to experiments on terbium in the past [34], for the next two coverage series, terbium was selected as coverage material.

5.5.1 Coverage Series IV

In this coverage series, deposition was performed again at a sample temperature of 500°C and an evaporation power of about 43W for depositing Tb. The deposition duration range reaches from one minute to 6,5 minutes leading to coverages from 20Hz to 300Hz with a coverage step size of 20Hz throughout the whole series without measurements at 40Hz and 160Hz.

Figure 5.29 shows a 3D presentation of the linescans of coverage series 4. Normalized intensities are displayed on a logarithmic scale and shifted against each other for better visibility. For low coverages up to 20Hz, a (x2) periodicity is visible with reflexes at 50%BZ. With further increasing coverage, additional reflexes at 25% and 75%BZ appear indicating a (2x4) reconstructed surface. This structure continues up to about 280Hz, whereas at 180Hz another broad reflex at about 10%BZ appears and stays until the highest coverage. For 280Hz and higher, the (2x4) reconstruction decreases. No reflexes caused by a (2x7) reconstructed surface can be seen in this coverage series. For identifying and evaluating single reflexes, only the side of negative lateral scattering is taken into account in the following and the highest coverage of 400Hz is left out from further evaluation due to strong deviations. The intensity course of the lowest two coverages of 0Hz and 20Hz show weaker reflexes which was probably caused by an improper centering of the (00)reflex before the SPA-LEED measurement so that reflexes at ±50%BZ and ±100%BZ were not met correctly.

2D diffraction patterns

Figure 5.30 displays four exemplary measurements of coverage series 4 in 2D. 60Hz, 120Hz, 240Hz and 300Hz were chosen to demonstrate a development in surface structures. At 60Hz, reflexes originating of a clear (2x4) surface structure are visible without streaky intensity between reflexes. At 120Hz streaks on the main axes appear and get more intense for higher coverages up to 240Hz. At 300Hz, the reflexes are mostly vanished and replaced by a continuous intensity distribution with higher streak intensity at about (0,0), (0,1) and equivalents of symmetry on the main axes. Reflexes on the minor axes can be observed for all but 300Hz.

2D pictures of this coverage series indicate a (2x4) reconstructed surface for coverages of
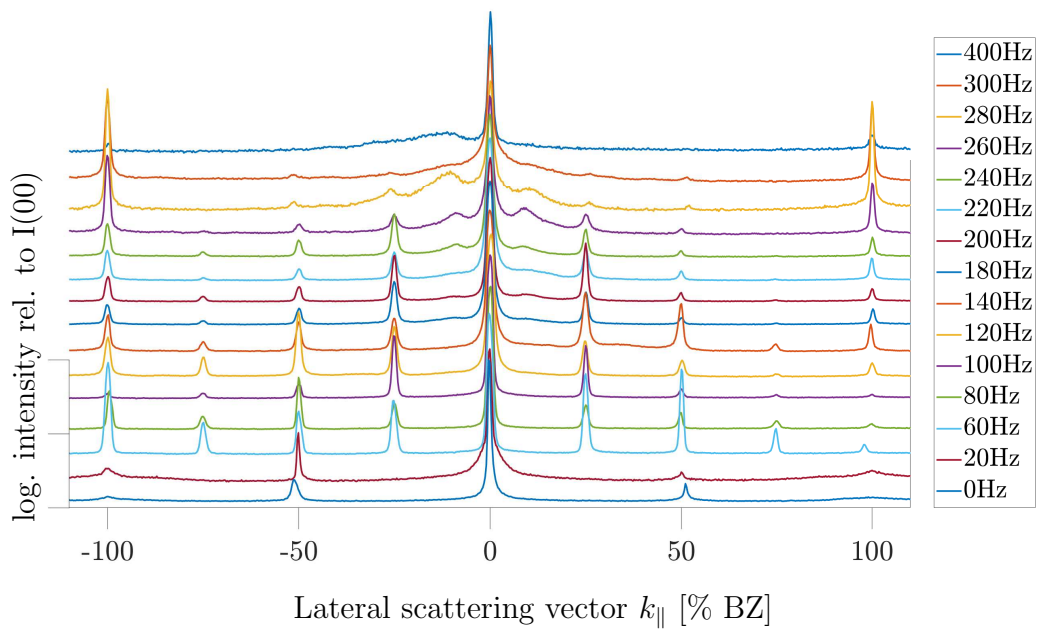
Figure 5.29: 3D presentation of linescans of coverage series 4. The linescans are shifted against each other for better visibility. The ordinate gives the normalized intensity in dependence of the lateral scattering vector in %BZ on the abscissa. The coverage step size is 20Hz from 0Hz to 300Hz without 40Hz and 160Hz. An additional measurement at 400Hz was performed.
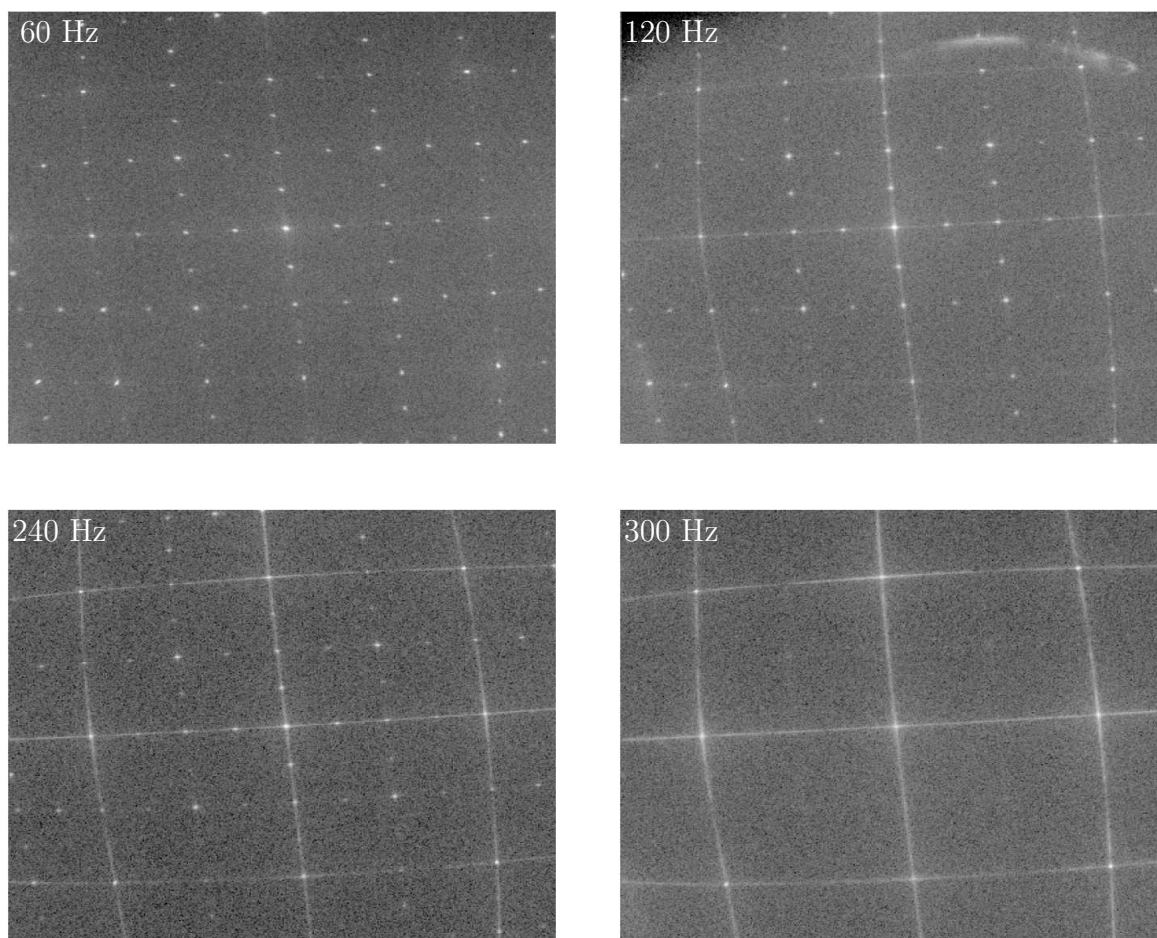
Figure 5.30: Exemplary 2D presentation of coverage series 4 with coverages of 60Hz, 120Hz, 240Hz and 300Hz. At 60Hz, a clear (2x4) pattern can be observed. With increasing coverage, streaky intensity on the main axes emerges, and for 300Hz, the reflexes caused by the (2x4) reconstruction are nearly vanished.

60Hz to 240Hz. At higher coverages, streaks on the main axes point to the existence of nanowires.

Analysis of linescans

FWHM and normalized intensity courses in dependence of the coverage are analyzed in the following, only the negative lateral scattering vector axis is evaluated for this coverage series. Figure 5.31 a) displays intensities and FWHM of reflexes at 0% cp and 50%BZ. As expected, the intensity of the central peak at 0%BZ is nearly constant at about 1. The intensity of the reflex at 50%BZ shows high fluctuations at about 0.2 until 120Hz and decreases afterwards to an intensity of 0.1 and lower. The FWHM of both reflexes is very similar, with a maximum followed by a steep fall at low coverages, slow and constant increase starting at 1%BZ for 80Hz to 2%BZ at 260Hz. These low values combined with high normalized intensities and a similar course of intensities and FWHM of reflexes at

0%BZ cp and 50%BZ indicate the existence of a (x2) structure covering nearly the whole surface in this coverage range. The increase in FWHM from 220Hz and higher and a parallel decrease in normalized intensity indicates a reduction of the (x2) periodicity and a replacement by nanowires.

Figure 5.31 b) gives the values for both functions used for fitting the 0%BZ reflex. The central peak is displayed in a) and b) for better comparison. Intensities as well as FWHM of 0%BZ b exhibit a slight increase from 0.02 to 0.1 respectively 20% to 38%BZ which can be interpreted as a slight roughening of the surface, with increasing coverage. The value stays almost at the same level for coverages up to 220Hz, normalized intensities are at about 0.1. Thereafter, FWHM and intensity increase.
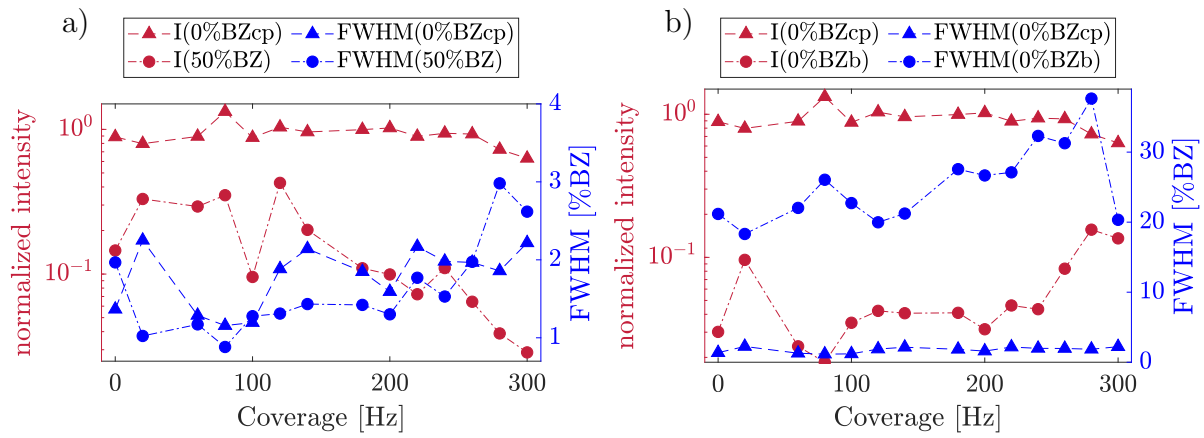
Figure 5.31: Coverage Series 4 - a) Normalized intensities and FWHM of 0%BZ cp and 50%BZ. Normalized intensities of 0%BZ cp stay constant, whereas for 50%BZ a decrease can be seen. FWHM start low and increase smoothly during the coverage series. b) gives normalized intensities and FWHM of 0% cp and broadening. Intensities and FWHM of the broadening reflex exhibit a slight increase.

Figure 5.32 a) displays values for reflexes at 25% and 75%BZ. They belong to a (2x4) reconstructed surface and normalized intensities show maximum values at about 0.1 in a range of 40Hz to 260Hz and decrease for lower and higher coverages. FWHM analogously have show minimal values at about 1%BZ in the same coverage range, surrounded by higher FWHM values. In general, normalized intensities in this diagram lie in the range of 0.01. This clearly shows that in the area of 40Hz to 260Hz, a stable (2x4) structure exists on the surface. Due to streaks on the main axes for 120Hz and above, the (2x4) structure probably coexists with nanowire on the surface for a wide coverage range.

For more precise evaluation of the (2x4) structure, the FWHM of associated reflexes at 25%, 50% and 75%BZ are displayed in figure 5.33. The course of all three FWHM are similar and at similar values. As one would expect, the reflex at 50%BZ exists already with a lower FWHM from the beginning of the coverage series caused by the (2x1) reconstruction of Si(001) surface. For the range of the (2x4) structure being most distinctive between 60Hz and 240Hz, FWHM values are at about the same level at 1% to 2%BZ. They increase for lower and higher coverages, implicating the vanishing of this structure. The similarity of the FWHM courses indicates again a statistical distribution of domain
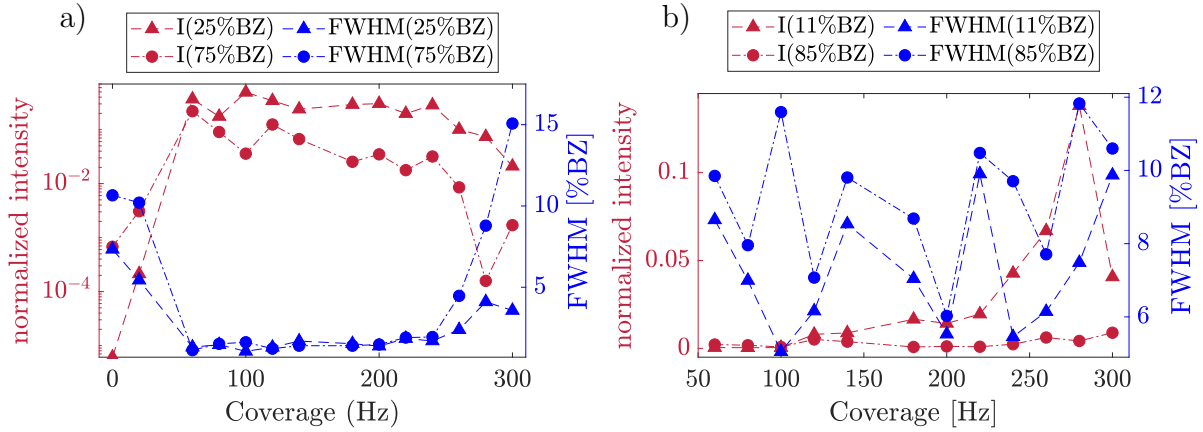
Figure 5.32: Coverage Series 4 - a) Normalized intensities and FWHM for reflexes at 25% and 75%BZ. They are considered to originate from a (2x4) reconstructed surface. In b), normalized intensities and FWHM of reflexes at 11% and 85%BZ are displayed which could be associated with bundling of nanowires or other structures on the surface.
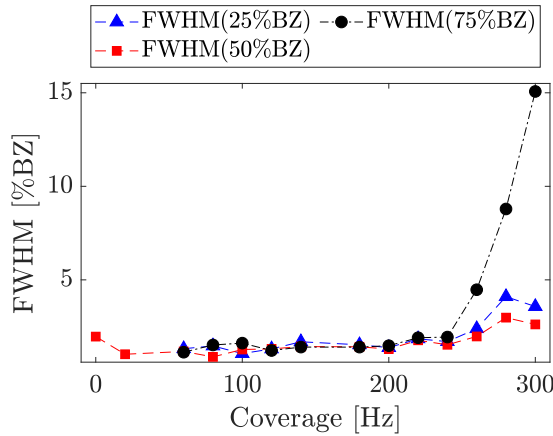

Figure 5.33: Coverage Series 4 - FWHM of 25%, 50% and 75%BZ reflexes. These reflexes belong to the (2x4) reconstruction on the sample surface, which is most distinctive between coverages of 60Hz and 240Hz. FWHM in this range take values of 1% to 2%BZ, increasing for lower and higher coverages.

boundaries on the surface. It can also be assumed that for 60Hz and above, the (2x1) reconstruction of the surface has vanished.

Figure 5.32 b) gives normalized intensities and FWHM of reflexes at 11% and 85%BZ. The reflex at 85%BZ has very low intensity, see exemplarily figure 5.34 b) for 120Hz. In figure 5.34 a), fitting for the reflex at about 10%BZ for 220Hz is shown.

In figure 5.32 b), normalized intensities lie at around 0.01 for both reflexes and show a linearly increasing trend. FWHM lie between 5% to 12%BZ with strong fluctuations. Normalized intensities of the 11%BZ reflex indicate a growing presence of the structure causing this reflex on the surface. The FWHM of 11%BZ fluctuates in a fixed range of about 6% to 12%BZ. This indicates that the domain size on the surface is not dependent on the coverage but rather of differences in sample preparation processes. The reflex at about 11%BZ appears together with a broadening of the 0%BZ reflex. The 11%BZ reflex could make a statement about to the average groove-to-groove distance of nanowire bundles on the surface, if that is assumed to be its cause.
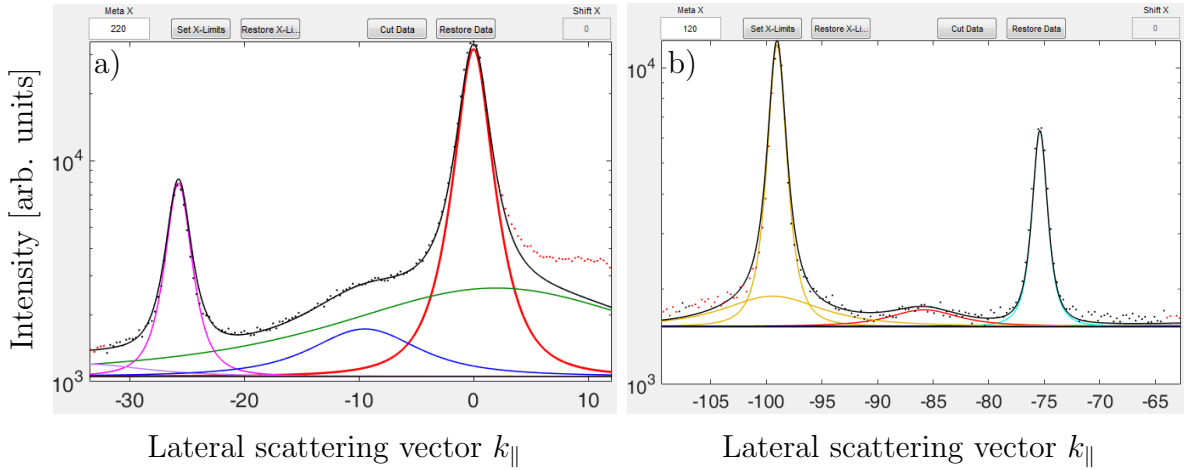
Figure 5.34: Coverage Series 4 - Fitting shown exemplarily for a) 11%BZ at 200Hz and b) 85%BZ at 120Hz. The coverages were chosen to show reflexes at a state of significant expression. In a), the 11%BZ reflex was fitted with the blue function, the rest is displayed for embedding. In b), 85%BZ measurement values were fitted with the red function, surrounding reflexes again shown for embedding the analyzed reflex. Both reflexes have very low intensities compared to their environment.

Figure 5.35 shows normalized intensities and FWHM for reflexes at lateral scattering vectors of 33% and 42%BZ. Normalized intensities of both reflexes only get visible in a closer evaluation of individual measurements, not in figure 5.29. Measurement values with the corresponding fit are displayed in figure 5.36. Both intensity courses show partly similar behavior, starting at high intensities for low coverages, decreasing to a local minimum at about 60Hz to 80Hz, increasing to a local maximum at about 120Hz to 140Hz. Afterwards, they show low intensities up to coverages of about 260Hz. At higher coverages, the values increase again. FWHM however have different courses: the one belonging to the reflex at 33%BZ stay at about the same level with a slow decrease and fluctuations of about ±3%BZ. FWHM of 42%BZ are remaining at a level of about 4-6%BZ for coverages of 100Hz to 260Hz, before and afterwards they have values up to 9%BZ. This could indicate the existence of a structure including the reflex at 42%BZ most pronounced between 100Hz and 260Hz, but still with low intensities. This differs from the course of reflexes at 11%BZ and 85%BZ, what lets assume that the reflexes belong to different structures. Intensity courses of 33%BZ and 42%BZ are similar which could indicate an affiliation to the same structure, but low intensity values make it hard to make statements out of these results.

The lateral scattering vector of about 42%BZ points to a (x7) structure, but no other correlating reflexes are visible in this coverage series. A reflex at 33%BZ could perhaps belong to the (2x3) substructure of a (2x7) reconstruction of the surface (see chapter 3.4). But to gain a linescan with only reflexes of a (x3) structure, it can not coexist with the (2x4) structure of the (2x7) reconstruction but would exist as a pure domain. Additionally, for a (2x3) reconstruction a (x2) periodicity would be visible here, which is not the case. So this explanation is very improbable. A pure (x3) reconstruction was examined at an additional measurement, the results are presented in figure 5.47. For a
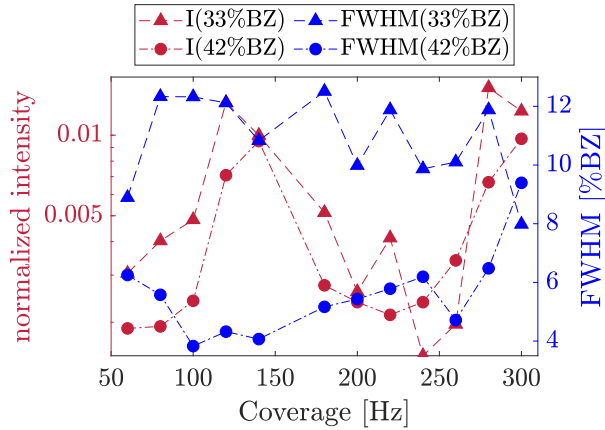
Figure 5.35: Coverage Series 4 - Normalized intensities and FWHM of reflexes at 33% and 42%BZ. Intensities show similar courses and values, whereas FWHM differ in values of about 11%BZ for 33%BZ and 5%BZ for 42%BZ. Both FWHM show rather constant behavior with fluctuations, with a slow linear decrease for 33%BZ and a slow increase for 42%BZ reflex.
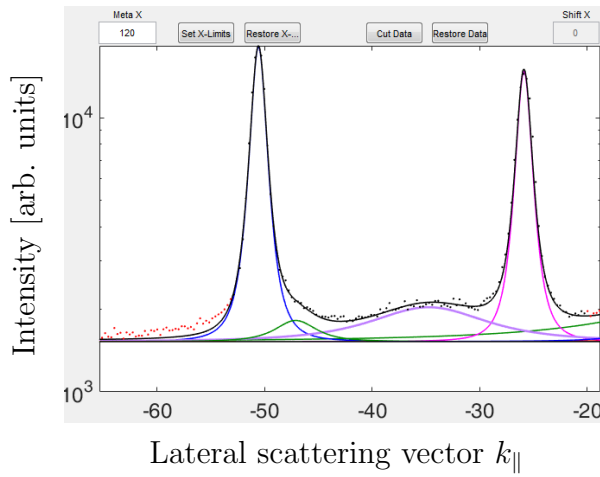

Figure 5.36: Coverage Series 4 - Measurement values in fitting program from 10% to 60%BZ. Reflexes at 33% and 42%BZ (here shifted up to about 47%BZ) lie between more intense reflexes at 25% and 50%BZ.

good (x3) structure on the surface, in this case for symmetrical reasons, another reflex at 66%BZ should be visible too, which can not be confirmed by this measurement.

Evaluation of nanowire bundles

In figure 5.37, the average groove-to-groove distance d resulting of the shift in position of the reflex at about 11%BZ is displayed. In general for this reflex, values fluctuate around an average groove-to-groove distance of about $9a_{Si(001)}$. For coverages from 120Hz to about 220Hz, d increases from about $8.5a_{Si(001)}$ to $10.5a_{Si(001)}$ and decreases afterwards again to about $8a_{Si(001)}$ for 300Hz. Positions of reflexes at 33%BZ and 85%BZ are not evaluated due to their very low intensities.

Other research [2, 14, 34] has shown that the nanowire bundles appear (here for coverages of 120Hz and higher). The nanowires are indicated by streaks on the main axes, coexisting with reflexes of a (2x4) reconstructed surface. The increase in average groove-to-groove distance between nanowire bundles d can possibly be explained by the assumption that in the beginning, only small parts of the surface are covered with nanowire bundle areas. With increasing RE material on the surface, more areas with a coverage of nanowire bundles are created on the surface, which would lead to an increase in the total average groove-to-groove distance of the whole surface. The decrease in d for 220Hz and higher leads to the presumption that the more rare earth material is deposited on the surface,

Figure 5.37: Coverage Series 4 - Coverage dependency of average groove-to-groove distance d of nanowire bundles resulting from the position of the reflex at about 11%BZ. The course shows a parabolic behavior with a maximum at about 240Hz.
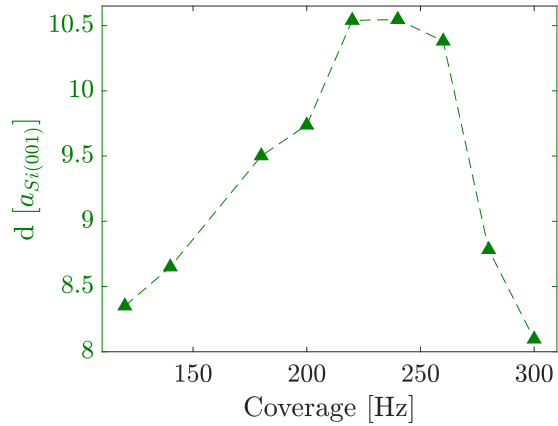
the more nanowire bundles grow on the surface, and the smaller the distances in between are.

In this coverage series, reflexes correlating with a (2x1) reconstructed surface are visible for up to 20Hz, afterwards additional reflexes indicating a (2x4) reconstruction can be seen for up to 280Hz by analyzing intensity and FWHM courses. For 120Hz and above, additional streaks on the main axes point to the existence of nanowires. Additional reflexes are appearing at 11%, 85%, 33% and 42%BZ, the latter could solely possibly belong to a (2x7) structure. The reflex at 33%BZ could belong to a (2x3) substructure of a (2x7) structure, whereas the reflexes at 11%BZ and 85%BZ can be associated to nanowire bundling but no clear tendency can be identified for their average groove-to-groove distance. No consistent growth of reflexes of nanowire bundles can be proven by this coverage series, as well as no (2x7) structure growth is visible in the measurement results.

5.5.2 Coverage Series V

This last coverage series was performed again with Tb as RE material, but with a higher substrate temperature of 600°C during deposition. The used evaporation power here is again 43W leading to the duration of the deposition process lying in a range of 30 seconds to 7 minutes. In this coverage series, the coverage steps are 20Hz up to 300Hz with an additional measurement at 350Hz. The measurement at a coverage of 280Hz was left out due to strong deviation from the rest with unknown origin.
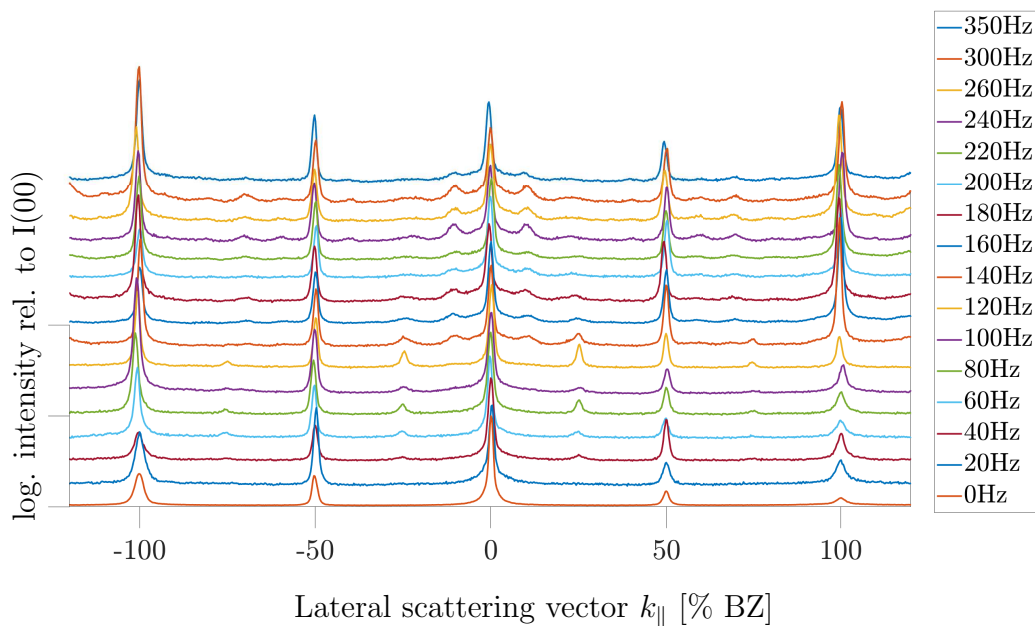

Figure 5.38: 3D presentation of linescans of coverage series 5. Coverage steps are 20Hz from 0Hz to 260Hz with additional measurements at 300Hz and 450Hz. The diagram displays the normalized intensity on the ordinate in dependence of the lateral scattering vector on the abscissa. The linescans are shifted against each other for better visibility.

Figure 5.38 displays the linescans of this coverage series in a 3D plot, showing the normalized intensity in dependence of and the lateral scattering vector. The intensity is again presented on a logarithmic scale. The diagram gives coverages from 0Hz to 260Hz in steps of 20Hz and additional measurements at 300Hz and 350Hz. For low coverages up to 40Hz, one can see reflexes at 50%BZ indicating a (2x1) reconstructed surface. With increasing coverage, additional reflexes at $\pm 25\%$ and $\pm 75\%$BZ correlating with a (2x4) structure appear up to 140Hz. At 140Hz, other reflexes besides them begin to appear. They stay visible up to 350Hz at positions of 11%, 33%, 42%, 58%, 68% and 82%BZ. The possible underlying structure is examined in the following.

2D diffraction patterns

Figure 5.39 exemplarily gives 2D diffraction patterns of the coverages 80Hz, 140Hz and 240Hz.

At 80Hz, clear reflexes correlating with a (2x4) reconstructed surface can be identified. On the main axes and the minor axes, reflexes at $(0,\frac{1}{2})$ and equivalents of symmetry and exist. At 140Hz, the main axes get more streaky but still show very weak reflexes belonging to a (2x4) structure which are marked yellow. The streakiness on the main axes remains for 240Hz, whereas intensity besides the main axes vanishes, but the diffraction pattern does not change significantly for coverages higher than 140Hz. At high coverages, reflexes caused by a (2x1) reconstruction remain, probably existing on the surface of nanowires (see chapter 3.4).
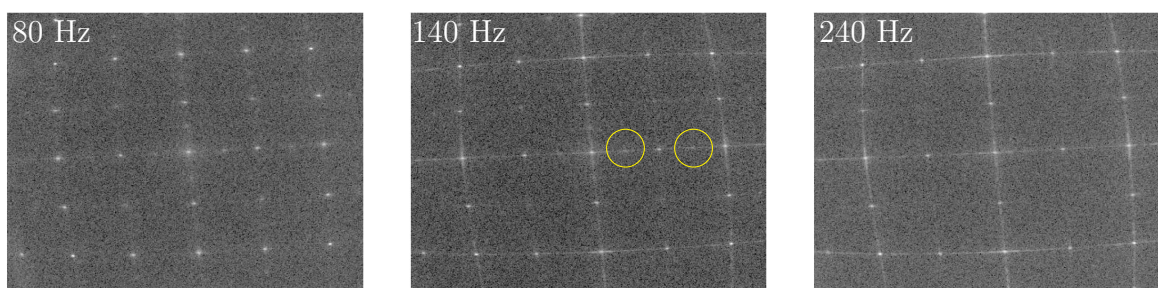
Figure 5.39: Exemplary 2D diffraction patterns of coverages of 80Hz, 140Hz and 240Hz of coverage series 5. For low coverages, reflexes correlating with a (2x4) reconstruction are visible. Intensity on minor axes vanishes with increasing coverage and on the main axes, streaks are emerging. Some weak reflexes at $(\frac{1}{4},0)$ and $(\frac{3}{4},0)$ are marked yellow. With increasing coverage above 140Hz, the diffraction pattern does not change significantly.

Analysis of linescans

Normalized intensity and FWHM courses of all identified reflexes are displayed in the following subchapter. They are grouped by the surface structures they probably belong to.

Figure 5.40 a) gives the measurement results for reflexes at 0% cp and 50%BZ. Normalized intensity values for 0% cp are relatively high as expected - about 0.8. It is constant with a slow linear decrease. The normalized intensity of the 50%BZ reflex starts low for low coverages and jumps to a level of about 0.6 between 100Hz and 140Hz. After 140Hz, it stays at about this level until highest coverages. FWHM start at high values of about 2.2%BZ, which is very low compared to other reflexes. Values sink a little to about 1.6%BZ with a slow linearly increasing tendency. In general, normalized intensities and FWHM of these reflexes indicate a clear and intense (2x1) reconstructed surface Si(001) surface for lowest coverages. The jump in FWHM and intensity values could indicate that for higher coverages, the structure causing the 50%BZ reflex changes.

Figure 5.40 b) shows both functions used for fitting the 0%BZ reflex, central peak and broadening. The intensity and FWHM of the central peak are nearly constant in this axis cutout. Courses for the 0%BZ broadening function show mainly constant behavior with a slow increase in intensity and decrease in FWHM. Similar behavior of both 0%BZ functions indicate again, that the roughness of the surface does not change throughout the coverage series.
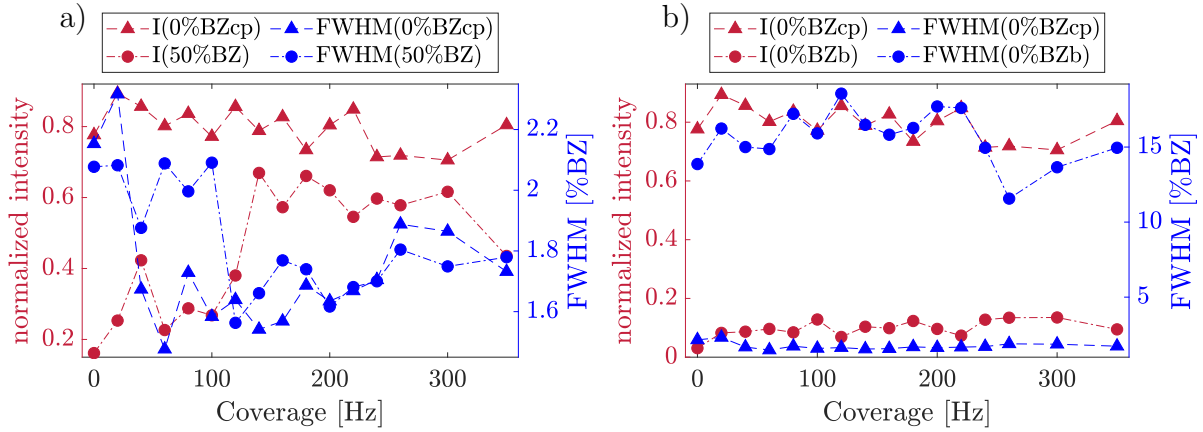
Figure 5.40: Coverage series 5 - a) Normalized intensities and FWHM of 0%BZ central peak and 50%BZ. The normalized intensity of 0%BZ cp reflex stays nearly constant with a slow decrease, whereas the reflex at 50%BZ starts at low intensities and jumps to a plateau at 140Hz. FWHM of 0%BZ cp is similar, only dropping to lower values already at 40Hz. b) shows normalized intensities and FWHM of the 0%BZ central peak and broadening. The intensities and FWHM of 0%BZ b are nearly constant.

Figure 5.41 a) displays fitting results for reflexes correlating with a (2x4) structure at 25% and 75%BZ. The normalized intensity courses for 25% and 75%BZ show a similar behavior. Normalized intensities start low at 0.02 respectively 0.05, increase to 0.3 at about 120Hz and decrease afterwards to about 0.001 for 75%BZ and 0.01 for 25%BZ reflexes. The course for 75%BZ shows a stronger decrease after 140Hz than the 25%BZ reflex. FWHM courses are similar too. They start at about 14%BZ for low coverages and sink in an exponential manner down to a minimum of 2%BZ at about 120Hz. With further increasing coverage, an increase can be noted up to 7% to 9%BZ at 300Hz. Normalized intensities and FWHM of these two reflexes allow a consistent conclusion: the (2x4) structure builds up from low coverages to about 120Hz and replaces the (2x1) structure, where it takes up the highest percentage and the longest-range areas of the surface. Reflexes are most distinctive at this coverage. Increasing further, the structure starts to disappear and on parts of the surface and different structures appear.

Figure 5.41 b) gives experimental results of 11% and 33%BZ reflexes which could eventually be counted to nanowire bundles and (x3) structures. Normalized intensities start at low values of about 0.002 and increase with decreasing gradient, whereas 33%BZ stays about constant at lower values than 11%BZ. FWHM of 11%BZ start at about 10%BZ and sink approximately linearly down to 3%BZ with a stronger decrease between 120Hz and 140Hz. FWHM of 33%BZ starts at about 7%BZ and sinks slowly down to values of 3%BZ too for highest coverages. The structure belonging to the reflex at 11%BZ is slowly building up until coverages of about 120Hz and has the highest average long-distance characteristics from 140HZ to 350Hz. The reflex at 33%BZ builds up earlier at about 40Hz and stays at that level for the rest of the coverage series, FWHM indicating a most characteristic representation at 300Hz.

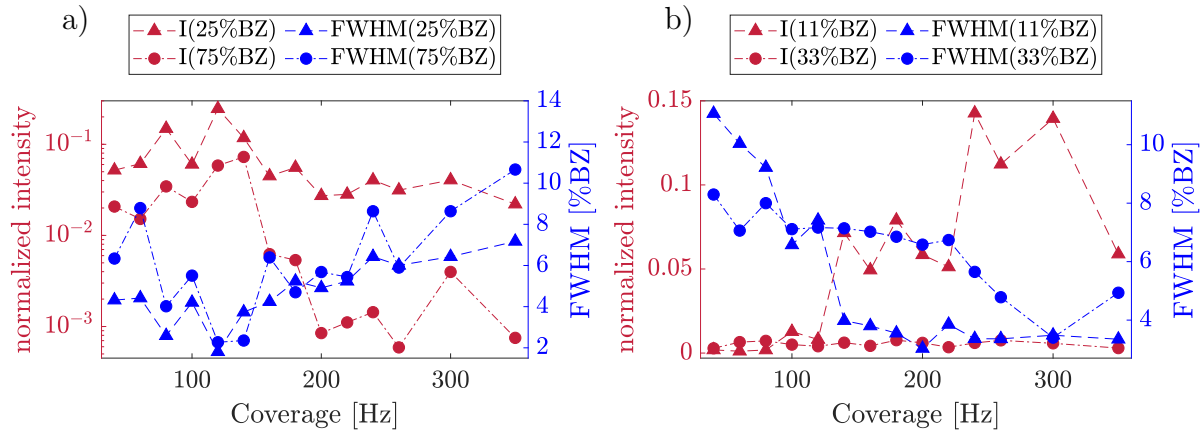The normalized intensity and FWHM courses of further reflexes at 42%, 58%, 68% and

Figure 5.41: Coverage Series 5 - a) Normalized intensities and FWHM of reflexes at 25% and 75%BZ. Courses of both FWHM and both normalized intensities are very similar. FWHM show a minimum, in the same range intensities have a maximum and slowly decrease afterwards. b) Normalized intensities and FWHM of reflexes at 11% and 33%BZ. Intensities both start low, with 33%BZ staying constant and 11%BZ increasing. FWHM decrease constantly for both reflexes.

82%BZ are shown in figure 5.42. These are displayed together to check whether they belong to one surface structure. In a), the normalized intensity of 42%BZ starts at values of about 0.002 and increases linearly until 80Hz, then drops down to 0.001 at 140Hz and increases again with higher coverages to values of 0.02. The other intensity course of 58%BZ reflex shows a slow and steady increase from the same low values for low coverages up to 0.05 for coverages of about 300Hz. FWHM show similar courses for both reflexes, starting at about 11%BZ decreasing to 3%BZ for 42%BZ and 6%BZ for 58%BZ at 300Hz.

Reflexes at 68% and 82%BZ show very similar courses in FWHM and normalized intensities displayed in figure 5.42 b). Normalized intensities start at very low values of about 0.003 and increase with one jump in intensity between 120Hz and 140Hz. For higher coverages, the intensities are nearly constant, values for 68%BZ are higher than for 82%BZ. FWHM start at a high level of 8% to 11%BZ and sink down to a range of 3% to 4%BZ at a coverage of 300Hz. 68%BZ values are similar up to 120Hz and afterwards lie above those of 82%BZ for higher coverages. From this diagram follows, that this structure gets more noticeable the higher the coverage and has therefore the highest average domain size for highest coverages. Reflexes get sharper and more intense, even though the intensity is still very low. For the highest coverage of 350Hz, FWHM increase and normalized intensities decrease indicating that this structure disappears with further increasing coverage.

Figure 5.43 gives again the FWHM measurement results for (2x4) assigned reflexes, this time displayed together in one diagram. FWHM courses of the reflexes at 25% and 75%BZ show very similar behavior, whereas the FWHM values of 50%BZ are much lower during the whole coverage series. The 50%BZ reflex is pronounced for all examined coverages. For low coverages, the reflex originates from the (2x1) reconstruction of the Si(001) substrate. With increasing coverage, it results from the (2x4) reconstructed surface, which is probably
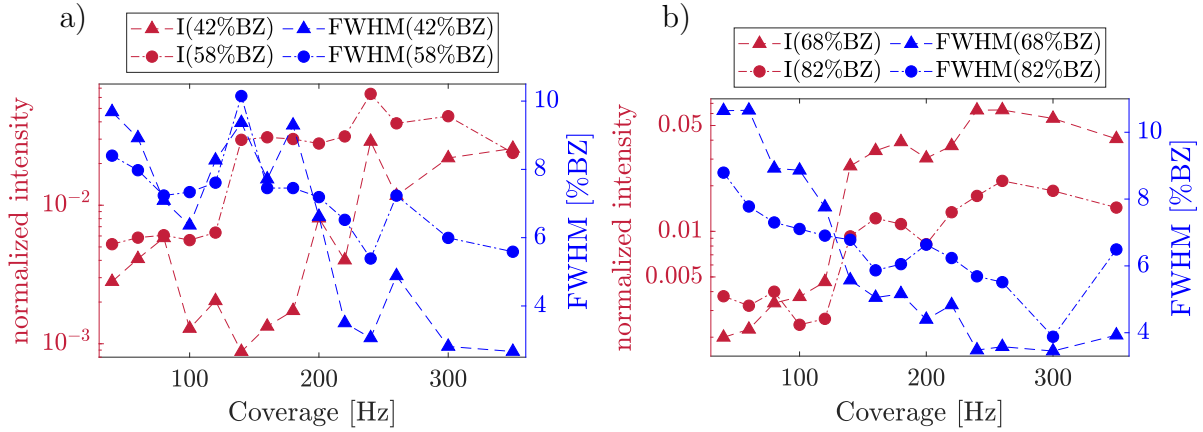
Figure 5.42: Coverage series 5 - a) Normalized intensities and FWHM of 42% and 58%BZ. FWHM both show about linearly decreasing values, whereas the normalized intensities increase, 42%BZ having a minimum at about 140Hz. In b) courses of normalized intensities and FWHM of reflexes at 68% and 82%BZ are very similar with behavior that can be seen as linearly too.

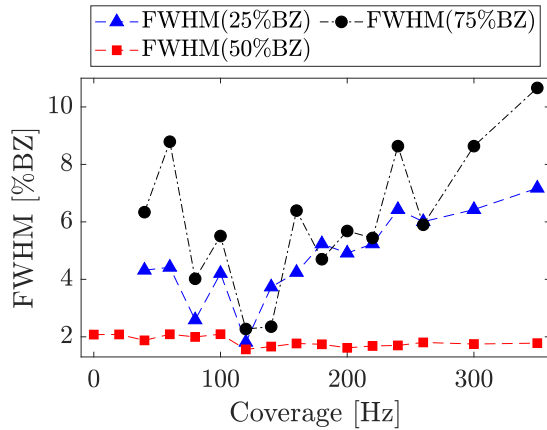replaced by nanowires which also can create a (2x1) reconstruction on their surface, as shown in [34].

Figure 5.43: Coverage Series 5 - FWHM of reflexes at 25%, 50% and 75%BZ. FWHM for the reflex at 50%BZ are constantly low. FWHM of reflexes at 25% and 75%BZ decrease from 40 to 120Hz where they form a minimum and increase for higher coverages. All three reflexes can be counted to (2x4) structure on the surface, whereas the reflex at 50%BZ also exists due to a (2x1) reconstructed substrate surface up to 40Hz. For higher coverages, the reflex probably results from a (2x1) reconstruction existing on nanowire structures.

FWHM and normalized intensities courses of reflexes at 11%, 58%, 68% and 82%BZ are very similar, as well as FWHM courses of reflexes at 33% and 42%BZ. These last two reflexes differ only in normalized intensity. This indicates that reflexes at about 11%, 58%, 68% and 82%BZ originate from the same surface structure, whereas reflexes at 33% and 42%BZ result from other unknown structures overlaying with it. In general, normalized intensities of these six reflexes are low in comparison to the reflex at 50%BZ. Measurement values for a coverage of 240Hz with fitting functions are shown in figure 5.44.

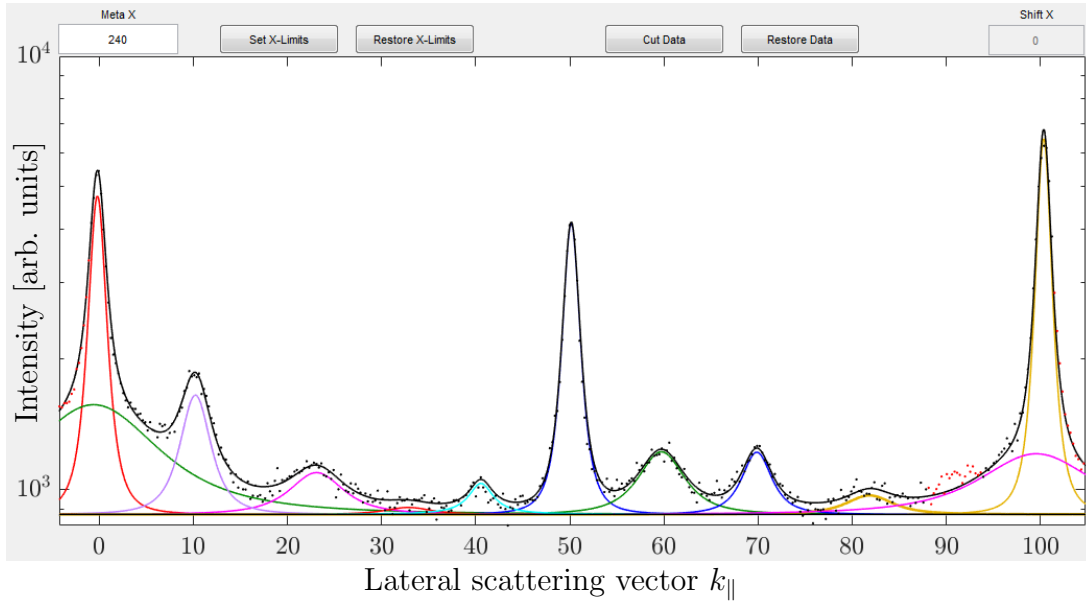Possibly, the reflex at 11%BZ does not belong to the same structure as other reflexes but

Figure 5.44: Coverage Series 5 - Fitting in the range of 0% to 100%BZ for a coverage of 240Hz. Measurement values at about 90%BZ are left out because no consistent growth of a reflex can be seen at this lateral scattering vector for surrounding coverages.

results from the nanowire bundling on the surface. Therefore, in figure 5.45 the average groove-to-groove distance d is displayed in dependence of the coverage in units of the lattice constant $a_{Si(001)} = 3.84$Å. This diagram shows that d starts at about $8a_{Si(001)}$ at 120Hz, jumps to $9a_{Si(001)}$ at 140Hz and increases slowly to about $10.7a_{Si(001)}$ for 350Hz. One explanation for the increase in d could be that with increasing coverage, several bundles merge with each other, leading to broader bundles with a higher average groove-to-groove distance between the bundles. Another possible explanation could be that the more Tb deposits on the surface, the more areas with nanowire bundles reconstruct on the surface, leading to an increase in the total mean groove-to-groove distance on the whole surface. The reflex at about 82%BZ is not further evaluated due to low normalized intensities.
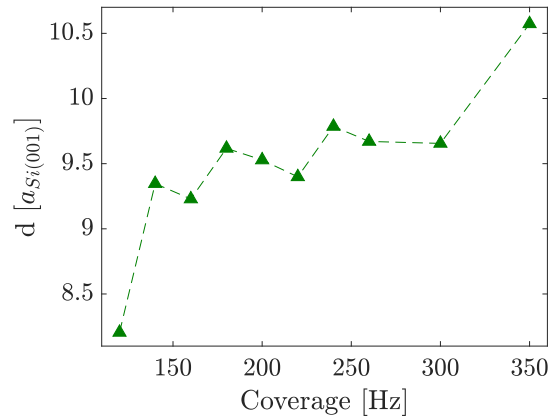

Figure 5.45: Coverage series 5 - Coverage dependent average groove-to-groove-distance d for the reflex at about 11%BZ possibly resulting from nanowire bundles on the surface. $d(11\%BZ)$ has a slowly increasing tendency.

All in all, in this coverage series, reflexes appearing at 25%, 50% and 75%BZ can be

identified belonging to (2x4) structures, additional reflexes can not easily be assigned to another structure. Their lateral scattering vectors are about 11%, 33%, 42%, 58%, 68% and 82%BZ and indicate most probably some kind of (x10) structure, when (2x4) reflexes are assumed to be superimposed. The assumed (x10) structure develops slowly for higher coverages of 140Hz and above. A reflex at about 90%BZ is missing following this theory, and some are shifted out of expected position for a (x10) structure, for example at 25%BZ. This indicates a nanowire bundle structure with no integer periodicity (no exact (x9) or (x10) structure) but something in between. The reflexes of a (x2) structure at high coverages point to the existence of nanowire bundles with a (2x1) reconstruction on their surface (see chapter 3.4).

A possible explanation for a (x10) structure on the surface could be an configuration where a (2x4) structure is surrounded with a (2x3) structure from two sides, which indicates a (x10) structure in the diffraction pattern. Though, this scenario has not yet appeared in research as far as known at this point.

5.5.3 X-ray photo electron spectroscopy (XPS)

To determine whether the deviations of the SPA-LEED results from the expected behavior (see chapter 5.7) is caused by inadvertent adsorbates on the sample or other factors, X-ray photo electron spectroscopy (XPS) measurements (see chapter 2.4) were performed.

For the XPS measurements, the sample had to be exposed to ambient conditions for transportation to the XPS system. Consequently, the XPS measurements might feature additional adsorbates on the sample surface than being present during SPA-LEED examination. Figure 5.46 shows a representing survey XP spectrum for a sample with a Tb coverage of 350Hz from coverage series 5. The intensity values were averaged over three measurements at different areas on the sample surface. The recorded spectrum was calibrated according to the C1s peak at 284.5eV.
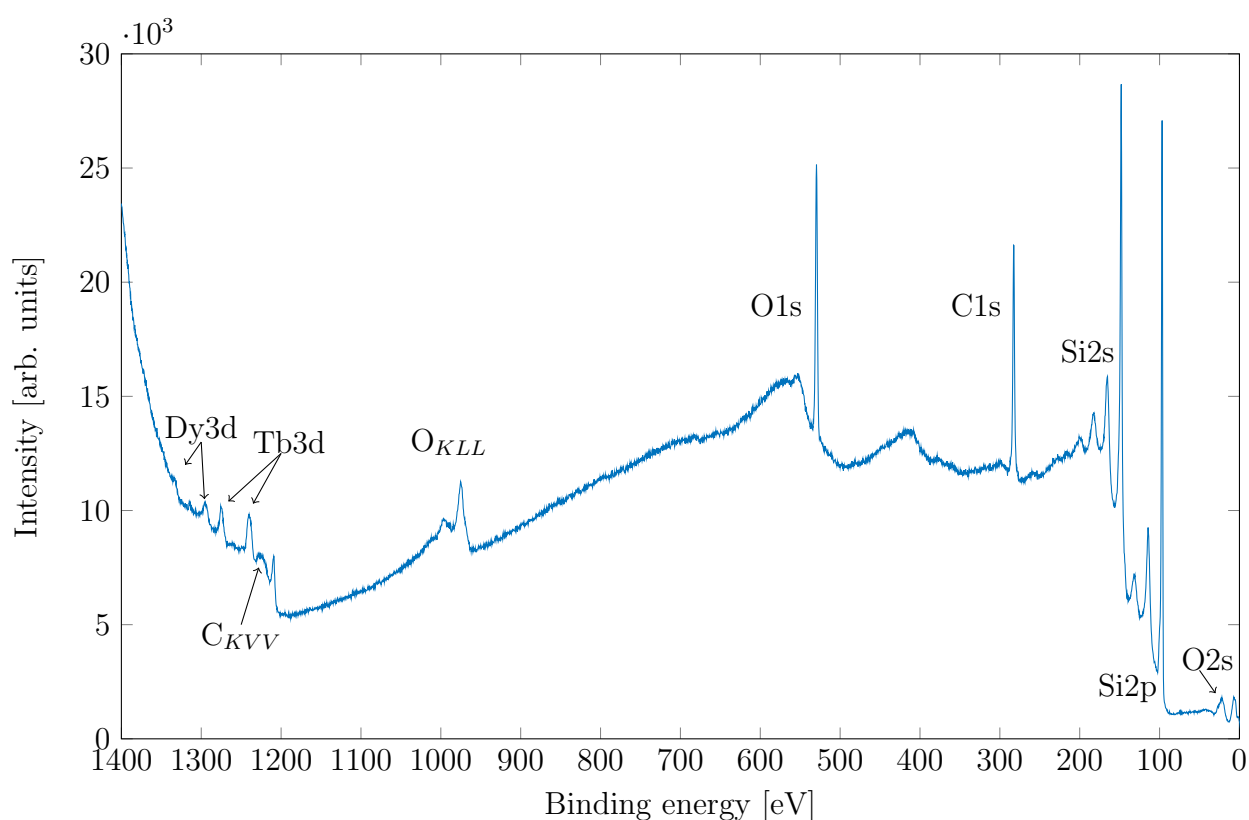

Figure 5.46: XP survey spectrum recorded for the last sample of coverage series 5 with a Tb coverage of 350Hz. The abscissa displays the binding energy, whereas the ordinate shows the correlating intensities. The different peaks in the spectrum are labeled according to their originating orbitals.

The spectrum has been analyzed qualitatively by comparing the binding energies of the different photoelectron peaks with literature values of different elements and their orbitals [51]. As a result, photoelectrons from C, O, Si, Tb and Dy could be identified. The different orbitals of each element are labeled in the spectrum above.

The spectrum shows distinct Si2p and Si2s photoelectron peaks at about 100eV and 150eV, respectively, originating from the used Si substrate itself. The Si2p and Si2s pho-

toelectron peaks are each accompanied by two additional peaks, which might be associated with plasmon loss satellites [52].

Furthermore, core-level photoelectron peaks of C1s at 284.5eV and O1s at 531eV as well as Auger peaks of C at 1223eV and O at 978eV are visible. The presence of both C and O in the spectrum can most likely be related to the fact that the sample was exposed to air during transport to the XPS analysis system, which resulted in the adsorption of C and O on the sample surface. However, the C1s peaks shows relatively high intensity. This could indicate a not yet discovered contamination of the UHV chamber or more probably of the evaporator used in these experiments. Additionally, it is possible that a contamination with C took place during manual transfer of the sample from the SPA-LEED chamber to the XPS measurement chamber.

The peaks at binding energies of 1242eV and 1277eV probably result from Tb3d photoelectrons due to the Tb coverage.

Most surprising and not expected to observe in the spectrum, are the photoelectron peaks at about 1296eV and 1333eV, which might be attributed to photoelectrons from Dy3d. Dy was used as rare earth element for other measurements in the same evaporator before, therefore traces can still exist and might have adsorbed on the sample surface.

A peak at a binding energy of 1211.2eV can not be accounted to a specific element. Nearby, literature values of Gd3d at 1218eV and Ge2p at 1217eV could indicate their existence with a bigger energy error range, but due to spin-orbit splitting, these peaks would only occur in pairs. The correlating additional peaks at 1186eV resp. 1248eV for Gd3d and Ge2p can not be identified in this spectrum.

The XPS measurement does not provide valid indications for the deviating SPA-LEED results. Although the increased amount of C on the sample could point to a contamination of UHV chamber or evaporator, it can also be explained by the transfer of the sample in ambient conditions. The existence of Dy is surprising but it can be assumed that Dy atoms on the sample would not induce the observed deviation.

5.6 Additional measurements - flux variation

The used evaporation rate is strongly dependent on the evaporator and the distances between sample and crucible. Therefore some additional measurements were performed with Gd where the flux was varied by varying the evaporation power from the crucible from 31mA to 38mA with a value of 35mA in between.
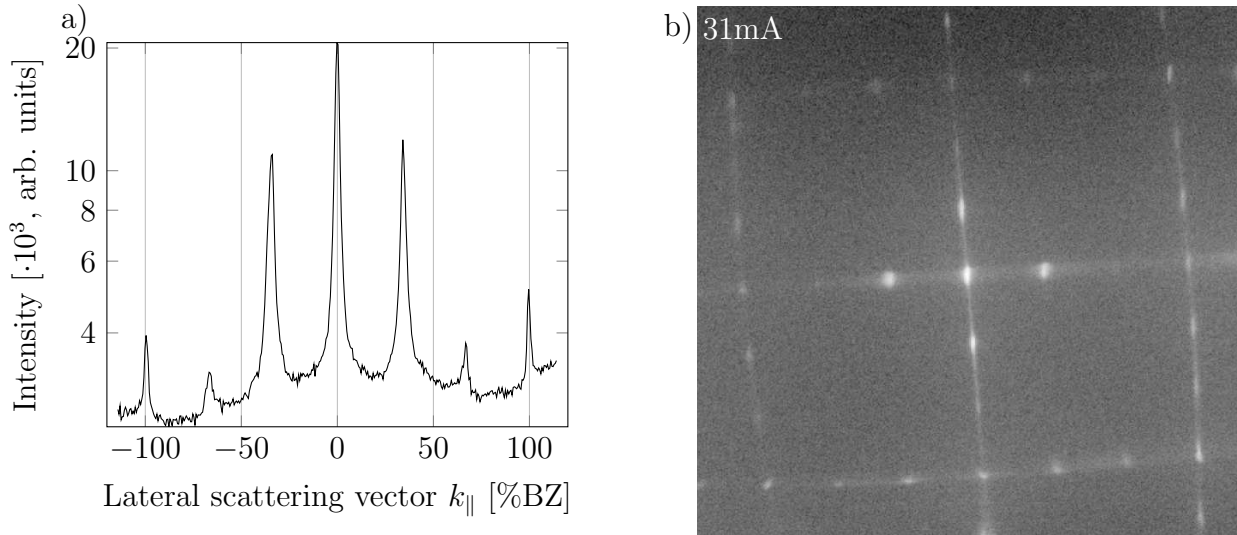

Figure 5.47: a) Linescan and b) 2D scan for a coverage of 160Hz, an evaporation power of 31mA and a substrate temperature of 550°C during deposition. The linescan was taken along the same axis as marked in figure 5.2. The 1D and 2D scans show a (x3) periodicity with reflexes at 33% and 67%BZ on both axes. The used electron energy is 130eV.

Figure 5.47 shows the first measurement at an evaporation power of 31mA. The 2D diffraction pattern indicates a (x3) superstructure. The correlating linescan confirms this assumption by showing reflexes of a (x3) periodicity at about 33% and 67%BZ.

Figure 5.48 shows a sample with a coverage of 80Hz and the same scan axis as in figure 5.2. The intensity of the 0%BZ reflex in a) is comparable to those in figure 5.47. Additionally, peaks at about 20%, 50% and 80%BZ can be identified in this intensity profile. The 2D diffraction pattern in b) shows some reflexes which could possibly be assumed to belong to a (2x4) superstructure (yellow) and a (x3) superstructure (blue). The streaks on the main axes indicate the existence of nanowire bundles, which could form a (2x1) reconstruction on the surface leading to reflexes at 50%BZ. Reflexes at 20% and 80%BZ could be caused by the average groove-to-groove distance of nanowire bundles. The (x3) structure can possibly belong to the (2x3) substructure of the (2x7) superstructure (see chapter 3.4). The quality of reflexes in the diffraction pattern is too low to allow further statements about the existence of structures on this surface.

The third measurement concerning the variable evaporation power was done at 38mA, results are shown in figure 5.49. The linescan in a) develops reflexes at 50%BZ as well as at about 33% and 67%BZ. The 50%BZ peak indicates the existence of a (2x1) superstructure on nanowires which cause streaky intensity on the main axes. Reflexes at 33% and 67%BZ could be the result of the (2x3) substructure which is part of the (2x7) superstructure (see
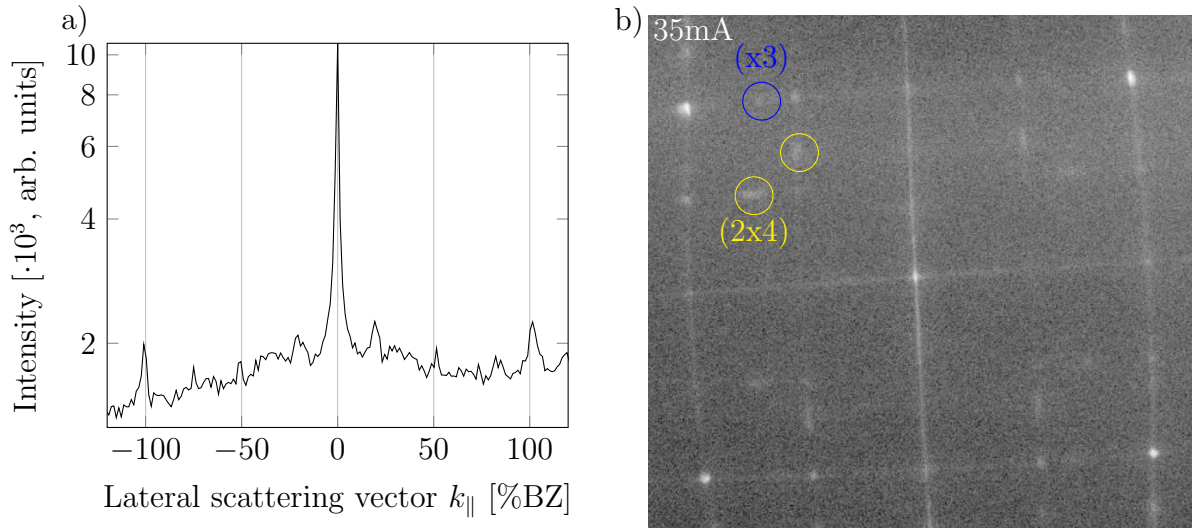
Figure 5.48: a) Linescan of a coverage of 80Hz with an evaporation power of 35mA and an electron energy of 130eV. The scan axis is again the same as in figure 5.2. Peaks are visible at about 20%, 50%BZ and 80%BZ. Intensities are low relatively to the reflex at 0%BZ. In b), the corresponding 2D diffraction pattern is shown. Reflexes possibly indicating a (2x4) superstructure (yellow) or a (x3) structure (blue) are marked. Streaks on the main axes point to the existence of nanowires on the surface.

chapter 3.4), but no reflexes correlating with a (2x7) reconstruction are visible. The 2D diffraction pattern in b) shows a low contrast and only some reflexes at 33% and 67%BZ can be identified.

These additional measurements were performed with differing evaporation powers and coverages which does not allow a direct comparison but show a (x3) periodicity for 31mA, 38mA and possibly at 35mA. The coverages with an evaporation power of 35mA and 38mA differ a lot, so that possibly the indistinct results have their origin in the amount of deposited material on the substrate, not in the evaporation power. These three measurements were not taken in a row and are displayed to show that (x3) periodicity in diffraction patterns can be detected at SPA-LEED measurements of Gd-induced superstructures. As long as the surface structures are in energetic balance, the evaporation power and thereby the duration of deposition should have no influence on the surface structures. A longer deposition duration could lead to more trace gas adsorbing on the surface, but the pressure range during the process lies in a range of about 10^{-9}mbar indicating low probability for that.
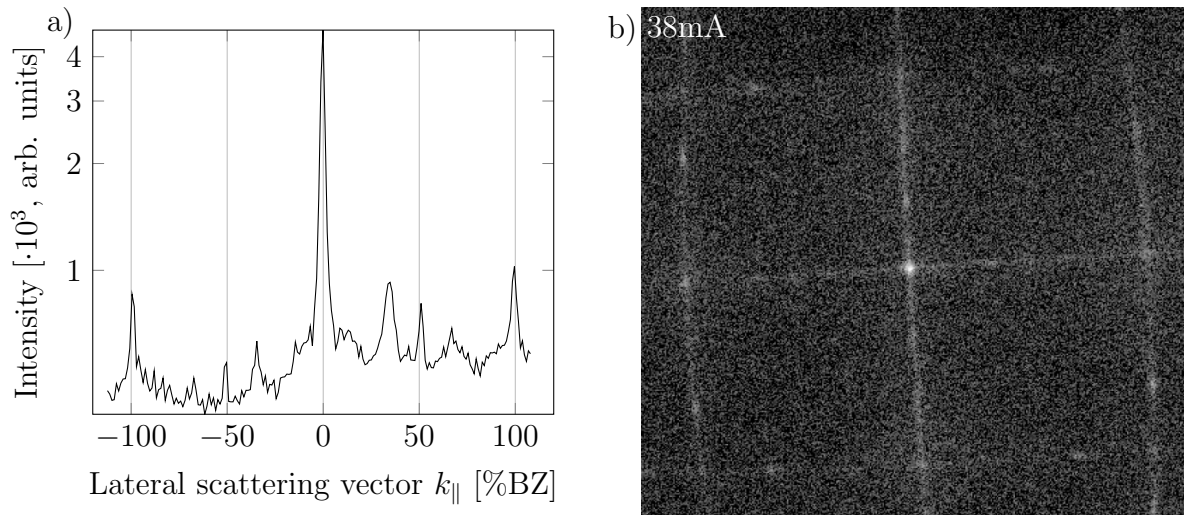
Figure 5.49: a) Linescan and b) 2D diffraction pattern of measurement conducted with evaporation power of 38mA. The coverage is about 660Hz and the scan axis is the same as in figure 5.2. Reflexes occur at positions of 50%BZ correlating with a (2x1) reconstruction, and 33%BZ and 67%BZ with their possible origin in (2x3) substructure as part of a in this measurement not detectable (2x7) superstructure on the surface. The measurement was done with an electron energy of 130eV.

5.7 Discussion of Series of Coverage

In this chapter, all five coverage series will be compared to each other based on different aspects. Coverage series is in the following shortened to *CS*.

First of all, both Gd and Tb were expected to present results with a (2x4), (2x7) and nanobundle structured surface, sequentially with smooth transitions. For both Gd and Tb, this behavior was shown in other research [2, 34, 38].

The broadening reflex gives information about the surface roughness of the sample surface. Its normalized intensities relatively to the total maximum intensity at 0%BZ mostly are low. They lie in the range of 0.01 to 0.2 for CS1 and CS4, the rest of the series have normalized intensities of about 0.1 to 0.4 at maximum (highest values only occurring at CS3). The FWHM of the broadening reflex at 0%BZ lies between 10% to 20% resp. 25%BZ for CS5 and CS3 and in a range of 20% to 35%BZ for the rest. A distinctive broadening reflex indicates that at least two levels exist on the sample surface. Due to high intensities of the central peak, one can assume wide terraces, possibly with about 2000Å [53] a higher width than the transfer width of the SPA-LEED instrument $\geq$1000Å [54]. This rules out that the original substrate had a bad surface quality. Possible contamination of the surface with a high roughness can therefore be assumed to appear earliest during the deposition process.

Between CS3 and CS4, the lens system of the SPA-LEED apparatus had been repaired which led to 2D patterns of higher quality. This reparation has influence on the evaluated FWHM of the reflexes as well, which can only be examined for a coverage of 0Hz. For higher coverages, a broadening of the reflexes can have other causes as well. For 0Hz, the 0%BZ cp of CS1 to CS3 have FWHM of 3%, 2.5% and 2%BZ, whereas after the repair, FWHM of 1.5% and 2.1%BZ occur. This could indicate a decreased FWHM due to the repair of the lens system, but since the ranges overlap a little, one could assume that the influence of the repair on these results is negligible.

For 0Hz, FWHM of the reflexes at 50%BZ lie in a range of 1.5% to 3%BZ for all coverage series. The low values indicate that one can assume a clear and structured (2x1) reconstructed surface for the pure Si(001) substrate.

For higher coverages, the peak at a lateral scattering vector of 50%BZ can originate from a superposition of (2x1), (2x4) and (2x7) surface structures. For low coverages, CS1 to CS4 show high normalized intensities and low FWHM. With further increasing coverage, FWHM increase and intensities show a decreasing tendency. In CS3 and CS4, for a temperature of 500°C during deposition, normalized intensities lie in a range of 0.01 to 1 for Gd and 0.02 to 0.3 for Tb, indicating for this temperature and Tb as RE, structures with a (x2) periodicity cover more surface than it is the case for Gd. At this substrate temperature for Tb deposition, the FWHM lie in a range of 1% to 3%BZ, whereas for Gd they reach from 2% to 9%BZ indicating that for Tb, wider domains of (x2) structured surface exist. For both RE, reflexes start to decrease at about 100Hz.

For a substrate temperature of 600°C during deposition, both CS1 and CS2 with Gd show different behavior in FWHM and normalized intensities for the reflex at 50%BZ. From a lower deposition rate in CS1 result FWHM of 3% to 18%BZ and normalized intensities

from 0.01 to 1. In CS2 with an increased deposition rate, normalized intensities lie in a range of 0.01 to 0.5 and FWHM between 1% and 8%BZ. The coverage at which the reflex starts to decrease is about 200Hz for CS1 and 100Hz for CS2. Hence, a higher deposition rate and thereby reduced deposition time leads to lower normalized intensities but also lower FWHM, indicating that the ratio of the (x2) reconstructed surface possibly decreases with increasing deposition rate, but the domain size increases at the same time. In contrast to CS1 to CS4, CS5 with Tb and a substrate temperature of 600°C during deposition shows low normalized intensities for coverages up to 120Hz, increasing afterwards, whereas FWHM start high and decrease at about 120Hz. Both CS with Tb show low FWHM values of 1% to 3%BZ, in contrast to CS with Gd. Low normalized intensities and high FWHM could also result from a bad positioning of the scan axis for the linescan in CS5, leading to lower intensities and higher FWHM.

The (2x4) structure appears in all coverage series but CS3. It is most present in CS1 between about 40Hz and 200Hz, in CS2 it already occurs at 20Hz and exists up to 120Hz. In CS4, the range for a (2x4) reconstructed surface reaches from 60Hz to 280Hz and in CS5 from 140Hz to the highest coverage of 350Hz. In CS3, the reflexes indicating a (2x1) structure are replaced directly by a (2x7) structure. The difference to the coverage series before is that the sample temperature during evaporation was changed from 600°C to 500°C. This leads to the conclusion that for Gd for reduced temperatures, the (2x7) reconstruction is formed preferentially.

Reflexes at 25%BZ and 75%BZ show similar behavior in each coverage series. Normalized intensities lie in a range of 0.01 to 0.1 for all CS except for the reflex at 25%BZ at CS4 with values from 0.1 to 0.8. FWHM values are between 2% and 7%BZ, rising to 9%BZ for the reflex at 75%BZ of CS5. Very similar courses of FWHM of reflexes correlating with a (2x4) structure in each coverage series give the information that the distribution of different domain boundaries probably is independent of the coverage.

Comparing all measurements with a sample temperature of 600°C during deposition, they show very similar results with similar courses and values of FWHM between 2% and 7%BZ and normalized intensities in a range of 0.01 to 0.1. In contrast, measurements at a temperature of 500°C lead to results with no (2x4) reconstruction in CS3 and lower FWHM between 1% and 3%BZ for CS4 for a wide coverage range of 60Hz to 240Hz. The reflexes at lateral scattering vectors of 25% and 75%BZ appear sharpest in CS4 for a temperature of 500°C of the sample during deposition of Tb. For coverages of 60Hz to 240Hz, the normalized intensities stay at a high plateau of 0.1 to 0.4 for 25%BZ and between 0.05 and 0.2 for the reflex at 75%BZ. This indicates a high percentage of the surface showing a (2x4) reconstruction. The (2x4) reconstruction seems to grow more long-ranged for a sample temperature of 500°C, or not at all like in CS3. Hereby, the used RE element could explain the different results for the same sample temperature.

Comparing different deposited RE, one can notice that lowest mean FWHM values for reflexes at 25% and 75%BZ can be achieved for the use of Tb. Hereby, FWHM in the areas of high intensities lie below 8%BZ, whereas for measurements with Gd, values rise up to about 15%BZ. This indicates that Tb has the tendency to build more long-ranged (2x4) reconstructions on the surface.

Furthermore, CS with Gd and Tb show no significant differences in FWHM or intensity

courses. The high chemical similarity seems to allow a direct comparability of the elements. Only for a substrate temperature of 500°C, Gd enables a preferred growth of a (2x7) reconstruction, whereas at this temperature Tb favors the growth of a relatively long-ranged (2x4) reconstruction.

In CS1, for coverages of 80Hz and above, streaky intensity on the main axes indicates the existence of nanowires on the surface. For coverages of 180Hz and above, reflexes at lateral scattering vectors of 20%, 40% and 80%BZ appear, correlating with a (2x5) structure on the surface.

A (2x5) structure was found in former research applying Gd on Si(100) by YEOM et al. [55] in LEED and STM examinations for coverages of about 0.7 monolayers and sample temperatures of 600°C. Results are shown in figure 5.50. (2x5) structure growth conditions were found to correspond to a regime where the nanowires dominate the surface, replacing a (2x7) superstructure on the surface. At higher coverages with an increased density of nanowire bundles, YEOM et al. found that the nanowire superlattice within each bundle has a (x5) periodicity (see the inlet of figure 5.50 e)). A guess is that each nanowire is composed of four unit cells of Gd silicide and a trench corresponds to a misfit dislocation.
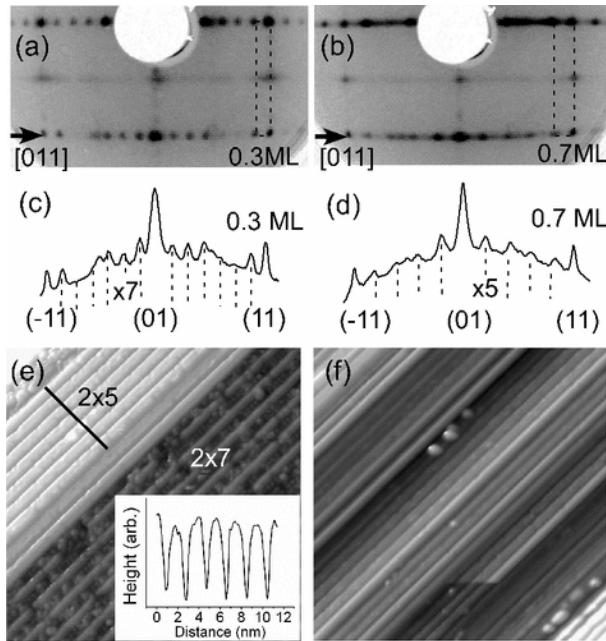
Figure 5.50: LEED patterns for Gd on Si(001) prepared at a sample temperature of 600°C with Gd coverages of a) 0.3 and b) 0.7 monolayers. Detailed LEED intensity profiles of the reflexes of superstructures along [001] shown by the arrows in a) and b) are given in c) for 0.3 and in d) for 0.7 monolayers, corresponding STM images in e) with 0.5 and f) 0.7 monolayers with sample bias voltages of +1.5 and +1.6V. The inset in e) shows the line profile across a silicide nanowire bundle (along the bar in the image). Taken from [55].

For CS2, besides the already described (2x1) and a (2x4) reconstruction for lower coverages with very weak reflexes for more than 250Hz, low additional reflexes appear with lateral scattering vectors possibly correlating with a (x9) or (x10) structure of unclear origin. Intensities are too low to allow further evaluation of this structure, but a comparable periodicity appears again in CS5. For coverages of 120Hz and above, streaks on the main axes indicate the existence of nanowires on the surface and are present until highest coverages. A possible explanation for a (x9) or (x10) periodicity could also be a regularity in formation of nanowires, with a structure analogous to the (2x5) described above. The nanowires within each bundle could hereby possibly show a (x9) or (x10) periodicity.

Reflexes indicating a (x7) periodicity on the surface appear only for sample temperatures

of 500°C during deposition, but for both Gd and Tb. For Tb, not all expected reflexes appear, but only at 42%BZ which lets not assume a (2x7) reconstructed surface. A sample temperature of 600°C could favor the growth of other structures, independently of the RE element deposited. Additionally, for the lower temperature the appearance of related reflexes can be seen beginning from a coverage of 100Hz resp. 120Hz, which is lower than for surface structures with a (x5) or (x9) resp. (x10) periodicity for CS with a sample temperature of 600°C during deposition, appearing at 140Hz resp. 180Hz. The coverage range for the described periodicities for 500°C samples reaches up to 180Hz for both Gd and Tb in CS3 and CS4. This indicates that surface structures with a (2x7) periodicity appear already for a lower temperature and lower coverages than those attributed to nanowires.

FWHM of reflexes associated with a (2x7) reconstructed surface in both CS lie at about 4% to 8%BZ, whereas normalized intensities are about 10% lower for the sample with Tb than for Gd.

The surface structure with a (x9) or (x10) periodicity probably resulting from a periodicity in nanowire formation only appears for a sample temperature of 600°C during deposition, hence one can assume that this reconstruction needs a higher energetic level to form, independently of the used RE. For Gd, the intensities are too low to evaluate FWHM of the appearing reflexes in the diffraction pattern, whereas for Tb FWHM values lie in the same range as the (2x5) structure in CS1 and the (x7) structures in CS3 and CS4, between 4% and 8%BZ. Normalized intensities for the (x9) or (x10) periodic structure in CS5 lie in a wider range than the others, between 0.001 and 0.05. The reflex at 11%BZ makes an exception with a normalized intensity up to 0.15, probably caused by a superposition with a reflex resulting from nanowire bundling.

In CS4, after the appearance of reflexes of a (2x1) and a (2x4) reconstruction for coverages up to 280Hz, additional streaks on the main axes point to the existence of nanowires. Reflexes can be noticed at about 11%, 33%, 42% and 85%BZ. They can not all be assigned to one surface structure, but could have different causes. Reflexes at 11% and 85%BZ are assumed to originate from the average groove-to-groove distance of nanowire bundling. Due to low intensities and high FWHM of the reflex at 85%BZ, its shift in position is not further evaluated. The reflex at 33%BZ indicates the existence of a (x3) reconstruction, but for that one would expect a reflex at about 67%BZ as well. A (x3) reconstruction appeared at an additional measurement in chapter 5.6. Hereby, the (x3) periodicity occurs at a substrate temperature of 550°C during deposition and coverages of 80Hz, 160Hz and 660Hz with varying deposition duration. A (x3) periodicity could not be reproduced in the context of this thesis. A possible explanation can be the existence of the (2x3) substructure of the (2x7) structure, but without the reflexes correlating with a (2x7) surface reconstruction. However, the existence of a pure (2x3) reconstruction on the surface without a (2x4) structure is not convincing. The lateral scattering vector of the reflex at about 42%BZ could correlate with a (2x7) reconstruction on the surface, but it is the only suitable reflex and therefore does not allow any conclusion regarding possible surface structures.

All in all for the appearance of reflexes correlating with structures other than (2x1) followed by (2x4), no consistent observations can be made for these five coverage series. For

CS with Gd, (2x5), (x9) or (x10) and (2x7) reconstruction can be witnessed, as well as streaky intensity from nanowires and once a reflex possibly indicating the average groove-to-groove distance of nanowire bundles. Tb also gives reflexes possibly originating from nanowire bundling, as well as additional reflexes with unclear origin and additionally again some kind of (x9) or (x10) periodicity.

CS1 and CS2 have the same preparation conditions with the use of Gd and a sample temperature of 600°C during deposition, only that the duration of the deposition process was reduced from 1 minute to 54 minutes for CS1 to 20 seconds to 210 seconds for CS2. This could indicate that the (2x5) structure forms on the surface when the sample is held at an elevated temperature and therefor an elevated energy level for a longer time. The (2x5) reconstruction seems to need more energy over a longer period of time to form properly, whereas for a shorter time, nanowires with a (x9) or (x10) periodicity build on the surface. Hereby, the time was reduced for trace gas atoms to have disruptive impact on the sample surface. The reflexes of a (x9) or (x10) reconstruction with Gd in CS2 also appear for Tb in CS5, both CS were performed at a sample temperature of 600°C during deposition. It can be assumed that this periodicity results from a structure of the nanowires within each bundle. Each nanowire could be composed of 8 or 9 unit cells of Gd resp. Tb silicide and a trench corresponding to a misfit location.

No correlation between the sample temperature during deposition and certain surface structures can be identified comparing these five CS. Only for 500°C and Gd as RE, a diffraction pattern of a (2x7) reconstruction is visible. For Tb at this temperature, only (2x1), (2x4) and streaks appear. Additionally, no correlation can be noticed between the Rare Earth element and certain surface structures. For Gd, reflexes of a (2x1), (2x4), (2x5) and a (x9) or (x10) periodicity occur, whereas for Tb (2x1), (2x4) and also a (x9) or (x10) periodicity can be seen. All coverage series have in common, that streaks appear on the main axes for high coverages indicating the existence of nanowires.

APPELFELLER reported a closed film of the wetting layer with some nanowires for an annealing temperature of 500°C and a coverage of about 0.5ML examined by STM. Under these conditions, another surface structure called dark wires was reported. For hereby increasing the annealing temperature, nanowires are also observed with the space in between not being exclusively filled with the wetting layer but being disordered [2]. This could be a possible explanation why for a substrate temperature of 600°C during deposition, no (2x7) reconstructed surface could be observed within this thesis. A lower ratio of the space in between the nanowires could be filled with an ordered (2x7) reconstructed wetting layer but with a disordered structure.

The evaluation of reflexes correlating with the average groove-to-groove distance of nanowire bundles was performed at CS3, CS4 and CS5 for reflexes at different lateral scattering vectors. For CS3, reflexes are at about 18% and 85%BZ, whereas for CS4 and CS5 they are at about 9% to 11%BZ.

The reflexes evaluated regarding their possible origin in nanowire bundles appear for both sample temperatures during deposition and both RE elements. For Tb and both sample temperatures, a reflex at about 11%BZ appears, whereas for Gd a peak can be seen at 18%BZ. Both the 11%BZ reflexes have a FWHM of about 3% to 11%BZ and normalized intensities of 0.01 to 0.15. In contrast to Tb at a temperature of 500°C during

deposition, CS3 with Gd shows a clear reflex at 85%BZ, probably being more intense due to a superposition wit the reflexes caused by the (2x7) reconstruction of the surface. For Tb in CS4, this reflex can only be guessed and is therefore not evaluated.

For Gd, the reflexes associated with the nanowire bundling appear at coverages of 60Hz resp. 120Hz to 490Hz, whereas for Tb they exist from 140Hz resp. 180Hz to 300 resp. 350Hz. Hence for Gd the nanowire bundles with this average groove-to-groove distance are assumed to stay for a wider range of coverages, whereas for Tb they start to disappear earlier. Normalized intensities are at a similar range of 0.01 to 0.15 for both CS with Tb, whereas for Gd values are lower between 0.001 and 0.1.

Regarding the areas of increase of $d(11\%BZ)$ of CS4 and CS5, one could assume that in the beginning of the nanowire growth, only small parts of the surface are covered with nanowire bundle domains. With an increasing amount of Tb on the sample surface, more areas with a nanowire bundle coverage could be created. APPELFELLER showed that small fluctuations of the Tb density, e.g. by locally higher defect density or surface step accumulation, might enable the nucleation of nanowires in certain sample areas [2]. The decrease for higher coverages can be explained by more nanowires bundles growing on the surface, leading to the fact that they move closer together. For CS5, it would be interesting to examine samples with coverages higher than 350Hz to see if d reaches a maximum and at some point decreases again as in CS4.

In [2], APPELFELLER states the general trend of Tb nanowires becoming denser and forming broader bundles, i.e. bundles incorporating more nanowires, with increasing coverage, independently of the annealing temperature. This does not necessarily have influence on the average groove-to-groove distance between the bundles. For a lower temperature like 500°C in CS4, mainly single nanowires and small bundles are observed, while higher temperatures like 600°C in CS5 and higher are described to possibly lead to the extinction of single nanowires for higher Tb coverages examined also by *Scanning Tunneling Microscope*. APPELFELLER states that this can be explained by the assumption of reduced diffusion length at lower temperatures leading to more separated growth. In addition, he assumes that the nanowires grow parallel to the wetting layer rows, so that diffusion barriers perpendicular to these rows may slow down the agglomeration of wider nanowire bundles at lower temperatures. By analyzing the reflexes probably correlating with the average groove-to-groove distance of the nanowire bundling on the surface, the same values were achieved in other research for coverages of 1.85 and 2.2 monolayers of Tb at both annealing temperatures. Hereby, the optimal nanowire width of densely packed nanowires seems independent of the annealing temperature [2].

Exemplary measurement results from APPELFELLER for an annealing sample temperature of 550°C and a coverage of 1.85 monolayers of Tb are presented in figure 5.51. Hereby, the values for the average groove-to-groove distances mainly lie in a range of 1.3nm to 3nm which equals a range of $3.3a_{Si(001)}$ to $7.8a_{Si(001)}$, similar to $d(18\%BZ)$ in CS3, but lower than in CS4 and CS5. This could indicate a similar nanowire surface structure for CS3, although in CS3 Gd was used as RE material.

In CS2 and most distinctive in CS5, the normalized intensities of the reflex at 50%BZ indicate the existence of a (x2) reconstruction for high coverages too, which can not be accounted to the dimers on the pure Si(001) surface. In a coverage range of 120Hz to
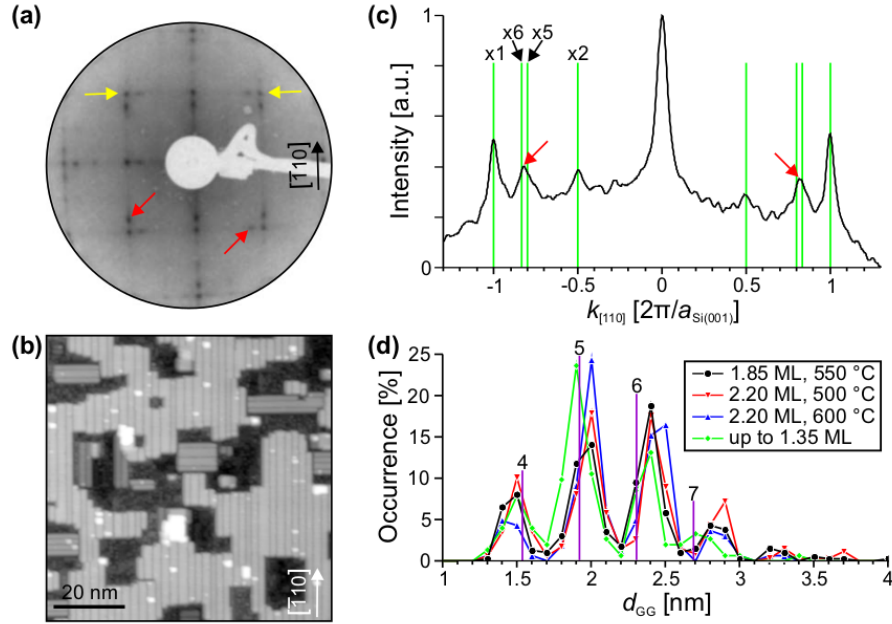
Figure 5.51: a) LEED and b) STM image of the same preparation with 1.85 ML Tb annealed at 550°C. The red arrows in a) mark additional spots due to the bundling. c) Intensity profile between the yellow arrows in a). The red arrows and the green lines mark the additional spots and expected maxima positions for certain periodicities of a Si(001), respectively. (d) Histogram of groove-to-groove distances d_{GG} preparations in [2]. The numbers at the vertical lines indicate the theoretical groove-to-groove distances in units of a Si(001). The lines connecting data points are guides to the eyes. Taken from [2].

highest coverages, one can assume that the streaks on the main axes together with the indication of a (x2) reconstruction point to the existence of a (2x1) reconstruction on the nanowire surface. Hereby, the (2x1) nanowire surface reconstruction is assumed to be the energetically most favorable for Tb silicide nanowires and a corresponding dimerization of the topmost Si atoms is indicated in a structure model presented in [34].

All in all, one can say that in the context of this thesis, RE silicide structure growth of a (2x4) reconstructed surface can be shown consistently except for CS3. For higher coverages, the resulting diffraction patterns and correlating surface structures differ a lot. Different periodicities deviating from other research occur and associated reflexes have low intensities relatively to the 0%BZ reflex. Therefore it is difficult to make statements based on the coverage series in this thesis. The origin of this partly unexpected behavior is unclear. Probably it results from an unknown contamination of the SPA-LEED chamber or the evaporator, possibly implied by an elevated amount of C appearing in the XPS measurement.

6 Summary and Outlook

In the context of this thesis, the formation of Gd and Tb silicide monolayers on Si(001) were examined. The deposition of the RE material was carried out by epitaxial growth with different preparation parameters. Hereby, in five coverage series, the coverages were increased successively from 0Hz to about 350Hz resp. 1000Hz. The samples were prepared and examined by SPA-LEED in UHV with a base pressure of about 10^{-10}mbar. Additional measurements were performed to identify suitable preparation and measurement parameters. For all SPA-LEED measurements, an electron energy of 130eV was chosen.

All five coverage series show a (2x1) reconstruction resulting from Si dimers on the pure Si(001) surface, followed by reflexes indicating a (2x4) reconstruction except for CS3, building a wetting layer in between nanowires [37]. CS1, with a substrate temperature of 600°C during deposition and a Gd silicide coverage, shows a diffraction pattern indicating a (2x5) reconstructed surface for high coverages which could hint to periodic bundling of nanowires. CS2 with the same preparation conditions except an increased deposition rate shows a (x9) or (x10) periodicity with low normalized intensity. For CS3, the sample temperature was reduced to 500°C during the deposition of Gd which lead to the occurrence of the diffraction pattern of a (2x7) reconstructed surface for up to 280Hz. The same preparation parameters were used for CS4, but as RE element now Tb was used. Again, a (2x4) reconstructed surface is indicated by the diffraction pattern, existing up to a coverage of 280Hz too. The last coverage series was carried out with an elevated substrate temperature of 600°C during deposition of Tb. The results indicate again the existence of a (x9) or (x10) reconstructed surface, comparable to CS2.

All coverage series have in common, that from a certain coverage on, the intensity on the main axes forms streaks. This suggests a consistent growth of nanowires for elevated coverages.

At additional measurements with Gd, a (x3) periodicity has occurred which could not be reproduced.

The goal of this thesis was to study the growth of Gd and Tb induced superstructures on the Si(001) surface, varying different parameters. This was only partly achieved, because no consistent growth behavior with a clear temperature or RE element dependency could be identified. Instead, a wide variety of reflexes of different periodicities appeared in the diffraction patterns. This lets assume that some unidentified interfering influences exist leading to growth behavior deviating from other research.

In an XPS measurement carried out for a sample with a Tb coverage of 350Hz, an elevated amount of C and O on the sample could be noticed. This could indicate a contamination of UHV chamber or evaporator, but can also be explained by the fact that the sample had to be taken to ambient conditions to transfer to the XPS measurement chamber.

Additionally, the XP spectrum indicates the existence of Dy on the sample, which probably results from former sample preparation with the same evaporator.

To further evaluate the Gd and Tb silicide growth on Si(001), it is necessary to identify the sources of contamination. Additionally, more SPA-LEED measurements are necessary to see if measurement results can be reproduced and disturbances can be eliminated. For some coverage series, a wider coverage range would be good to evaluate how surface structures develop for higher coverages. An examination of the same samples with other measurement methods as STM would give another perspective on what structures might develop on the sample surface and would help to interpret the SPA-LEED diffraction patterns. Additionally, one could use vicinal Si(001) as substrate to further study the growth of nanowires induced by RE. Furthermore, a calibration of the evaporator, e.g. with spectroscopic methods, would allow to convert the amount of deposited material into coverage values to directly compare to other research.

Bibliography

[1] C. Preinesberger, S. K. Becker, S. Vandré, T. Kalka, and M. Dähne. Structure of DySi2 nanowires on Si(001). *Journal of Applied Physics*, 91(3):1695–1697, feb 2002.

[2] Stephan Appelfeller. *Atomic structure and electronic properties of Tb silicide nanowires*. PhD thesis, Berlin, Technische Universität Berlin, 2018.

[3] Martina Wanke and Mario Dähne. Comment on 'Structure and electronic properties of dysprosium-silicide nanowires on vicinal Si(001)' [Appl. Phys. Lett. 87, 083107 (2005)]. *Applied Physics Letters*, 99(3):036101, jul 2011.

[4] D. E. Chang, A. S. Sørensen, P. R. Hemmer, and M. D. Lukin. Quantum Optics with Surface Plasmons. *Physical Review Letters*, 97(5), aug 2006.

[5] A. Bravais. *Mémoire sur les systèmes formés par des points distribués régulièrement sur un plan ou dans l'espace*. Bachelier, 1850.

[6] Elizabeth A. Wood. Vocabulary of Surface Crystallography. *Journal of Applied Physics*, 35(4):1306–1312, apr 1964.

[7] Robert L. Park and Hannibal H. Madden Jr. Annealing changes on the (100) surface of palladium and their effect on CO adsorption. *Surface Science*, 11(2):188–202, 1968.

[8] K. Oura, M. Katayama, A. V. Zotov, V. G. Lifshits, and A. A. Saranin. *Surface Science*. Springer Berlin Heidelberg, 2003.

[9] Udo W. Pohl. Thermodynamics of Epitaxial Layer-Growth. In *Graduate Texts in Physics*, pages 131–170. Springer Berlin Heidelberg, 2013.

[10] Marian A. Herman, Wolfgang Richter, and Helmut Sitter. Heteroepitaxy Growth Phenomena. In *Epitaxy*, pages 389–421. Springer Berlin Heidelberg, 2004.

[11] Florian Bertram. *The structure of ultrathin iron oxide films studied by x-ray diffraction*. PhD thesis, Universität Osnabrück, 2013.

[12] Henrik Wilkens. *Phase transitions of rare earth oxide films grown on Si(111)*. PhD thesis, Universität Osnabrück, 2014.

[13] Frederic Timmer. *Diffraction studies on ordering of quasi-one-dimensional structures and nanowires on silicon surfaces induced by metals*. PhD thesis, Osnabrueck University, 2017.

[14] Jascha Bahlmann. SPA-LEED-Untersuchungen an quasi-eindimensionalen Dysprosiumsilizidstrukturen auf Si(001), 2015.

[15] Olga Schuckmann. Plasmamodifizierung von Praseodym- und Ceroxidschichten. Master's thesis, Universität Osnabrück, 2012.

[16] Martin Henzler. Defects at semiconductor surfaces. *Surface Science*, 152-153:963–

976, apr 1985.

[17] Joachim Wollschläger. *Ordnungsvorgänge in einatomaren Metallschichten auf hochin-duzierten Metallflächen.* PhD thesis, Universität Hannover, 1990.

[18] Daniel Bruns. *Structure and morphology of ultrathin iron and iron oxide films on Ag(001).* PhD thesis, Universität Osnabrück, 2012.

[19] Jari Rodewald. Oxidation epitaktischer Eisenschichten auf Ag(001). Master's thesis, Universität Osnabrück, 2014.

[20] Robert Oelke. SPA-LEED Untersuchungen an dünnen Ceroxidfilmen auf Si(001), 2013.

[21] http://www.chemgapedia.de/vsengine/vlu/vsc/de/ph/14/ep/einfuehrung/wellenoptik/interferenz_a.v last access january 24, 2021.

[22] M. Horn von Hoegen. Growth of semiconductor layers studied by spot profile analysing low energy electron diffraction. *Zeitschrift für Kristallographie - Crystalline Materials*, 214(10), jan 1999.

[23] Ralph Buß. Studies on the Epitaxial Growth of Ultrathin Metal Oxide Films. Master's thesis, Universität Osnabrück, 2015.

[24] U. Hilleringmann. *Silizium-Halbleitertechnologie: Grundlagen mikroelektronischer Integrationstechnik.* Springer Fachmedien Wiesbaden, 2014.

[25] M. C. Neuburger. Präzisionsmessung der Gitterkonstante von Silicium. *Zeitschrift für Kristallographie - Crystalline Materials*, 92(1-6), jan 1935.

[26] E. P. Donovan, F. Spaepen, D. Turnbull, J. M. Poate, and D. C. Jacobson. Heat of crystallization and melting point of amorphous silicon. *Applied Physics Letters*, 42(8):698–700, apr 1983.

[27] H. Over, J. Wasserfall, W. Ranke, C. Ambiatello, R. Sawitzki, D. Wolf, and W. Moritz. Surface atomic geometry of Si(001)-(2x1): A low-energy electron-diffraction structure analysis. *Physical Review B*, 55(7):4731–4736, feb 1997.

[28] J. R. Banister, S. Legvold, and F. H. Spedding. Structure of Gd, Dy, and Er at Low Temperatures. *Physical Review*, 94(5):1140–1142, jun 1954.

[29] Walter Greulich. *Lexikon der Physik. 6. Gesamtwerk (inkl. Register).* Spektrum, Akad. Verlag, 2000.

[30] C. Rau and S. Eichner. Evidence for ferromagnetic order at gadolinium surfaces above the bulk Curie temperature. *Physical Review B*, 34(9):6347–6350, nov 1986.

[31] Hermann Sicius. *Seltenerdmetalle: Lanthanoide und dritte Nebengruppe.* Springer Fachmedien Wiesbaden, 2015.

[32] M. Jackson. Magnetism of Rare Earth. *The IRM Quarterly*, 2000.

[33] J. Nogami, B. Z. Liu, M. V. Katkov, C. Ohbuchi, and Norman O. Birge. Self-assembled rare-earth silicide nanowires on Si(001). *Physical Review B*, 63(23), may 2001.

[34] Stephan Appelfeller, Stefan Kuls, and Mario Dähne. Tb silicide nanowire growth on

planar and vicinal si(001) surfaces. *Surface Science*, 641:180–190, nov 2015.

[35] J. E. Baglin, F. M. d'Heurle, and C. S Petersson. The formation of silicides from thin films of some rare-earth metals. *Applied Physics Letters*, 36(7):594–596, apr 1980.

[36] J. E. E. Baglin, F. M. d'Heurle, and C. S. Petersson. Diffusion marker experiments with rare-earth silicides and germanides: Relative mobilities of the two atom species. *Journal of Applied Physics*, 52(4):2841–2846, apr 1981.

[37] B.Z. Liu, J. Nogami. An STM study of the Si(001)(2x4)-Dy surface. *Surface Science*, 540(1):136–144, aug 2001.

[38] B.Z. Liu, J. Nogami. An STM study of the Si(001) (2x7)-Gd, Dy surface. *Surface Science*, 540(1):136–144, aug 2003.

[39] C. Preinesberger, S.K. Becker, and M. Dähne. An STM Study of the 2x7 Dysprosium-Silicide Nanowire Superstructure on Si(001). In *AIP Conference Proceedings*. AIP, 2003.

[40] B. Z. Liu and J. Nogami. A scanning tunneling microscopy study of dysprosium silicide nanowire growth on Si(001). *Journal of Applied Physics*, 93(1):593–599, jan 2003.

[41] Saban M. Hus and Hanno H. Weitering. Formation of uni-directional ultrathin metallic YSi2 nanowires on si(110). *Applied Physics Letters*, 103(7):073101, aug 2013.

[42] Kris Holtgrewe, Stephan Appelfeller, Martin Franz, Mario Dähne, and Simone Sanna. Structure and one-dimensional metallicity of rare-earth silicide nanowires on Si(001). *Physical Review B*, 99(21), jun 2019.

[43] Stephan Appelfeller, Kris Holtgrewe, Martin Franz, Lars Freter, Christian Hassenstein, Hans-Ferdinand Jirschik, Simone Sanna, and Mario Dähne. Continuous crossover from two-dimensional to one-dimensional electronic properties for metallic silicide nanowires. *Physical Review B*, 102(11), sep 2020.

[44] Preinesberger and Vandré and Kalka and Dähne-Prietsch. Formation of dysprosium silicide wires on Si(001). *Journal of Physics D: Applied Physics*, 31(12):L43–L45, jun 1998.

[45] Y. Cui and J. Chung and J. Nogami. Controlling the width of self-assembled dysprosium silicide nanowires on the Si(001) surface. *Journal of Physics: Condensed Matter*, 24(4):045003, jan 2012.

[46] C. Ohbuchi and J. Nogami. Holmium growth on Si(001): Surface reconstructions and nanowire formation. *Physical Review B*, 66(16), oct 2002.

[47] J. A. Knapp and S. T. Picraux. Epitaxial growth of rare-earth silicides on Si(111). *Applied Physics Letters*, 48(7):466–468, feb 1986.

[48] K. Santoro and C. Ricciardi. Biosensors. In *Encyclopedia of Food and Health*, pages 430–436. Elsevier, 2016.

[49] Sebastian Gevers. SPA-LEED-Untersuchungen von Praseodymoxidschichten auf Si(111)-Substraten. Master's thesis, Universität Osnabrück, 2007.

[50] Falko Sojka, Matthias Meissner, Christian Zwick, Roman Forker, and Torsten Fritz. Determination and correction of distortions and systematic errors in low-energy electron diffraction. *Review of Scientific Instruments*, 84(1):015111, jan 2013.

[51] D. Briggs et al. Handbook of X-ray Photoelectron Spectroscopy. *Surface and Interface Analysis*, 3(4):v–v, aug 1981.

[52] Stefan Hüfner. Continuous Satellites and Plasmon Satellites: XPS Photoemission in Nearly Free Electron Systems. In *Springer Series in Solid-State Sciences*, pages 112–145. Springer Berlin Heidelberg, 1995.

[53] M. G. Lagally Y.-W. Mo. Anisotropy in surface migration of Si and Ge on Si(001). *Surface Science*, 248(3):313–320, 1991.

[54] http://spa-leed.com/components_en.html, last access january 22, 2021.

[55] H. W. Yeom, Y. K. Kim, E. Y. Lee, K.-D. Ryang, and P. G. Kang. Robust One-Dimensional Metallic Band Structure of Silicide Nanowires. *Physical Review Letters*, 95(20), nov 2005.

List of Figures

Ich versichere, dass ich die eingereichte Masterarbeit selbstständig und ohne unerlaubte Hilfe verfasst habe. Anderer als der von mir angegebenen Hilfsmittel und Schriften habe ich mich nicht bedient. Alle wörtlich oder sinngemäß den Schriften anderer Autoren entnommenen Stellen habe ich kenntlich gemacht.

Osnabrück, 25. Januar 2021

_____
Kristina Sprenger

Acknowledgements

I would like to thank everyone who supported me in writing this thesis.

My thanks go to Prof. Dr. Wollschläger, who provided the possibility to do my experimental research in his working group and was always able to spread his enthusiasm for this field of research. Thanks to all the other members of the working group „Dünne Schichten und Grenzflächen" who were always willing and able to help with experimental and theoretical problems occurring during the last two years.

I would especially like to thank Jascha Bahlmann for supporting me strongly whenever I did not know how to proceed. Thank you for many hours helping me fix my UHV chamber and explaining diffraction theory to me. Thanks to Jannis Thien for sharing his expertise about XPS analysis.

Thank you Tobi for being the best office mate I could wish for. I will miss that time.

Thanks to my flatmates and friends who, especially during the last months, were always there to pretend to know what I was talking about. And if not, they were there to provide the possibility to get distraction and recovery.

Thanks to my family who always stood behind me. Thank you for not asking too often about the progress of my thesis and at the same time, kindly pushing me forward.

Thank you Alex, for believing in me and always giving me the feeling that I could succeed in finishing this.